Forschungsbericht 2018-11

Boundary Layer Transition in External Aerodynamics and Dynamic Aeroelastic Stability

Michael Fehrs

Deutsches Zentrum für Luft- und Raumfahrt
Institut für Aeroelastik
Göttingen

161 Seiten
103 Bilder
17 Tabellen
135 Literaturstellen

DLR Deutsches Zentrum für Luft- und Raumfahrt

TU Braunschweig – Niedersächsisches Forschungszentrum für Luftfahrt

Berichte aus der Luft- und Raumfahrttechnik

Forschungsbericht 2017-27

Boundary Layer Transition in External Aerodynamics and Dynamic Aeroelastic Stability

Michael Fehrs

Deutsches Zentrum für Luft- und Raumfahrt
Institut für Aeroelastik
Göttingen

Diese Veröffentlichung wird gleichzeitig in der Berichtsreihe „NFL - Forschungsberichte“ geführt.

Diese Arbeit erscheint gleichzeitig als von der Fakultät für Maschinenbau der Technischen Universität Carolo-Wilhelmina zu Braunschweig zur Erlangung des akademischen Grades eines Doktor-Ingenieurs genehmigte Dissertation.

Boundary Layer Transition in External Aerodynamics and Dynamic Aeroelastic Stability

Von der Fakultät für Maschinenbau
der Technischen Universität Carolo-Wilhelmina zu Braunschweig

zur Erlangung der Würde

eines Doktor-Ingenieurs (Dr.-Ing.)

genehmigte Dissertation

von:	Michael Fehrs
aus:	Rendsburg

eingereicht am:	27.04.2017
mündliche Prüfung am:	05.12.2017

Gutachter:	Prof. Dr.-Ing. Lorenz Tichy
	Prof. Dr.-Ing. Rolf Radespiel

2018

Abstract

The dynamic aeroelastic stability of airfoils and wings is determined by aerodynamic, inertial, and elastic forces. A model representation of these forces is required to address aeroelastic phenomena like flutter. This thesis deals with the effect of boundary layer transition on the aerodynamics and aeroelasticity based on a computational fluid dynamics transition model.

A transition model for Reynolds Averaged Navier-Stokes computations is introduced that allows the prediction of the transition behavior in transonic, high Reynolds number flows in a low turbulence environment. The presented transition model is a simplification of the γ-Re_θ transition model and it is named γ transition model. The γ transition model is an empirical model, based on a transport equation for the intermittency variable γ.

The γ transition model is calibrated with experimental data for 2-dimensional airfoil test cases at moderate Mach numbers and moderate to high Reynolds numbers. After calibration, a large number of validation test cases is computed. The model gives reasonable results up to Reynolds numbers found in free flight. In addition, the extent of the laminar drag bucket is well predicted compared to experimental results and the model behavior is similar to the established e^N method. The γ transition model closes an existing gap for high Reynolds number, external aerodynamic applications in local correlation-based transition modeling.

Although the boundary layer influence on the aerodynamics is more pronounced at low Reynolds numbers, a partly laminar flow affects the drag and lift at free flight Reynolds numbers. More important for aeroelastic considerations, the occurrence of laminar separations, shock positions, and the shock strength are directly influenced by an upstream laminar boundary layer. These effects enable aeroelastic effects like a torsional flutter, which is connected to the shock-induced separation of the laminar boundary layer.

Zusammenfassung

Die dynamische aeroelastische Stabilität von Profilen und Tragflügeln wird durch aerodynamische, Trägheits- und elastische Kräfte bestimmt. Die Diskussion aeroelastischer Phänomene erfordert eine Modellierung dieser Kräfte. Diese Arbeit behandelt den Effekt der Grenzschichttransition auf die Aerodynamik und Aeroelastik, wobei ein Transitionsmodell aus dem Bereich der numerischen Strömungssimulation verwendet wird.

Ein Transitionsmodell für Reynolds-gemittelte Navier-Stokes-Methoden wird vorgestellt, das die Vorhersage des Transitionsverhaltens in transsonischen Strömungen bei hohen Reynoldszahlen und schwacher Störumgebung ermöglicht. Das vorgestellte Transitionsmodell stellt eine Vereinfachung des γ-Re_θ-Transitionsmodells dar und wird als γ-Transitionsmodell bezeichnet. Beim γ-Transitionsmodell handelt es sich um ein empirisches Modell, das eine Transportgleichung für die Intermittenzvariable γ verwendet.

Das γ-Transitionsmodell ist mittels zweidimensionaler Profilströmungen bei moderaten Machzahlen und moderaten bis hohen Reynoldszahlen kalibriert. Nach der Kalibrierung wird eine große Anzahl an Validierungsfällen berechnet. Das Modell liefert zufriedenstellende Ergebnisse bis zu Reynoldszahlen, die im Reiseflug auftreten. Zusätzlich wird die Laminardelle in der Lilienthal-Polare im Vergleich zu experimentellen Daten und der e^N-Methode befriedigend wiedergegeben. Das γ-Transitionsmodell schließt eine existierende Lücke bei der lokalen korrelationsbasierten Transitionsbestimmung für Außenströmungen bei hohen Reynoldszahlen.

Obwohl der Einfluss der Grenzschicht auf die Aerodynamik bei kleinen Reynoldszahlen stärker ausgeprägt ist, wird auch bei Reiseflug-Reynoldszahlen der Widerstand und Auftrieb von einer teilweise laminaren Strömung beeinflusst. Für die Aeroelastik ist hierbei von besonderer Bedeutung, dass laminare Ablösungen, die Stoßlage in der Transsonik und die Stoßstärke durch die laminare Grenzschichtströmung stromauf direkt beeinflusst werden. So führen diese Effekte zum Beispiel zu einem Torsionsflattern, das durch die stoßbedingte Ablösung der laminaren Grenzschicht ermöglicht wird.

Contents

Nomenclature

Symbols

A	=	amplitude, m
b	=	semi-chord length, m
c	=	chord length, m
c_d	=	drag coefficient
c_f	=	friction coefficient
c_l	=	lift coefficient
c_m	=	moment coefficient around quarter-chord
c_p	=	pressure coefficient
f	=	frequency, Hz
I_α	=	mass moment of inertia of wing segment about e.a., $\mathrm{kg\,m^2}$
k	=	specific turbulent kinetic energy, $\mathrm{m^2/s^2}$
k	=	reduced frequency
K	=	acceleration parameter
K_t	=	scaled acceleration parameter
L	=	lift, $\mathrm{kg\,m/s^2}$
M	=	Mach number
M_y	=	moment, $\mathrm{kg\,m^2/s^2}$
N	=	N factor
p	=	pressure, $\mathrm{kg/m/s^2}$
p	=	complex eigenvalue
Q_i	=	aerodynamic force vector, $(\mathrm{kg\,m/s^2}, \mathrm{kg\,m^2/s^2})^T$
R_T	=	viscosity ratio
r_α	=	radius of gyration about e.a.
Re	=	Reynolds number
Re_ν	=	vorticity Reynolds number
Re_θ	=	momentum loss Reynolds number

s	=	distance along streamline, m
S	=	strain rate magnitude, 1/s
S_α	=	static mass moment of wing segment about e.a., kg m
Tu	=	turbulence level
u, v, w	=	velocity component in x, y, z direction, m/s
U	=	velocity, m/s
x_α	=	non-dimensional distance of e.a. to c.g.
Δx	=	cell length in flow direction, m
$\hat{y}$	=	distance to the nearest wall, m
α	=	angle of attack, deg
$\widehat{\alpha}$	=	pitch amplitude, deg
β	=	Hartree parameter
γ	=	intermittency
δ	=	boundary layer thickness, m
δ	=	reduced damping
ζ	=	ratio $Re_{\nu,max} \,/\, Re_\theta = f(\beta)$
η	=	similarity variable
θ	=	momentum loss thickness, m
κ	=	specific heat ratio
λ_θ	=	pressure gradient parameter
Λ	=	sweep angle, deg
μ	=	dynamic viscosity, kg/m/s
μ_t	=	eddy viscosity, kg/m/s
ξ	=	ratio $Re_{\nu,max} \,/\, Re_\theta = f(M)$
ρ	=	density, kg/m^3
τ	=	turbulence level, %
Φ	=	phase angle, deg
ψ	=	wave number direction, deg
ω	=	specific turbulence dissipation rate, 1/s
$\omega_h \,/\, \omega_\alpha$	=	uncoupled natural frequency ratio

Subscripts

corr	=	corrected

$crit$	=	critical value
e	=	boundary layer edge value
fl	=	value at flutter
h	=	heave derivative
ind	=	indifference value
L	=	laminar
m	=	mean value
t	=	transition onset
T	=	end of transition region / turbulent
α	=	pitch derivative
∞	=	freestream

Abbreviations

AC	=	alternating current
ALF	=	Aerodynamik des Laminarflügels
ALLEGRA	=	Aeroelastic stability and loads prediction for enhanced green aircraft
ALT	=	attachment line transition
aoa	=	angle of attack
CF	=	crossflow
CFD	=	Computational Fluid Dynamics
c.g.	=	center of gravity
DLR	=	Deutsches Zentrum für Luft- und Raumfahrt
dof	=	degree of freedom
e.a.	=	elastic axis
LCO	=	limit cycle oscillations
LE	=	leading edge
MAV	=	micro aerial vehicles
NLF	=	natural laminar flow
RANS	=	Reynolds-averaged Navier-Stokes
T-S	=	Tollmien-Schlichting

List of Figures

List of Tables

1 Introduction

1.1 Motivation and Scope

Aeroelastic phenomena arise from the interaction of aerodynamic, inertial, and elastic forces (Bisplinghoff et al. 1996). To address any problem in aeroelasticity, the forces involved have to be understood and a model representation has to be found. This thesis deals with the effect of boundary layer transition on the aerodynamics and aeroelasticity based on a computational fluid dynamics (CFD) transition model.

In most cases, laminar flow exists downstream of the stagnation point and after some distance the laminar flow undergoes transition to a turbulent state. The boundary layer state influences the forces acting on an aerodynamic object in a flow field. As the aerodynamic forces change, the aeroelastic behavior is changed as well.

The computation of the flutter behavior with free boundary layer transition requires a transition prediction method to determine the aerodynamic forces correctly. The DLR TAU-Code provides a transition module based on the linear stability theory and a correlation-based transition model. The transition module fails to give a robust transition prediction at the laminar drag bucket limit and the correlation-based model is not suited for high Reynolds number flows.

This thesis introduces a transition model for Reynolds averaged Navier-Stokes (RANS) computations that allows the prediction of the transition behavior in transonic, high Reynolds number flows in a low turbulence environment. The presented transition model is a simplification of the γ-Re_θ transition model and it is named γ transition model. The γ transition model is an empirical model, based on a transport equation for the intermittency variable γ.

The first chapter gives an introduction into the topic of transition and aeroelasticity. The second chapter presents transition mechanisms and influence parameters on transition. The third chapter describes basic aeroelastic considerations for airfoil flutter. The fourth chapter presents the transition model and the fifth chapter gives results for validation test cases. In addition, unsteady test cases are presented, which include a discussion of the flutter stability for transitional flows at free flight Reynolds numbers. The last chapter presents the conclusion.

1.2 Scientific Background

1.2.1 Transition and Aerodynamics

At the end of the 19th century, experimental and theoretical effort was put on the problem of the resistance of fluid flows through pipes and of bodies moving through fluids. A description of the general character of a fluid in contact with a solid surface had still to be found and theorists were looking for a universal law of resistance. In 1883, Osborne Reynolds describes two basic classes of motion of water:

> "*...– either the elements of the fluid follow one another along lines of motion which lead in the most direct manner to their destination, or they eddy about in sinuous paths, the most indirect possible.*" (Reynolds 1883, p. 84)

As an example for this direct and sinuous motion, Reynolds presents the well-known pipe experiment: Dye is injected into clear moving water. In the case of direct motion, any irregularity will vanish in the absence of eddies and colored streaks of dye will be seen in the flow. In the case of sinuous motion, the dye will spread throughout the fluid.

Osborne Reynolds studied the occurrence of these eddies in pipes and classified a flow by the dimensionless quantity:

$$Re = \frac{\rho U c}{\mu} \tag{1.1}$$

– today named Reynolds number. It is given by the fluid density ρ, the flow velocity U, a characteristic length c, and the dynamic viscosity μ. Reynolds assumed that the occurrence of eddies in the flow and the change from direct to sinuous motion takes place at a certain Reynolds number. Today these basic types of fluid flow are called laminar and turbulent flow. Once the laminar flow gets unstable, it will undergo transition to turbulence.

According to Betchov and Criminale (1967), "[s]*tability can be defined as the quality of being immune to small disturbances*". In aerodynamic applications, there is a vast variety of sources for small disturbances in the flow. They range from acoustic disturbances in the flow field to surface imperfections and roughness elements. Therefore, "[l]*aminar or organized flow is the exception rather than the rule to fluid motion*" (Criminale et al. 2003). Nevertheless, a laminar flow is generally desired in many aerodynamic applications. In the case of an aircraft wing or airfoil, the laminar flow will reduce the friction drag.

Three major transition mechanisms exist for a transport aircraft: attachment line transition, crossflow transition, and Tollmien-Schlichting transition. The transition process depends to a large extend on the cruise flight Reynolds number and leading edge sweep. Figure 1.1 depicts the

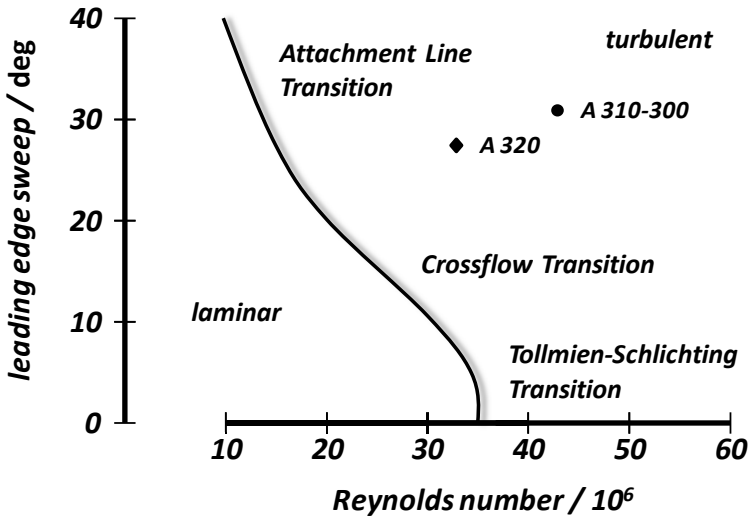

Figure 1.1: Natural laminar flow limit and transition modes for different Reynolds numbers and leading edge sweep angles. Adapted from Redeker et al. (1990).

limit of natural laminar flow (NLF) and the dominant transition mode for different Reynolds numbers and leading edge sweep angles according to Redeker et al. (1990). The NLF limit describes the design space, for which a large extent of laminar flow is possible by means of airfoil design. Beyond this boundary, active boundary layer control has to be used for extended laminarity on the device. Once a large laminar boundary layer flow is achieved, the influence on the aeroelastic behavior has to be considered.

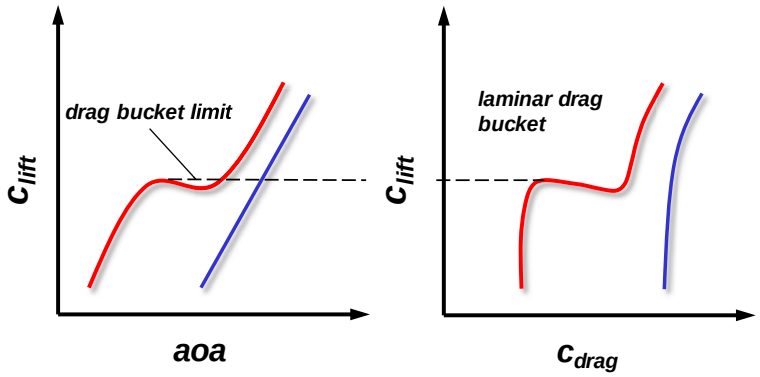

Figure 1.2: Laminar drag bucket and drag bucket limit

Figure 1.2 depicts the effect of a laminar boundary layer flow on the lift and drag curve of an airfoil. For a certain angle of attack range, the laminar boundary layer is stable over a large part of the chord length. The airfoil drag is therefore significantly lower in this range and the lift is increased. At some point, the transition position moves towards the leading edge. The

drag bucket limit is reached and the beneficial laminar flow is lost. Depending on the airfoil design, the change in the aerodynamic forces is rather abrupt and a novel aeroelastic behavior might be encountered.

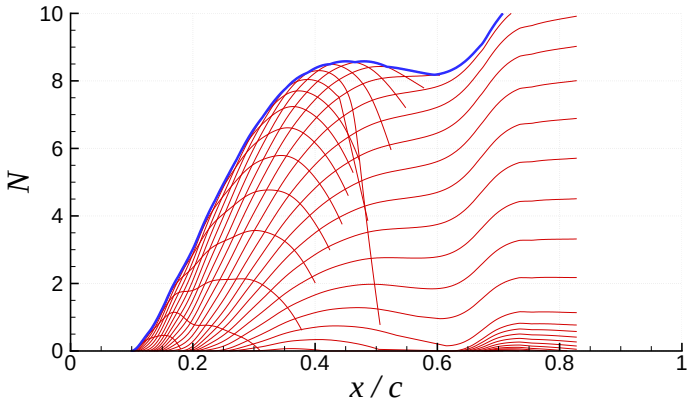

Figure 1.3: N factor distribution at the drag bucket limit: single frequency curves (red) and envelope of all curves (blue)

Figure 1.3 depicts a N factor distribution on the suction side of a supercritical airfoil at the drag bucket limit. The N factor describes the growth of disturbances inside the laminar boundary layer based on the linear stability theory. In the e^N method, the transition onset is assumed at a critical value of N (van Ingen 1956; Smith and Gamberoni 1956). For the case depicted, the transition location is prescribed based on an experimental transition location. In the experiment, first instabilities are measured at $x/c \approx 0.4$, the boundary layer is fully turbulent at $x/c \approx 0.65$, and the overall flow is steady (Hebler 2013, $M = 0.7, \alpha \approx -0.2°$).

The critical N factor for the experimental transition location at $x/c \approx 0.65$ does not give a unique transition location. It is said to be pathologic as the envelope of the N factor curves is intersected multiple times (Schrauf et al. 1998). In a CFD computation with free boundary layer transition based on the e^N method, no steady solutions are found for these cases, although a steady flow field might exist. Fehrs et al. (2015) show that the transport equation approach of the γ-Re_θ model gives robust results at the drag bucket limit. However, the method fails for high Reynolds numbers and needs to be revised.

1.2.2 Transition and Aeroelasticity

Aeroelastic phenomena are classified as dynamic or static problems. The former involve an interaction between inertial, aerodynamic, and elastic forces, the latter between aerodynamic and elastic forces (Bisplinghoff et al. 1996). The most prominent dynamic aeroelastic phenomenon

is flutter. Flutter is defined "*as the dynamic instability of an elastic body in an airstream*" (Bisplinghoff et al. 1996, p. 527).

Energy is transferred from the airstream into the movement of the elastic body by the aerodynamic forces acting on it. Once flutter occurs, it is catastrophic in nature and will usually result in the loss of structural integrity. The determination of the flutter boundary, the airspeed at which flutter occurs, is a major part in the airplane design process.

Reports exist of unexpected aeroelastic behavior in wind tunnel experiments, which is supposed to be caused by boundary layer transition. In addition, numerical studies on the unsteady aerodynamic behavior associated with free boundary layer transition show the importance of boundary layer transition in aeroelastic considerations. Some examples are given below.

Van de Vooren and Bergh (1951) report spontaneous pitch oscillations of a symmetrical airfoil in a wind tunnel test. The oscillations occur only for a laminar boundary layer flow. They are suppressed by creating a turbulent boundary layer on the airfoil. It is assumed that the oscillations are due to an instability of the laminar boundary layer. The frequency of the small amplitude oscillations coincide with the natural frequency of the model. In addition, the frequency is in the range to excite unstable boundary layer modes. Therefore, it is assumed that a self-exciting feed-back mechanism exists that is caused by the transition behavior of the boundary layer (van de Vooren and Bergh 1951).

Erickson (1974) describes wind tunnel tests for low aspect ratio wings with subsonic airfoil sections in transonic flows. This aerodynamic design is found on space shuttles. Without boundary layer trips on the model, the Mach number at flutter increases slightly and the flutter mode changes. The flutter mode is most likely a single mode type (Erickson 1974). As the results are sensitive to the Reynolds number, Erickson (1974) stresses the importance of testing as close as possible to full scale boundary layer characteristics.

Houwink et al. (1982) present results for a flutter test of a supercritical transport aircraft wing in transonic flow. At low stagnation pressure, one-degree-of-freedom (dof) oscillations of the model are reported with a zero damping of the wing bending. The low stagnation pressure results in a decreased Reynolds number and the transition tripping gets ineffective. The airloads given by a partly laminar boundary layer flow differ considerably from the airloads at higher Reynolds numbers in a fully turbulent flow.

Mabey et al. (1987) investigate the effect of transitional boundary layers, for which a large proportion of the boundary layer flow is laminar, on the aeroelastic behavior of wind tunnel models. In a wind tunnel test, violent oscillations occur in the first wing bending mode if no transition tripping is used. Mabey et al. (1987) assume that the transitional boundary layer reduces the aerodynamic damping and magnifies the unsteady aerodynamic excitation.

Poirel et al. (2008) report wind tunnel tests of a NACA 0012 airfoil in a low Reynolds number range of $Re = 10^4$ ... 10^6, for which laminar boundary layer flow naturally exists on the airfoil. The airfoil exhibits nonlinear dynamic behavior given by limit cycle oscillations. Although no direct measurement is made, it is assumed that the oscillations are initiated by laminar separation bubbles.

Hebler et al. (2013) describe a transonic wind tunnel experiment on the flow around the supercritical CAST10-2 airfoil in the DNW-TWG transonic wind tunnel. The aerodynamic coefficients of the supercritical airfoil show strong nonlinearities at the upper limit of the laminar drag bucket in transonic flow. As the drag bucket is left, a phase lead of the pitch moment coefficient derivative is found that makes a 1-dof flutter possible. The experimental results are qualitatively reproduced by Fehrs et al. (2015) with the γ-Re_θ transition model. Fehrs et al. (2015) show that a transition-induced 1-dof torsional flutter exists.

All these cases demonstrate the importance to provide a reliable transition prediction method for aeroelastic problems. A transition model, validated for high Reynolds numbers, supports the design process and helps to model effects observed in free flight and wind tunnel experiments.

2 Boundary Layer Transition

2.1 Transition Process

A boundary layer develops on any body moving through a fluid. The fluid will be at rest at the wall and the fluid velocity increases towards the freestream. Figure 2.1 depicts the transition process on a flat plate. A laminar boundary layer develops downstream of the stagnation point. The fluid flow inside the boundary layer is orderly and laminar. There is only little exchange of mass and momentum between adjacent layers of the boundary layer flow.

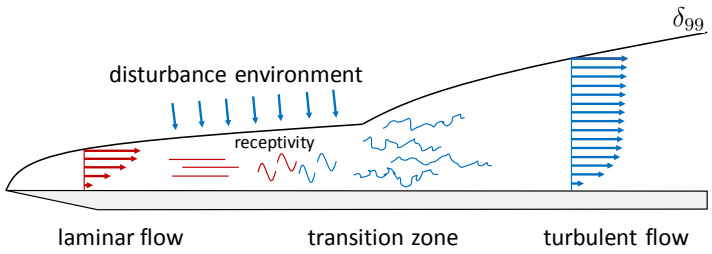

Figure 2.1: Transition process on a flat plate

The freestream or the wall provides a disturbance environment that acts on the boundary layer. Disturbances are e.g. sound waves, velocity fluctuations, or wall roughness. The laminar boundary layer will show receptivity for some disturbances provided by the disturbance environment acting on the boundary layer. At some point, disturbances of a certain frequency and wave length cause undamped oscillations of the boundary layer flow. As the oscillations grow, the laminar boundary layer undergoes transition to a fully turbulent state. The fluid flow inside the boundary layer is no longer orderly and the mass and momentum exchange between adjacent layers of the fluid is increased.

2.2 Receptivity

The process in which disturbances from the freestream (e.g. sound or vorticity) or other disturbances (e.g. wall roughness) enter the boundary layer is called receptivity (Saric et al. 2002).

The name receptivity for the first stage in the transition process is introduced by Morkovin (1969). A main part of the receptivity process is the transformation of freestream (or other) disturbances into small-amplitude perturbations inside the boundary layer (Schmid and Henningson 2001).

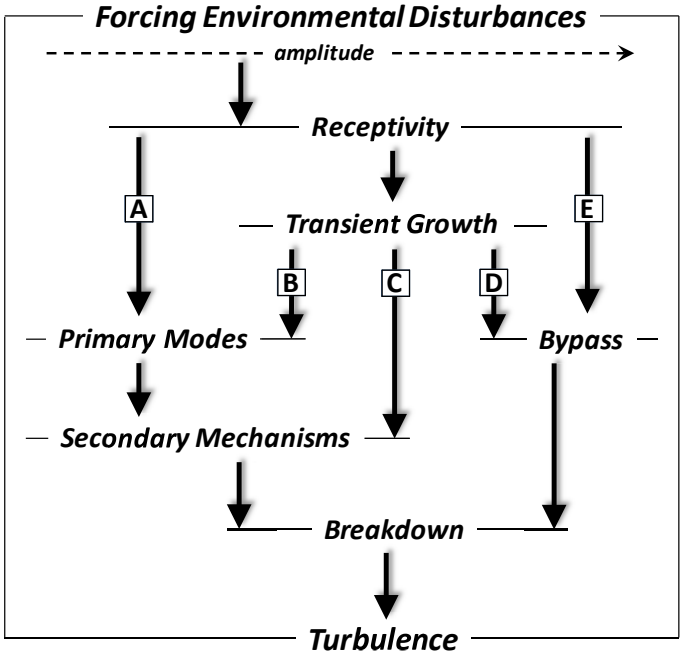

Figure 2.2: Receptivity and transition mechanisms. Adapted from Saric et al. (2002).

Figure 2.2 depicts a simplified overview of different paths to turbulence as presented by Saric et al. (2002): Environmental disturbances enter the laminar boundary layer through a receptivity process. For a weak disturbance environment, the transition process follows path A. This transition mechanism is called Tollmien-Schlichting transition. The growth of disturbances is weak and occurs over a long streamwise length. It is influenced by pressure gradients, temperature gradients, etc. (Saric et al. 2002).

If the freestream provides the right initial conditions, transient growth can occur. In the case of transient growth, two stable boundary layer modes interact. Transient growth can lead to a spanwise modulation of two-dimensional waves (path B), directly to secondary instabilities (path C), or to a bypass (path D) of the preliminary stages in the transition process (Saric et al. 2002).

For very strong freestream disturbances, the linear disturbance growth is bypassed without a transient growth mechanism and the boundary layer flow becomes directly turbulent (path E). The transition mechanism associated with a strong disturbance environment is called bypass transition.

2.3 Transition Mechanisms

2.3.1 Tollmien-Schlichting Transition

Tollmien-Schlichting transition (T-S transition) or natural transition is given by path A in Fig. 2.2. The transition mechanism is named after W. Tollmien and H. Schlichting. According to Schlichting and Gersten (2006), natural transition is characterized by the following stages (compare Fig 2.3):

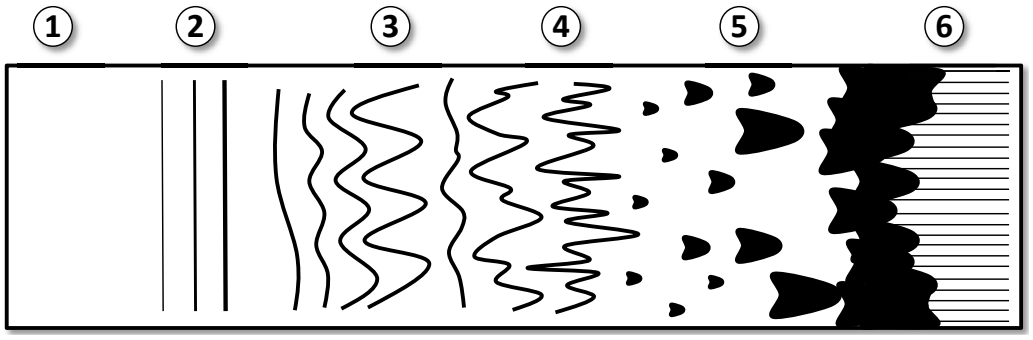

Figure 2.3: Stages of Tollmien-Schlichting transition on a flat plate according to Schlichting and Gersten (2006)

1. The laminar boundary layer flow is stable and small disturbances inside the boundary are damped.

2. Disturbances inside the boundary layer are no longer damped and 2-dimensional Tollmien-Schlichting waves develop. This point is given by the indifference Reynolds number Re_{ind}.

3. Secondary instabilities grow nonlinearly into 3-dimensional disturbances. Characteristic Λ-structures develop inside the boundary layer.

4. The vortex structures break down into smaller and smaller vortices (Arnal 1984).

5. Turbulent spots develop and grow inside the boundary layer. A turbulent spot is a fully turbulent flow region inside the laminar boundary layer.

6. The growing turbulent spots accumulate downstream and give a fully turbulent boundary layer. This point is given by the critical Reynolds number Re_{crit}.

The development of a theory of natural transition began at the end of the 19^{th} century but it took almost 50 years to establish the theory by experimental evidence. John William

Strutt, 3rd Baron Rayleigh, developed a stability equation for small disturbances in parallel inviscid flow, today known as Rayleigh equation (Rayleigh 1879, 1887). William McFadden Orr (Orr 1907a, b) and Arnold Sommerfeld (Sommerfeld 1908) developed independently an equation governing the stability of parallel viscous flow, today known as Orr-Sommerfeld equation. Based on the work of Ludwig Prandtl and Oskar Tietjens, Walter Tollmien (1929) was the first to compute the neutral eigenvalue for a continuous profile (plane Poiseuille flow). Based on Tollmien's work, Hermann Schlichting (Schlichting 1933) was able to determine the amplification for the most unstable frequencies.

The predicted instability waves, referred to as Tollmien-Schlichting waves, and the linear stability theory received little acceptance because there was no experimental evidence that these instability mechanism actually exist (Arnal 1984). This changed with the experimental results of Schubauer and Skramstad (1948): In the 4½-foot wind tunnel at the National Bureau of Standards at turbulence levels as low as 0.032 %, two-dimensional instability waves were detected. Small disturbances are able to excite these normal modes of the laminar boundary layer only in a low turbulence environment (Arnal 1984). Therefore, the existence of T-S waves was masked in earlier wind tunnel experiments with higher freestream turbulence levels (Morkovin 1969).

2.3.2 Bypass Transition

Bypass transition is a transition mechanism at high freestream disturbance levels. It is given by path E in Fig. 2.2. Primary modes and secondary mechanisms of the Tollmien-Schlichting transition process are bypassed. The forcing environment interacts with the laminar boundary layer and turbulent spots are directly produced inside the laminar boundary layer (Mayle 1991).

Suder et al. (1988) conducted experiments to determine the effect of the freestream turbulence level on bypass transition. Tollmien-Schlichting waves are detected for turbulence levels of 0.3 %. At a turbulence level of 0.65 %, the T-S path is already bypassed. For turbulence levels above 3 %, sudden turbulent bursts occur. At these turbulence levels the laminar flow shows a sudden change to a fully turbulent state.

The turbulent bursts occur over the entire boundary layer thickness and the convective velocity of the turbulent spots is about 70 % of the boundary layer edge velocity (Mayle 1991). A further description of these turbulent bursts or spots is given in Section 2.4.

2.3.3 Separated-Flow Transition

A laminar boundary layer is more likely to separate compared to a fully turbulent boundary layer. The turbulent mixing inside the turbulent boundary layer increases the shear stress and delays the detachment of the boundary layer. A laminar separation might occur due to adverse pressure gradients or at sharp corners of a geometry. In the case of a laminar separation, transition to turbulence occurs in the shear-layer flow. The length of the bubble is determined by the type of transition inside the shear layer (Mayle 1991).

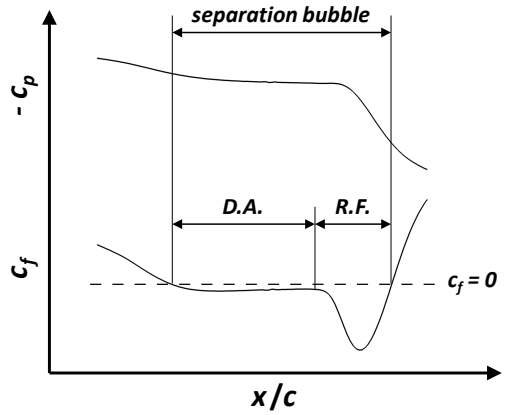

Figure 2.4: Pressure and skin friction coefficient across a laminar separation bubble (D.A – dead air region, R.F. – reverse flow vortex)

Figure 2.4 depicts the pressure coefficient c_p and the skin friction coefficient c_f over a laminar separation bubble in an adverse pressure gradient flow[1]. At the separation and reattachment point, the wall shear stress and the skin friction coefficient vanish as $(\partial u/\partial y)_w = 0$. Downstream of the separation point, the free shear layer is laminar and the viscous shear stress is low. As the shear layer flow is not capable to overcome an adverse pressure gradient, a plateau in the pressure distribution develops (Horton 1968). A dead air region exists downstream of the separation point. Towards the reattachment point a strong reverse flow vortex is found. According to Horton (1968), the maximum reverse velocities are in the order of 20 % of the freestream velocity.

After transition takes place, the effect of turbulent entrainment will enable the flow to overcome a certain pressure gradient and eventually to reattach. However, once the pressure rise is too strong, the flow stays separated. Based on their effect on the pressure distribution, two types of separation bubbles are defined (Mayle 1991): Short bubbles only have a local effect on the pressure distribution; long bubbles change the whole pressure distribution and interact

[1]The figure is produced from CFD results.

with the flow outside the boundary layer. The process in which a small bubble suddenly changes to a long bubble is called "bursting". Bubble bursting leads to dramatic lift losses or to a stalled flow condition (Mayle 1991).

2.3.4 Crossflow Transition

Crossflow transition (CF transition) is a transition mechanism in a three-dimensional boundary layer flow. An extensive overview of crossflow transition is given by Bippes (1999) and Saric et al. (2003).

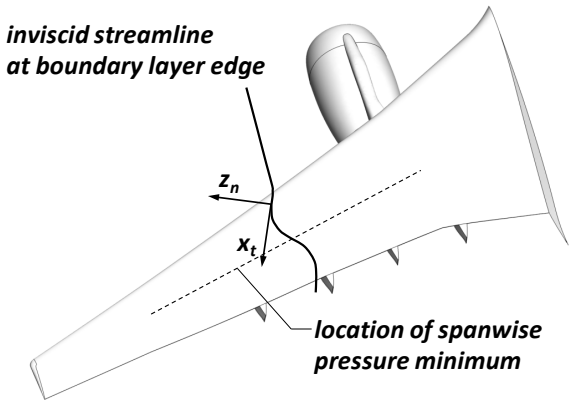

Figure 2.5: Inviscid three-dimensional flow over a swept wing

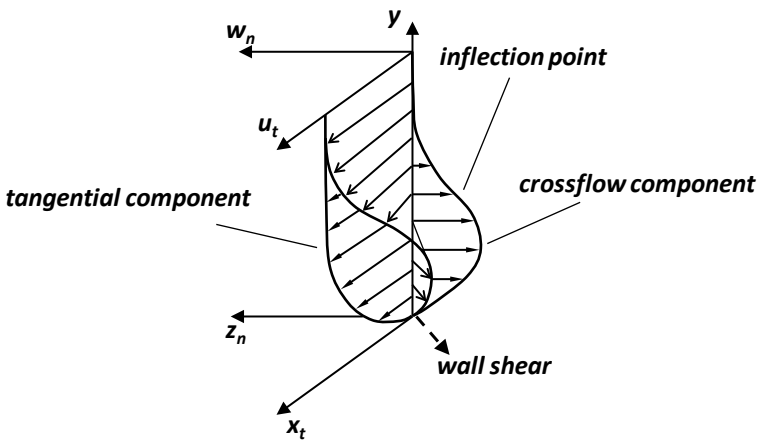

Figure 2.6: Three-dimensional velocity profile. Figure based on Saric et al. (2003); Arnal and Casalis (2000).

The pressure gradient and geometric sweep result in a s-shaped inviscid streamline at the edge of the boundary layer on a swept wing (Boiko et al. 2002). Figure 2.5 depicts the inviscid

streamline at the boundary layer edge qualitatively. Inside the boundary layer, the velocity decreases towards the wall as well as the centrifugal force acting on the fluid element. The pressure stays in first approximation constant. This excess of pressure forces on the fluid element produces a crossflow component in the velocity profile (Bippes 1999; Saric et al. 2003).

Figure 2.6 depicts the crossflow velocity profile upstream of the pressure minimum in a three-dimensional boundary layer. The tangential velocity component is in direction of the inviscid boundary layer edge streamline. In addition to the tangential velocity, a crossflow velocity component exists perpendicular to the inviscid boundary layer edge flow direction.

The crossflow component has to vanish at the wall and at the boundary layer edge. Therefore, the crossflow velocity profile is inflectional (Saric et al. 2003). Rayleigh's Inflection Point Theorem (Rayleigh 1879) states that an inflection point in the mean velocity profile is a necessary condition for any inviscid instability to occur. Later, Tollmien (1935) showed that an inflection point is a sufficient condition for the existence of unstable modes. The inflection point in the crossflow component provides the source for an inviscid instability. This instability results in co-rotating stationary vortices, whose axes are aligned with the local inviscid streamlines (Saric et al. 2003). The vortices produce the characteristic jagged pattern of the transition zone for crossflow transition (see e.g. Fig. 44 to 48 in the report by Dagenhart and Saric 1999).

2.3.5 Attachment Line Transition

Attachment line transition (ALT) is a transition mechanism along the leading edge of a swept wing. Figure 2.7 gives the basic concept of an attachment line flow on a swept wing. At the attachment (or stagnation) line of the wing, a spanwise flow develops with a boundary layer edge velocity W_{alt} given by the freestream velocity and the sweep angle of the leading edge:

$$W_{alt} = U_\infty \sin(\Lambda_{LE}) \tag{2.1}$$

A turbulent contamination introduced by the fuselage, an engine pylon, a small roughness element, or a surface imperfection can disturb the laminar boundary layer in the mean flow direction but also the spanwise attachment line flow. A spanwise turbulent attachment line flow will eventually give a fully turbulent flow outboard[2] of the contamination in the mean flow direction and along the attachment line (see e.g. Gregory 1960). The negative effect of wing sweep on a laminar flow is first reported by Gray (1952).

Pfenninger (1965) determined a critical leading edge momentum loss thickness Reynolds

[2]In the case of a backward swept wing.

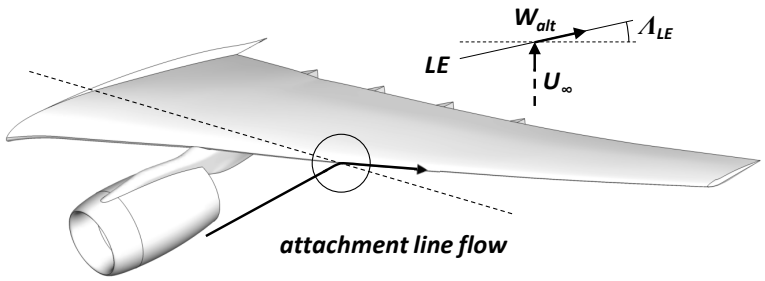

Figure 2.7: Attachment line flow on a swept wing

number to define the condition for which an attachment line flow is turbulent:

$$Re_{\theta alt} = \frac{\rho W_{alt} \theta_{alt}}{\mu} \tag{2.2}$$

The critical leading edge momentum loss thickness Reynolds number is based on the attachment line flow velocity in the freestream W_{alt} and the local attachment line momentum loss thickness θ_{alt}. At $Re_{\theta alt} = 90$ to 105 turbulent bursts develop along the attachment line. For $Re_{\theta alt} > 104$ [sic] the boundary layer is fully turbulent in spanwise and chordwise direction (Pfenninger 1965).

2.3.6 Relaminarization

Transition from a turbulent to a laminar boundary layer flow is called relaminarization or reverse transition (Mayle 1991). A first systematic experiment is described by Launder (1964b) and Launder (1964a): The boundary layer reverts to a laminar state and the resulting boundary layer flow does not differ in any essential feature from a normal laminar state (Launder 1964a). However, the process of relaminarization is gradual and the laminar boundary layer is not necessarily completely recovered if the acceleration is not sufficient (Launder 1964b).

According to Launder (1964b) the acceleration provides a stabilizing effect in the experiment by the overall environment (favorable pressure gradient) and by reducing the momentum loss Reynolds number. The turbulent boundary layer departs from the universal law of the wall under strong acceleration and viscous effects increase inside the boundary layer. At some point the laminar sublayer starts to grow at the expense of the turbulent outer layer. Launder (1964b) stresses that this explanation is solely based on mean velocity profiles and the change in the turbulence characteristics has to be considered as well.

Based on considerations on departure from the logarithmic law, Launder (1964a) deduces that a relaminarization of the turbulent boundary layer can be expected at magnitudes of the

acceleration parameter $K = \frac{\nu}{U^2}\frac{dU}{dx} \approx 10^{-6}$. Later a value of $K > 3 \cdot 10^{-6}$ is established to predict a relaminarization of the boundary layer (Jones and Launder 1972; Mayle 1991).

2.4 Transition Zone Length and Intermittency

Transition takes place over a finite length inside the boundary layer. The length of the transition zone will be defined as the length between the first disturbance growth and the fully developed turbulent boundary layer. For Tollmien-Schlichting transition, two-dimensional disturbances develop at the indifference Reynolds number Re_{ind}. The end of the transition process is given at the critical Reynolds number Re_{crit} with a fully turbulent boundary layer (Schlichting and Gersten 2006). However, the first disturbance growth is hard to detect and will most likely not alter the mean flow. Therefore, definitions of start and end of the transition zone differ between different authors.

The length of the transition zone depends strongly on the forcing environment and therefore on the transition mechanism: A bypass transition mode will result in a shorter transition zone length as the disturbance development is bypassed compared to Tollmien-Schlichting transition.

One of the earliest descriptions of the transition zone length is given by Dryden (1937). In a flat plate experiment, transition zone length Reynolds numbers Re_x up to 200 000 are found. The Reynolds number at transition onset is determined by a comparison of measured velocity profiles with the theoretical Blasius velocity distribution. However, an increase of velocity fluctuations inside the boundary layer occurs at a considerably lower Reynolds number. In addition, it is found that fully turbulent regions occur intermittently inside the transition zone. The occurrence of such turbulent regions is termed transition point by Dryden (1937) and a wide movement of the transition point is reported.

It took almost 15 years and an incidental observation to shed some light on the observed transition behavior: In a water-table analogy to supersonic flow for demonstration purposes at Harvard University, transition on a flat plate is obtained. The appearance of tiny turbulent spots at some random instant and point is observed in the thin layer of water. These turbulent spots grow as they are washed down the plate (Emmons 1951).

Emmons (1951) interprets the turbulent bursts described by e.g. Schubauer and Skramstad (1948) or Dryden (1937) as turbulent spots passing over the measurement probe. Emmons (1951) gives a statistical transition theory based on the turbulent spot production and propagation. The method gives a quantitative prediction for the fraction of time a point in the boundary layer is turbulent.

This fraction of time is called intermittency, usually denoted by γ. Emmons (1951) assumes

that the local skin friction coefficient in the transition region is given as a superposition, based on the intermittency and the laminar and turbulent friction coefficients:

$$c_f = c_{fL}\,(1-\gamma) + c_{fT}\gamma \tag{2.3}$$

Based on the experimental data of Schubauer and Klebanoff (1955), the intermittency concept is further developed by Dhawan and Narasimha (1958). Although there is a vast amount of literature on transition zone length and intermittency models (Abu-Ghannam and Shaw 1980; Narasimha 1985; Narasimha and Dey 1989; Mayle 1991), the development of the transition zone is often discarded in transition models for engineering purposes.

2.5 Influence Parameters on Transition

2.5.1 Overview of Parameters

The transition onset is determined by the disturbance environment that acts on the boundary layer flow. Any parameter that changes this environment will have an effect on the transition onset and the transition mode. Abu-Ghannam and Shaw (1980) give a list of parameters affecting boundary layer transition:

- freestream turbulence
- pressure gradients
- Reynolds number
- Mach number
- acoustic radiation
- surface roughness
- surface temperature
- surface curvature
- the history effect of the above

For some of these parameters a large body of experimental and theoretical work can be found. For others no quantifiable data are available. In addition, in almost every experimental test more than one of the above mentioned parameters is present.

The effect of the freestream turbulence level, pressure gradient, and compressibility is described shortly in the following section. A further insight requires an understanding of the specific receptivity mechanism and the interaction with the relevant transition modes, which is beyond the scope of this work.

2.5.2 Freestream Turbulence Level

Any external flow shows fluctuations in its pressure, velocity, density, and temperature field. The amplitudes of the fluctuations have a strong effect on the development of any boundary layer as seen from Fig. 2.2. Higher amplitudes in the forcing environment change the transition mechanism and the transition onset. To describe the amount of turbulence in the flow field, a turbulence level is defined based on the velocity fluctuations $u^{'}$, $v^{'}$, and $w^{'}$ (Schlichting and Gersten 2006):

$$Tu = \frac{\sqrt{\frac{1}{3}\left(\overline{u'^2} + \overline{v'^2} + \overline{w'^2}\right)}}{U_\infty} \tag{2.4}$$

The turbulence level Tu is often given in percent. To indicate which value is meant, τ is used at this point whenever a value in percent is considered:

$$\tau = \frac{\sqrt{\frac{1}{3}\left(\overline{u'^2} + \overline{v'^2} + \overline{w'^2}\right)}}{U_\infty} \cdot 100\,\% \tag{2.5}$$

In general, the turbulence in a flow is anisotropic so that fluctuations differ in each spatial direction: $\overline{u'^2} \neq \overline{v'^2} \neq \overline{w'^2}$ (Fröhlich 2006). The anisotropic characteristic is strongest for fluctuations of low frequency, i.e. small wavenumbers, which contribute most to the turbulent kinetic energy $k = 1/2\left(\overline{u'^2} + \overline{v'^2} + \overline{w'^2}\right)$ of the flow (Herwig 2008). In the case of isotropic turbulence, which is assumed in eddy viscosity turbulence models (Fröhlich 2006), the fluctuations are of equal size in every direction $\overline{u'^2} = \overline{v'^2} = \overline{w'^2}$ and the turbulence level is given by

$$Tu = \frac{\sqrt{\overline{u'^2}}}{U_\infty}. \tag{2.6}$$

For applications in external aerodynamics, turbulence levels $\tau \leq 0.1$ % are most important. High quality wind tunnels show turbulence levels of about $\tau \approx 0.1$ % and in free flight the turbulence level is even lower (Schlichting and Gersten 2006). Although a simple value like Tu or τ is very descriptive, it is still a gross simplification of what turbulence actually resembles. As Kundu et al. (2012) state:

> "[The] *idea of a spectral energy cascade is at the heart of our present understanding of turbulence.*" (Kundu et al. 2012, p. 545).

The idea of an energy cascade is first introduced by Lewis Richardson and later quantitative described by A. N. Kolmogorov. According to Richardson, turbulent kinetic energy is constantly transferred from large to small eddies. The turbulent kinetic energy is lost by viscous dissipation on the smallest scales (Kundu et al. 2012).

In most cases, the momentum thickness Reynolds number at the transition onset $Re_{\theta t}$ is correlated to the freestream turbulence level τ:

$$Re_{\theta t} = \frac{\rho\, U\, \theta_t}{\mu} = f(\tau) \tag{2.7}$$

According to Liepmann (1945), the momentum loss Reynolds number Re_θ is an appropriate parameter to describe boundary layer transition data as it is closely connected to the slope of the velocity profile inside the boundary layer. The instability of the laminar boundary layer depends strongly on the velocity profile (see Section 2.5.3). In addition, the momentum loss thickness can be calculated more accurately than other boundary layer quantities by boundary layer calculation methods (Hall and Gibbings 1972).

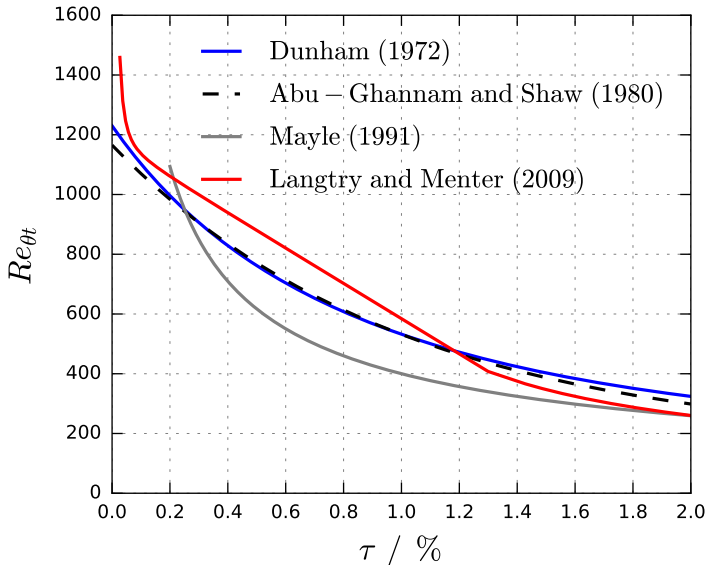

Figure 2.8: Effect of freestream turbulence level on the transition onset Reynolds number

The basic effect of a turbulence increase is to decrease the transition onset Reynolds number for a given transition mechanism (e.g. T-S transition). Moreover, the transition mechanism

can change as the amplitudes of the disturbance environment grow (e.g. from T-S to bypass transition). Different correlations for zero-pressure gradient flows are depicted in Fig. 2.8.

For turbulence levels below 1 %, the experimental data and the transition onset correlations scatter strongly. Furthermore, experimental results from different sources are often obtained by different measurement techniques and different definitions of the transition onset. Hall and Gibbings (1972) give a broader insight into these problems as they review and discuss experimental results and different methods to define transition parameters from various authors.

2.5.3 Pressure Gradient

The pressure gradient has a strong influence on the boundary layer stability. This can already be seen by considering the velocity profile for different pressure gradients. A laminar boundary layer under a positive (adverse) pressure gradient shows an inflection point, a boundary layer under a negative (favorable) pressure gradient is inflection point free. As described in Section 2.3.4, Rayleigh (1879) and later Tollmien (1935) showed that an inflection point is a necessary and sufficient condition for an inviscid instability of the laminar boundary layer. The inflection point free boundary layer under a favorable pressure gradient is stable for $Re \rightarrow \infty$. For finite Reynolds numbers, an indifference Reynolds number exists, which is caused by a viscous instability (Schlichting and Gersten 2006).

For positive pressure gradients exist sufficient experimental data to show the strong destabilizing effect of the pressure gradient and most authors present correlations with qualitatively similar results. For negative pressure gradients, the experimental data scatter and disagreement exists on how to quantify the stabilizing effect.

Different non-dimensional parameters exist to describe pressure gradients in a flow (Brown and Martin 1976):

$$\text{Pohlhausen parameter:} \quad \Lambda \equiv \frac{\delta^2}{\nu}\frac{dU}{dx} \tag{2.8}$$

$$\text{pressure gradient parameter:} \quad \lambda_\theta \equiv \frac{\theta^2}{\nu}\frac{dU}{dx} \tag{2.9}$$

$$\text{acceleration parameter:} \quad K \equiv \frac{\nu}{U^2}\frac{dU}{dx} \tag{2.10}$$

The acceleration parameter K quantifies the acceleration in the freestream and is easily obtained in an experimental facility (Mislevy and Wang 1995). It is related to the other parameters by the boundary layer Reynolds numbers: $\Lambda = K \cdot Re_\delta^2$ and $\lambda_\theta = K \cdot Re_\theta^2$. According to Mayle (1991), the acceleration parameter is the appropriate parameter to describe transition in accelerated flows with bypass transition. The pressure gradient parameter λ_θ is expected to

describe Tollmien-Schlichting transition as it includes information on the boundary layer profile given by θ (Mayle 1991).

From stability analysis it is possible to obtain a stability limit for a boundary layer flow. By solving the Orr-Sommerfeld equation it is possible to determine the indifference Reynolds number Re_{ind}, above which first undamped solutions exist. These values can be considered as a stability limit (see e.g. Wazzan et al. 1968). For Reynolds numbers below the stability limit, no amplification of disturbances is possible for any Tollmien-Schlichting transition mode.

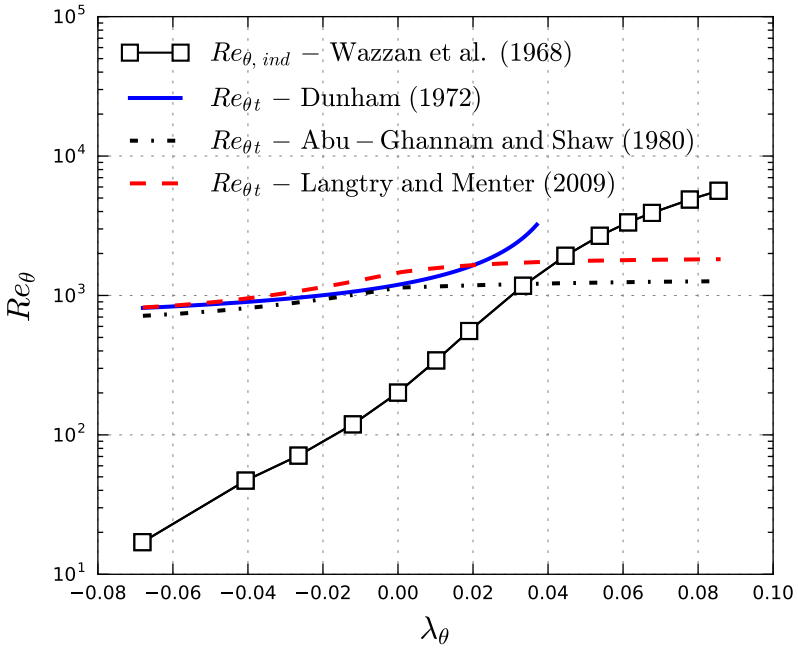

Figure 2.9: Effect of pressure gradients on the transition onset Reynolds number $Re_{\theta t}$ for $\tau = 0.027$ %

Figure 2.9 depicts the stability limit given by Wazzan et al. (1968) and the correlations given by Langtry and Menter (2009), Abu-Ghannam and Shaw (1980), and Dunham (1972). The empirical correlations are depicted for $\tau = 0.027$ %, which is the lowest turbulence level assumed by Langtry and Menter (2009).

The correlations given by Abu-Ghannam and Shaw (1980) and Langtry and Menter (2009) cross into the stable region for favorable pressure gradients. The focus of the correlation of Abu-Ghannam and Shaw (1980) is on flows with high turbulence levels. In high turbulence level flows, the effect of acceleration is negligible (Mayle 1991) and the stability limit is not relevant as Tollmien-Schlichting transition is bypassed.

The correlation of Dunham (1972) is more appropriate for transition in a low turbulence environment as the stability limit is not crossed. Similar correlations are presented by Liepmann

(1945); Crabtree (1958); Hall and Gibbings (1972); Seyb (1972); Singh (1974).

Mayle (1991) states that the stabilizing effect of acceleration is significant in cases of low turbulence levels. The effect of pressure gradients on boundary layer transition has to be discussed in relation to the turbulence level. Pressure gradient effects for a bypass transition mode will deviate strongly from a Tollmien-Schlichting mode as the presented data suggest.

2.5.4 Compressibility

Mack (1975), Narasimha (1985), and Mayle (1991) state that there is a lack of flat plate transition data for high Mach number flows. An increase in Mach number is usually connected to a change in the disturbance environment. Therefore, it is hardly possible to separate the influence of compressibility from other influence parameters on transition.

A first insight can be obtained by considering theoretical results. Mack (1975) presents amplitude growth curves from linear stability theory for increasing Mach numbers. The results by Mack (1975) and Arnal (1989) show a strong stabilizing effect of compressibility for transonic flows, a destabilizing effect for Mach numbers $M = 2$ to 3, and a stabilizing effect for hypersonic flows.

In subsonic flow, 2-dimensional disturbances are most unstable for Tollmien-Schlichting transition, which is described by Squire's Theorem:

> "*If an exact two-dimensional parallel flow admits an unstable three-dimensional disturbance for a certain value of the Reynolds number, it also admits a two-dimensional disturbance at a lower value of the Reynolds number.*"(Criminale et al. 2003, p.39)

For compressible flows, Squire's Theorem no longer holds and 3-dimensional disturbances become more unstable (Arnal 1989). The wave number direction ψ of the most amplified disturbance changes with increasing Mach number. The wave number direction ψ is the direction normal to the wave crests given by the real parts of the wave numbers α_r and β_r (Arnal 1989):

$$\tan\psi = \beta_r/\alpha_r \tag{2.11}$$

As the Mach number increases, the maximum amplification is found for $\psi \neq 0°$ and 3-dimensional disturbances can no longer be discarded.

For transonic Mach numbers, there is hardly any data available that shows the single effect of compressibility, predicted by linear stability theory. Fisher and Dougherty (1982) present transition locations from free flight experiments for transonic Mach numbers. The transition onset Reynolds number shows the behavior, predicted by the linear stability theory. However, as

the Mach number increases the disturbance environment gets weaker. Therefore, the stabilizing effect can not be solely attributed to compressibility.

Narasimha (1985) points out that transition in low speed wind tunnel tests is often driven by freestream turbulence. In high speed tunnels, noise radiated from turbulent wind tunnel wall boundary layers is the main driver. Therefore, direct comparisons between low and high speed wind tunnels are problematic and might be misleading as the receptivity mechanism changes. Based on some experimental data, Narasimha (1985) proposes an increase of the transition onset Reynolds number $Re_{xt,\,comp}$ of

$$Re_{xt,\,comp} = \left(1 + 0.38\, M_\infty^{0.6}\right) Re_{xt,\,incomp} \tag{2.12}$$

or in terms of the momentum loss Reynolds number:

$$Re_{\theta t,\,comp} = \sqrt{1 + 0.38\, M_\infty^{0.6}}\, Re_{\theta t,\,incomp} \tag{2.13}$$

for $0.2 \leq M \leq 2.4$ and freestream turbulence levels of $0.1\ \% \leq \tau \leq 3\ \%$. Equation 2.12 gives a much lower stabilizing effect than the results predicted by Mack (1975) and Arnal (1989). Without any well defined wind tunnel tests on the single effect of compressibility, the quantifiable effect of a Mach number increase stays mere speculation.

2.6 Unsteady Boundary Layer Transition

Boundary layer transition is affected by an unsteady base flow and by an unsteady disturbance environment. Any changes in the flow conditions might be periodic or singular events (e.g. gust encounters). Periodic-unsteady transition is of high importance in gas turbines as the flow is periodically unsteady. Turbulent wakes from an upstream rotor, stator, or trailing edge shocks disrupt the laminar flow and cause a turbulent boundary layer region, which grows and propagates downstream (Mayle 1991).

Unsteady flow effects also arise from the movement of airfoils and wings in a given, otherwise steady flow. Helicopter rotor blades encounter periodic pitch and heave motion in forward flight (Leishman 2000). The blades are designed to have large laminar flow regions for drag reduction and experiments focus on the effect of boundary layer transition for large pitch amplitudes $\widehat{\alpha} > 1°$ on attached and stalled flow conditions (Richter et al. 2014).

Flapping wing propulsion of micro aerial vehicles (MAV) require a combined pitch and heave motion of the wing (Radespiel et al. 2007). The aerodynamic performance of an MAV in the low Reynolds number range $Re \ll 10^6$ is largely determined by laminar separations and the

transition process following the boundary layer separation (Lian and Shyy 2007). Hence, the prediction of the unsteady transition behavior of separated flows is highly important.

In addition, airfoil and wing flutter is determined by the aerodynamic response to small motions of the structure in the airstream. Forced motion experiments (Hebler 2013) and computations (Fehrs et al. 2015) are used to investigate the flutter stability. For airfoil flutter calculations, the response to small harmonic pitch and heave motion is considered with amplitudes $\hat{\alpha} \ll 1°$. Adequate methods to predict the unsteady transition behavior are required for these conditions.

As Radespiel et al. (2007) and Richter et al. (2014) point out, there is little published on models for unsteady transition prediction and information on the unsteady transition behavior is often drawn from wind tunnel experiments. One exception is the unsteady e^N method presented by Radespiel et al. (2007) and Windte and Radespiel (2008). The unsteady e^N method uses a novel integration scheme to obtain the required N factors by considering the temporal evolution of amplification rates in the unsteady laminar boundary layer (Bansmer et al. 2010). The difference between steady and unsteady transition prediction increases with reduced frequency of the motion. Large differences exist for $k = \omega\, c/2\,/\,U_\infty = 1$ (Windte and Radespiel 2008).

Krumbein et al. (2011) included and tested the unsteady e^N method by Radespiel et al. (2007) and Windte and Radespiel (2008) in the TAU transition module. Light and deep stall test cases for the OA209 airfoil are used to investigate the unsteady transition prediction by different simulation approaches. First, a steady boundary layer code is used to compute the boundary layer profiles based on the RANS pressure distribution for the pitching airfoil. The boundary layer profiles are evaluated with the standard e^N method. Neither the boundary layer code, nor the standard e^N method account for the unsteady base flow. Second, the boundary layer profiles are taken directly from the TAU-Code and the stability analysis is based on the standard e^N method. For this approach, the velocity profiles account for the unsteady boundary layer flow, but the transition prediction method is steady. The third approach is given by the unsteady RANS boundary layer data and the unsteady e^N method. In addition, the γ-Re_θ transition model is used (Krumbein et al. 2011).

The fully steady transition prediction approach gives results similar to a fully turbulent approach. The approaches based on the unsteady RANS data and either e^N method give qualitatively similar results. It remains unclear if the steady e^N method is sufficient for dynamic stall applications. The γ-Re_θ transition model results resemble the steady e^N method results for unsteady boundary layer data (Krumbein et al. 2011).

Different authors use steady transition prediction methods for unsteady applications: Lian

and Shyy (2007) investigate the aerodynamics of a MAV ($Re = 60\,000$). The experimental data by Radespiel et al. (2007) are compared to RANS results using a steady transition prediction approach based on an e^N method. The predicted transition behavior is considered good but no final assessment for a general applicability is made as more tests are required (Lian and Shyy 2007).

Bansmer et al. (2010) study a birdlike airfoil to investigate the influence of flexibility on the propulsive efficiency of flapping wings ($Re = 100\,000$). The transition behavior is driven by laminar separation bubbles. The experimental results are supported by RANS computations. For transition prediction in most of the cases, a steady e^N method is used for the unsteady computations. According to Bansmer et al. (2010), the predicted transition behavior is slightly improved by applying the unsteady transition prediction presented by Radespiel et al. (2007).

Yuan et al. (2015) use the γ-Re_θ transition model for the prediction of limit-cycle oscillations (LCO) of a NACA 0012 airfoil ($Re = 77\,000$). According to Yuan et al. (2015), the γ-Re_θ transition model is advantageous for the prediction of LCO related to laminar separations in strong disturbance environments (bypass transition mode). However, Yuan et al. (2015) only show some qualitative agreement but uncertainties exist regarding the influence of the turbulence level on the LCO amplitudes in the computations.

3 Aeroelasticity

3.1 Dynamic Aeroelastic Stability: Flutter

Flutter is "*the dynamic instability of an elastic body in an airstream*" and it occurs above a critical airspeed, for which the structure exhibits sustained, harmonic oscillations (Bisplinghoff et al. 1996, p. 527). For speeds above this neutral stability boundary, the oscillations of the structure grow exponentially.

Flutter is induced by the aerodynamic forces, which is only possible if energy is extracted from the airstream into the structure. For an airfoil undergoing pure heave motion, the oscillation is always stable in an inviscid, incompressible flow as the airfoil loses energy to the airstream. The pitch motion can be unstable for certain combinations of mass distribution and location of the elastic axis (Fung 2002). For a 2-degree-of-freedom system, the stability is determined by the phase lag between the heave and pitch motion, and the frequency of the motion.

Figure 3.1 depicts an airfoil undergoing a combined pitch and heave motion. For simplification, quasi-steady airloads are assumed, for which lift and moment correspond to the steady values. Two cases are depicted for different phasing between both modes (Freymann 2011).

In case I, pitch and heave are in phase as the maximum deflection in heave corresponds to the maximum pitch position. During the first and third quarter of the cycle, the aerodynamic lift and the heave motion are in the same direction. Energy is transferred from the airstream into the airfoil. However, during the remaining time of the cycle, lift and motion are opposed and energy is withdrawn. The overall energy balance is zero and the system is stable. In case II, the pitch mode leads the heave mode by $+90°$. Over the whole cycle, energy is extracted from the freestream and the airfoil will encounter flutter at some critical airspeed.

In general, flutter is characterized by the interaction of two or more degrees-of-freedom. The complexity of the mode-interaction requires a stability analysis that includes a description of the structural model and the unsteady, aerodynamic airloads.

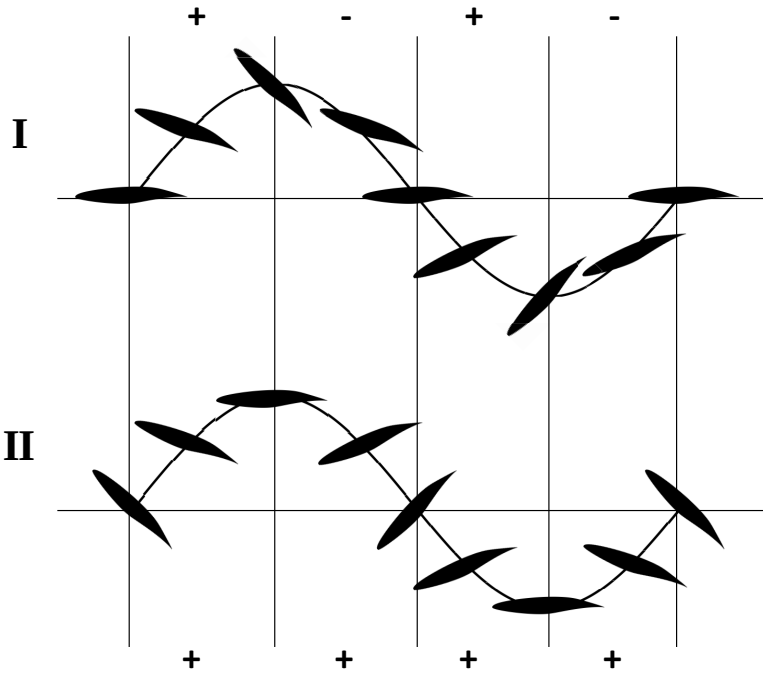

Figure 3.1: Energy balance for different phasing between heave and pitch motion (adapted from Freymann 2011)

3.2 Unsteady Aerodynamics

The unsteady aerodynamic forces acting on an airfoil or wing depend on Mach number, Reynolds number, and frequency of the unsteady motion: $Q_i = f\,(Re,\, M,\, \omega)$ (Leishman 2000). The frequency ω is described in terms of the reduced frequency k:

$$k = \frac{\omega\, c}{2\, U_\infty} = \frac{\omega\, b}{U_\infty} \tag{3.1}$$

Leishman (2000) gives the following characteristics for unsteady flows and reduced frequency: The flow is steady for $k = 0$. In the range $0 < k \leq 0.05$, the flow is quasi-steady and unsteady effects are small. Flows with reduced frequencies of $0.05 < k \leq 0.2$ are unsteady and unsteady effects can not be neglected. For frequencies $k > 0.2$, the flow is highly unsteady and the unsteady airloads dominate the aerodynamics.

A first theoretical description of the unsteady airloads on an oscillating airfoil is given by Theodorsen (1935). Theodorsen's theory describes the airloads on a harmonically oscillating airfoil in inviscid, incompressible flow (Leishman 2000). A description of the basic concept is given by Bisplinghoff et al. (1996); Fung (2002); Wright and Cooper (2007); Leishman (2000).

The Theodorsen aerodynamic represents the transfer function between the airfoil motion

(e.g. pitch or heave) and the aerodynamic response in terms of lift L and moment M_y (Leishman 2000):

$$\begin{aligned} L &= \pi\rho U_\infty^2 b\left(\frac{b}{U_\infty^2}\ddot{h} + \frac{b}{U_\infty}\dot{\alpha} - \frac{b^2}{U_\infty^2}e\,\ddot{\alpha}\right) \\ &\quad +2\pi\rho U_\infty^2\, b\left(\frac{\dot{h}}{U_\infty} + \alpha + \frac{b\,\dot{\alpha}}{U_\infty}\left[\frac{1}{2} - e\right]\right) C(k) \end{aligned} \tag{3.2}$$

$$\begin{aligned} M_y &= -\rho\, b^2\left(\pi\left[\frac{1}{2} - e\right] U_\infty\, b\,\dot{\alpha} + \pi\, b^2\left[\frac{1}{8} + e^2\right]\ddot{\alpha} - e\,\pi\, b\,\ddot{h}\right) \\ &\quad +2\pi\rho\, U_\infty\, b^2\left(\frac{1}{2} + e\right)\left(U_\infty\alpha + \dot{h} + b\left[\frac{1}{2} - e\right]\dot{\alpha}\right) C(k) \end{aligned} \tag{3.3}$$

$C(k)$ is the frequency-dependent Theodorsen function, b the semi-chord length, and e the location of the elastic axis relative to mid-chord. In both equations, the first term accounts for the non-circulatory or apparent mass effects. The second term describes the circulatory effects based on the Theodorsen function (Leishman 2000).

The circulatory terms of the lift and moment are caused by the vorticity in the wake of the airfoil, which affects the circulation about the airfoil. The non-circulatory terms are given by the acceleration of the mass of air through the motion of the airfoil, which causes a reacting force on the airfoil itself (Wright and Cooper 2007; Leishman 2000).

Figure 3.2 depicts the unsteady aerodynamic airloads of an airfoil in pitch motion around the airfoil center. For low reduced frequencies, the quasi-steady lift and moment ($k = 0$) is reduced by the circulatory effects. For higher reduced frequencies, lift and moment increase as the apparent mass forces dominate the unsteady aerodynamic forces (Leishman 2000). The apparent mass effects are most important for control surface flutter at high reduced frequencies (Wright and Cooper 2007).

Theodorsen aerodynamics gives a description for inviscid, incompressible flow. Compressibility and viscosity are highly important in transonic flows. Therefore, the assumptions of the Theodorsen aerodynamics are of little value. For viscous, compressible flows, the transfer function between the motion of the airfoil and the unsteady aerodynamic loads can be obtained by CFD methods. Forced motion computations are performed for a single reduced frequency or a linear system identification is used to obtain the transfer function.

In linear system identification, the steady state is disturbed by a perturbation of small amplitude to obtain the transfer function of the system. For a linear, time-invariant system, the transfer or frequency response function $G(i\omega)$ is given by the system response $Q(i\omega)$ and

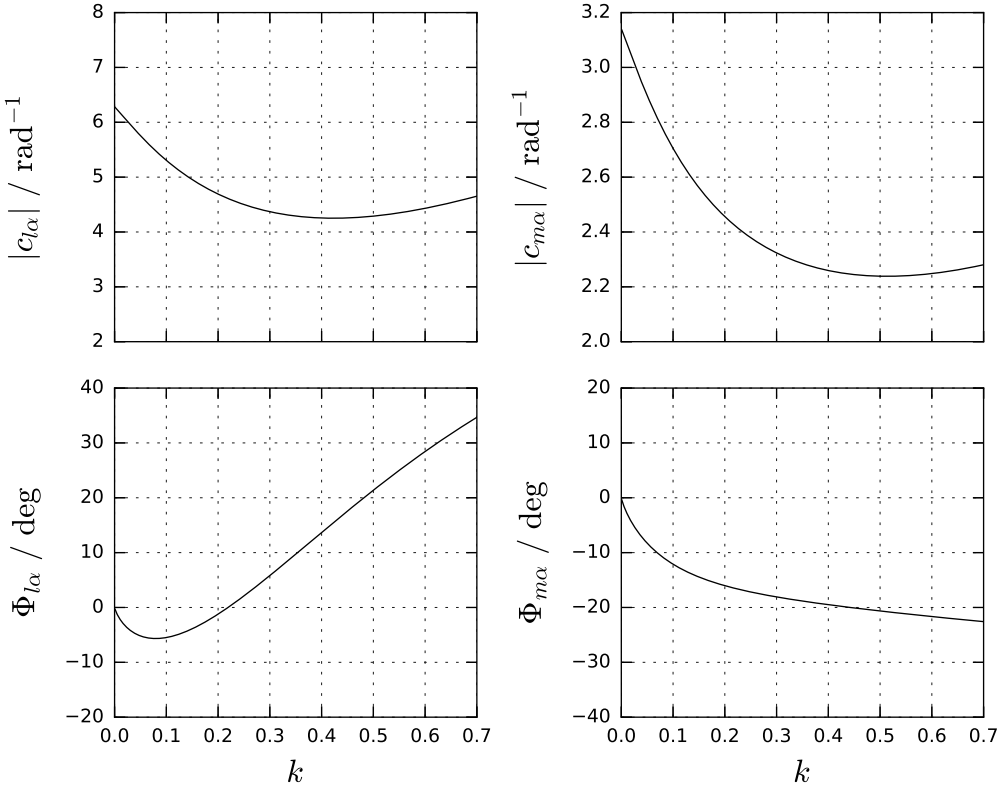

Figure 3.2: Theodorsen aerodynamics for an airfoil pitching around mid-chord

the excitation $X(i\omega)$ (Kaiser et al. 2015):

$$G(i\omega) = \frac{Q(i\omega)}{X(i\omega)} \tag{3.4}$$

$Q(i\omega)$ is given by the Fourier-transformed lift and moment for the smooth step function $X(i\omega)$. The step function is designed to give a broadband excitation of the system (Kaiser et al. 2015).

The flow field around an airfoil in a transonic flow is in general dominated by nonlinear effects. For this case, linearity is assumed for sufficiently small disturbance amplitudes, for which the system response is amplitude independent.

3.3 Flutter Solution for a Binary System

The influence of transitional flows on the flutter boundary will be investigated for a binary system with a pitch and a heave degree-of-freedom. The 2-dof system is depicted in Figure 3.3. The generalized coordinates are given by $\overrightarrow{x} = \{h,\ \alpha\}^T$. The equation of motion is given by:

$$\begin{bmatrix} m & S_\alpha \\ S_\alpha & I_\alpha \end{bmatrix} \overrightarrow{\ddot{x}} + \begin{bmatrix} K_h & 0 \\ 0 & K_\alpha \end{bmatrix} \overrightarrow{x} = Q_i \tag{3.5}$$

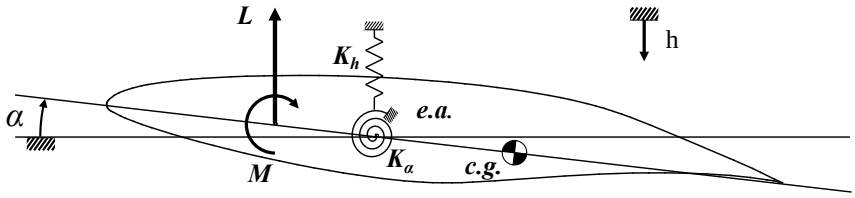

Figure 3.3: 2-dof system for flutter calculations

The external forces Q_i acting on the airfoil are given by the aerodynamic lift L and moment M_y. If the elastic axis is the moment reference axis, they are easily expressed by the derivatives of the aerodynamic coefficients:

$$Q_i = \left\{ \begin{array}{c} -L \\ M_{y,\,e.a.} \end{array} \right\} = \begin{bmatrix} -q_\infty S\, c_{lh} & -q_\infty S\, c_{l\alpha} \\ q_\infty S\, c\, c_{mh} & q_\infty S\, c\, c_{m\alpha} \end{bmatrix} \overrightarrow{x} = q_\infty S\ [\mathbf{A}]\, \overrightarrow{x} \tag{3.6}$$

It is assumed that for harmonic motion in both degrees-of-freedom the lift and moment response is linear and harmonic (Försching and Tichy 2014). The p-k method is used to compute the frequency and damping of the system for the Ansatz (Hassig 1971):

$$\overrightarrow{x} = \{\hat{h},\ \hat{\alpha}\}^T \exp\left(U_\infty\, p\, t/b\right) \tag{3.7}$$

which gives:

$$\frac{U_\infty^2}{b^2}\,[\mathbf{M}]\, p^2 + [\mathbf{K}] - q_\infty S\ [\mathbf{A}] = 0 \tag{3.8}$$

The eigenvalues p are determined from equation 3.8. They describe the reduced damping $\delta = \sigma\, b/U_\infty$ and reduced frequency $k = \omega\, b/U_\infty$ of the system:

$$p_1 = \delta_1 + i\, k_1, \qquad p_2 = \delta_2 + i\, k_2 \tag{3.9}$$

The aerodynamic matrix $[\mathbf{A}]$ depends on the reduced frequency k. The frequency of $[\mathbf{A}(k)]$

has to meet the frequency of the computed eigenvalue p. Therefore, the eigenvalues have to be determined by iteration.

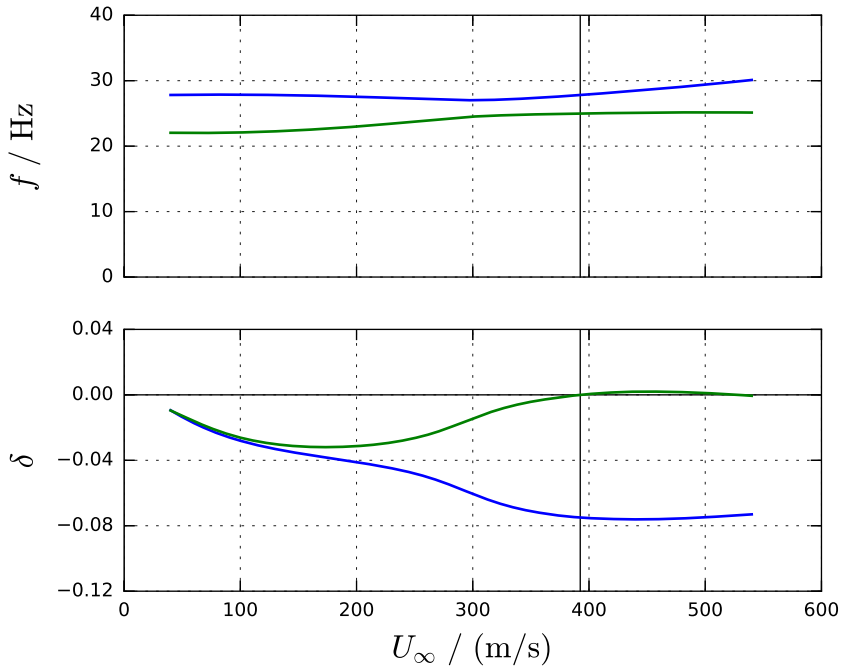

Figure 3.4: Frequency and damping of a 2-dof system

Once the matrix $[\mathbf{A}(k)]$ is known for a specific Mach and Reynolds number, the frequency f and reduced damping δ of the aeroelastic system is computed for increasing freestream velocities. From the resulting δ-U_∞ diagram, the flutter speed is found at the zero-damping crossing. An example of a flutter diagram is depicted in Fig. 3.4. The 2-dof system shows classical bending-torsion flutter. The modes start to interact and the 1^{st} mode gets unstable as the velocity increases.

Classical bending-torsion flutter requires a mode interaction as it is shown in Fig. 3.4. Therefore, the ratio of the structural natural frequencies (wind-off frequencies) has a strong influence on the flutter behavior. For a binary system, the flutter speed is increased by an increase of the frequency ratio (Wright and Cooper 2007).

The system given by equation 3.8 is coupled in terms of structural and aerodynamic parameters. The static moment S_α gives a non-diagonal structural matrix $[\mathbf{M}]$. The lift coefficient derivative due to pitch $c_{l\alpha}$ and the moment coefficient derivative due to heave c_{mh} result in a non-diagonal aerodynamic matrix $[\mathbf{A}]$. The structural coupling is lost for a center of gravity located on the elastic axis. The aerodynamic de-coupling requires a vanishing of the unsteady lift and moment coefficient derivatives, which is generally not given for airfoils.

4 Transition Model

4.1 γ-Re$_\theta$ Transition Model

4.1.1 Local Correlation-Based Transition Model

The γ-Re$_\theta$ transition model is a local correlation-based transition model. The transition model utilizes two transport equations to model boundary layer transition based on empirical correlations. The model is considered local as only information given at a single grid point is used. There is no need to determine any integral boundary layer quantities, which are usually employed in empirical correlations. The transition criterion for the transition onset Reynolds number in the γ-Re_θ model is given by the freestream turbulence Tu and the pressure gradient parameter λ_θ:

$$Re_{\theta t} = f(Tu, \lambda_\theta) \tag{4.1}$$

Both correlation parameters are not well defined inside the boundary layer and a transport equation is used to provide the information on the transition onset momentum loss Reynolds number $Re_{\theta t}$ inside the boundary layer. Instead of computing the actual momentum loss Reynolds number Re_θ to evaluate the transition criterion, an approximation is used, which is derived from boundary layer equations.

A second transport equation for the intermittency variable γ is used to scale the turbulence production of the underlying turbulence model (see Fig. 4.1). Once the transition onset is given, the intermittency increases from its floor value $\gamma = 0.02$ to 1. The intermittency is used to scale the turbulence production of the turbulence model. Outside the boundary layer, which is approximated by blending functions, the intermittency is $\gamma = 1$ to maintain the characteristics of the underlying turbulence model. The blending based on γ gives a smooth transition from a laminar to a turbulent boundary layer flow.

The γ-Re$_\theta$ transition model is based on a one-equation transition model introduced by Menter et al. (2002). This predecessor model is built on a transport equation for an intermittency variable γ to model the transition process (Menter et al. 2002). The first publication of

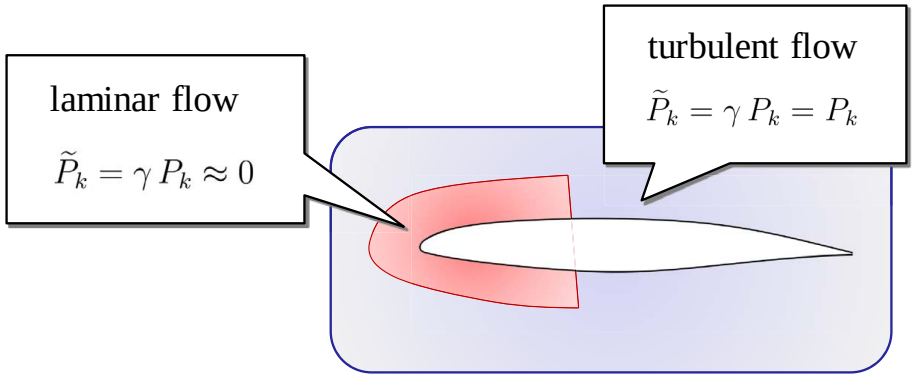

Figure 4.1: Intermittency γ and turbulence production term P_k

the γ-Re$_\theta$ transition model (Menter et al. 2006; Langtry et al. 2006) did not include two major correlations due to proprietary reasons. Until the model was fully disclosed (Langtry and Menter 2009), other authors used the model framework to calibrate the missing correlations (e.g. Misaka and Obayashi 2006; Krause et al. 2008; Pettersson and Crippa 2008; Malan et al. 2009). In addition, the model is further developed to account for crossflow transition by Grabe et al. (2016).

The γ-Re$_\theta$ transition model is available in the DLR TAU-Code (Seyfert and Krumbein 2010). In addition, the TAU-Code provides a transition module, which includes an e^N method approach based on the linear stability theory. The e^N method is the standard transition prediction method in the aircraft industry (Krumbein et al. 2009a, b). The DLR TAU-Code is a finite-volume CFD solver for viscous and inviscid flows. It uses an edge-based dual-cell approach and provides different eddy viscosity turbulence models to solve the Reynolds-averaged Navier-Stokes (RANS) equations (Schwamborn et al. 2006).

4.1.2 Transition Model Description

As the correlation for the transition onset Reynolds number $Re_{\theta t}$ is not well defined inside the boundary layer, $Re_{\theta t}$ is only computed in the freestream. A transport quantity $\widetilde{Re}_{\theta t}$ is used to transport the information on $Re_{\theta t}$ into the boundary layer. The transport equation for $\widetilde{Re}_{\theta t}$ is given by (Langtry and Menter 2009):

$$\frac{\partial \rho \widetilde{Re}_{\theta t}}{\partial t} + \frac{\partial \rho\, u_j \widetilde{Re}_{\theta t}}{\partial x_j} = P_{\theta t} + \frac{\partial}{\partial x_j}\left[\sigma_{\theta t}\,(\mu + \mu_t)\,\frac{\partial \widetilde{Re}_{\theta t}}{\partial x_j}\right] \tag{4.2}$$

with the production term $P_{\theta t}$:

$$P_{\theta t} = c_{\theta t} \frac{\rho}{t_\theta} \left(Re_{\theta t} - \widetilde{Re}_{\theta t} \right) (1 - F_{\theta t}) \tag{4.3}$$

The production term is a proportional control for $\widetilde{Re}_{\theta t}$ with the target value $Re_{\theta t}$. The term $F_{\theta t}$ disables the production inside the laminar boundary layer. The basic concept of the $\widetilde{Re}_{\theta t}$ transport is depicted in Fig. 4.2. $\widetilde{Re}_{\theta t}$ diffuses into the boundary layer and is convected downstream. Once the quantity of $\widetilde{Re}_{\theta t}$ is given at every grid point inside the boundary layer, the transition criterion can be evaluated.

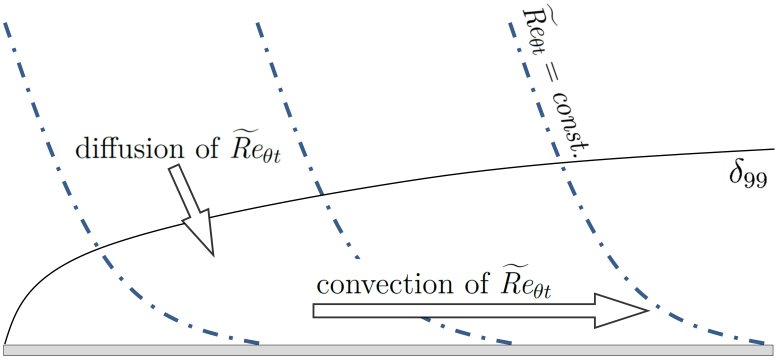

Figure 4.2: Diffusion and convection of $\widetilde{Re}_{\theta t}$

The evaluation is included in the γ transport equation. The intermittency γ is used to scale the production and destruction of the turbulent kinetic energy of the underlying turbulence model. Although the intermittency variable resembles the idea of Emmons (1951), it should not be interpreted in the same way as it does not model the physical intermittency. The γ transport equation is given by (Langtry and Menter 2009):

$$\frac{\partial \rho \gamma}{\partial t} + \frac{\partial \rho u_j \gamma}{\partial x_j} = P_\gamma - E_\gamma + \frac{\partial}{\partial x_j} \left[\left(\mu + \frac{\mu_t}{\sigma_f} \right) \frac{\partial \gamma}{\partial x_j} \right] \tag{4.4}$$

with the production term P_γ:

$$P_\gamma = F_{length}\, c_{a1}\, \rho\, S \sqrt{\gamma F_{onset}}\, (1 - c_{e1}\gamma) \tag{4.5}$$

and the destruction term E_γ:

$$E_\gamma = c_{a2}\, \rho\, \Omega\, \gamma F_{turb}\, (c_{e2}\gamma - 1) \tag{4.6}$$

The intermittency production is scaled by $F_{length} = f\left(\widetilde{Re}_{\theta t}\right)$. The term F_{onset} triggers the transition onset, once the transition criterion is met. F_{turb} in the destruction term is used to turn off the intermittency destruction outside of the laminar boundary layer.

The transition onset Reynolds number $\widetilde{Re}_{\theta t}$ has to be compared to the local Reynolds number Re_θ at each station along the boundary layer. As the computation of a non-local quantity is not desired, Re_θ is not computed directly. Instead, the vorticity Reynolds number Re_ν is computed:

$$Re_\nu = \frac{\rho l^2 \left({}^{du}/_{dy}\right)^2}{\mu \, {}^{du}/_{dy}} = \frac{\hat{y}^2}{\nu} \frac{\mathrm{d}u}{dy} \tag{4.7}$$

where $\hat{y}$ is the distance to the nearest wall.

The maximum vorticity Reynolds number is proportional to the momentum loss Reynolds number Re_θ (Menter et al. 2006). Therefore, the local value of the momentum loss Reynolds number can be determined by computing the maximum vorticity Reynolds number with an appropriate scaling:

$$Re_\theta = \frac{Re_{\nu,\,max}}{\zeta} \tag{4.8}$$

Van Driest and Blumer (1963) use Re_ν directly as a transition criterion. The same formulation is used by Rouse (1946) as a stability parameter χ. Rouse (1946) argues that a steep velocity gradient is required for any disturbance to grow into a turbulent structure.

For a Falkner-Skan flow and different Hartree parameters[1] β, the local ratio of Re_ν/Re_θ is computed and depicted in Fig. 4.3. At the wall, any disturbance is damped and equation 4.7 is zero. The same applies for the freestream, where du/dy is zero. The vorticity Reynolds number Re_ν has a local maximum in the boundary layer at the point at which the breakdown to turbulence is expected (van Driest and Blumer 1963; Rouse 1946).

Figure 4.4 depicts the ratio $\zeta = Re_{\nu,\,max}/Re_\theta$ for different pressure gradients (i.e. Hartree parameters). The γ-Re_θ transition model predicts transition, once the critical momentum loss Reynolds number $Re_{\theta c} = f\left(\widetilde{Re}_{\theta t}\right)$ is reached:

$$\frac{Re_\theta}{Re_{\theta c}} = \frac{Re_\nu}{\zeta \, Re_{\theta c}} > 1 \tag{4.9}$$

The relation in equation 4.9 is included in F_{onset} in equation 4.5. The transition onset is given at the location of $Re_{\nu,\,max}$ inside the laminar boundary layer, where first breakdown patterns occur in a laminar boundary layer flow (Klebanoff and Tidstrom 1959; Kovasznay et al. 1962). Therefore, no search procedure is required to determine $Re_{\nu,\,max}$.

Langtry and Menter (2009) use a constant value of $\zeta = 2.193$ to scale the vorticity Reynolds number. The value of ζ deviates from the Blasius boundary layer value depending on the Hartree parameter β. As the model includes a calibration for pressure gradient effects, it is not

[1] $\beta = -0.1988$: separation point, $\beta = 0$: Blasius boundary layer, $\beta = 1$: stagnation point

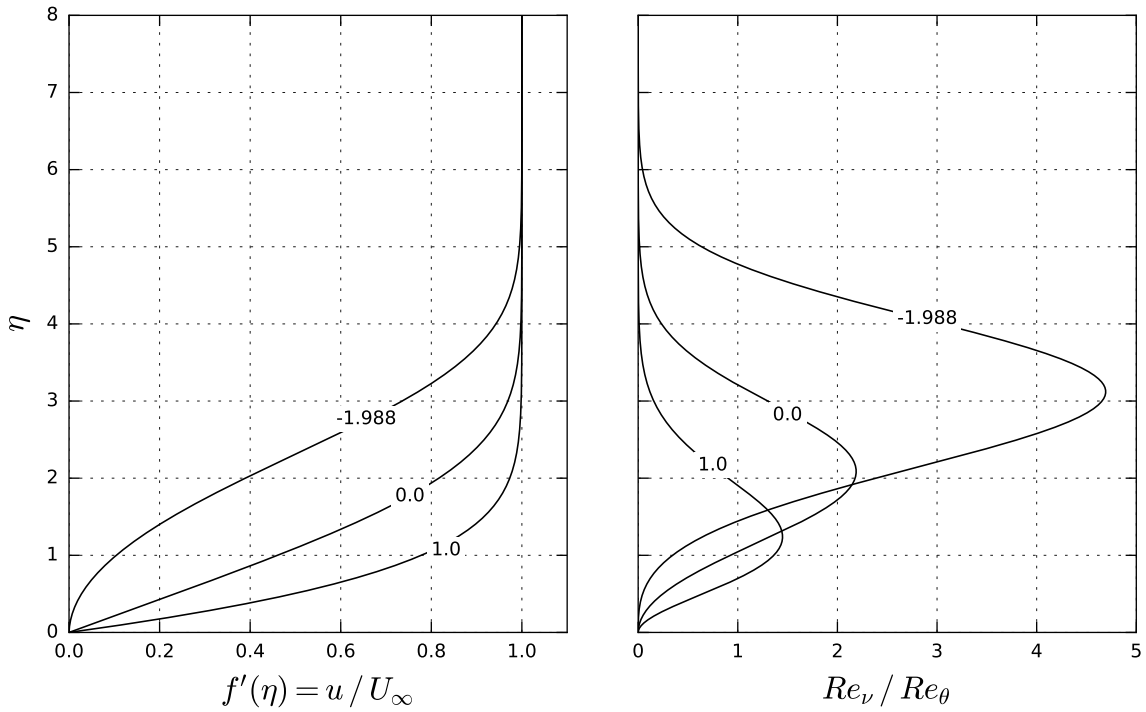

Figure 4.3: Velocity profile and ratio of Re_ν/Re_θ for different Hartree parameters β

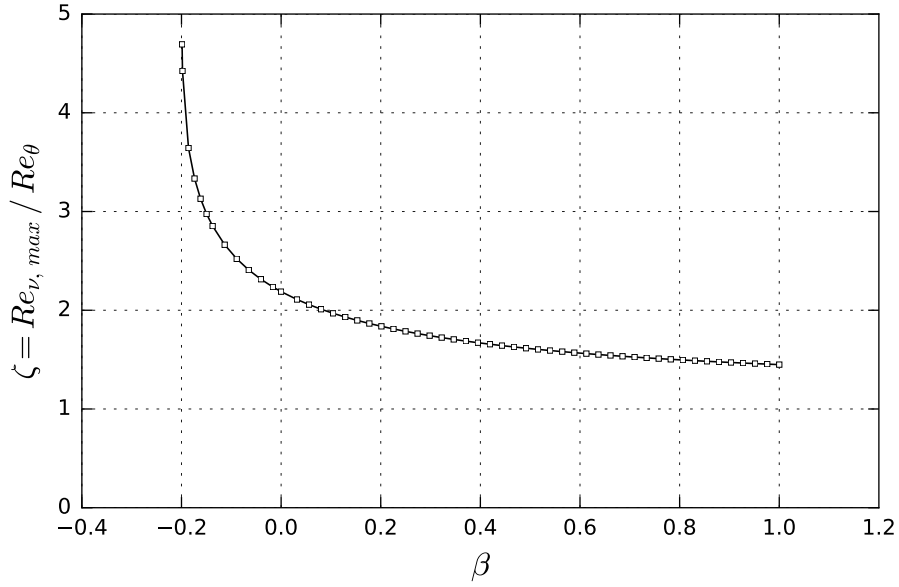

Figure 4.4: Ratio of $Re_{\nu,max}/Re_\theta$ for different Hartree parameters β

required to use the exact value of ζ for different pressure gradients (Menter et al. 2015).

Once the intermittency increases, the turbulent kinetic energy is increased. This is achieved by the coupling to the SST k-ω turbulence model. The production and destruction term of the SST k-ω turbulence model are modified by the effective intermittency[2] (Langtry and Menter 2009):

$$\widetilde{P}_k = \gamma_{eff} P_k \tag{4.10}$$

$$\widetilde{D}_k = \min\left[\max\left(\gamma_{eff},\, 0.1\right),\, 1\right] D_k \tag{4.11}$$

A complete description of the transition model with all model parameters and test cases is given by Langtry (2006) and Langtry and Menter (2009).

4.1.3 Transition Model Deficiencies

Transition Onset Correlation

During research on airfoil flows in a wide range of Mach and Reynolds numbers, certain shortcomings of the γ-Re_θ transition model are observed. The transition position is predicted too far upstream in favorable pressure gradient flows at moderate and high Reynolds numbers, compared to experimental data and results from the e^N method.

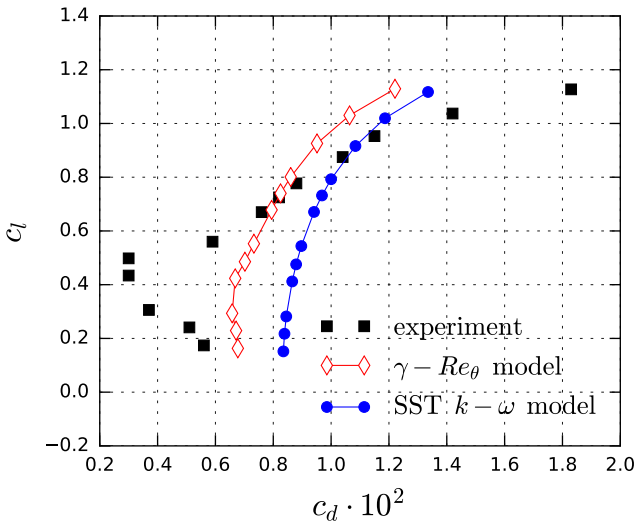

Figure 4.5: Transition model deficiencies: Transition onset correlation

[2]The effective intermittency γ_{eff} is used to allow intermittency values $\gamma > 1$ in the case of a laminar separation.

An example is depicted in Fig. 4.5: Experimental results for a two-dimensional airfoil at $Re = 9.5 \cdot 10^6$ and $M_\infty = 0.4$ (NLF(1)-0414F, Run 15, see Section 4.2.4) are compared to fully turbulent results from the SST $k-\omega$ turbulence model and transitional results from the γ-Re_θ transition model. The experimental results give a drag curve with a laminar drag bucket. The drag bucket has a small extent with a rather sharp upper limit. The drag benefit is huge compared to the fully turbulent results. Although the γ-Re_θ transition model predicts some laminar flow, the drag bucket is not reproduced.

The laminar drag bucket in Fig. 4.5 develops under favorable pressure gradients on the upper and lower surface of the airfoil. The transition location is located at the pressure minimum at a chord position far downstream. The transition onset correlation of the γ-Re_θ transition model is not able to reproduce the stabilizing effect of the accelerated flow.

In Section 2.5, different correlations for the influence of turbulence level and pressure gradient are presented. The pressure gradient correlation of Langtry and Menter (2009) agrees with the correlation given by Abu-Ghannam and Shaw (1980). However, both correlations cross the theoretical stability limit for favorable pressure gradients. This is of no concern for high turbulence levels but questionable for T-S transition at low turbulence levels.

Turbulence Levels in External Flows

The main correlation parameter for the γ-Re_θ transition model is the turbulence level Tu. The turbulence level differs strongly between different applications: The freestream turbulence level encountered during cruise flight ($\tau < 0.05$ %) is lower than in a wind tunnel ($\tau \approx 0.1$ % ... 0.3 %). In gas turbine engines, the turbulence level is even higher: Compressor and turbine stages show turbulence levels of $\tau = 5$ % to 10 % (Mayle 1991).

In addition, the flow around an object changes the turbulence level in the vicinity of the object. A trailing edge wake of a device, different local freestream velocities in rotor applications, and blockage effects in wind tunnels change the local turbulence level. The γ-Re_θ model accounts for these effects as a local turbulence level is computed. However, there is no experimental data available, which show that the local deviation of the ambient turbulence level from the farfield value is represented correctly.

Figure 4.6 depicts the turbulence level in the vicinity of an airfoil. The farfield values for the viscosity ratio R_T and τ are set to obtain a value of $\tau = 0.1$ % at the airfoil. The turbulence level increases as the flow approaches the airfoil. In the low turbulence regime, there is a strong variation of $Re_{\theta t}$ with Tu. The turbulence level evaluated in the transition criterion can deviate strongly from the expected ambient value.

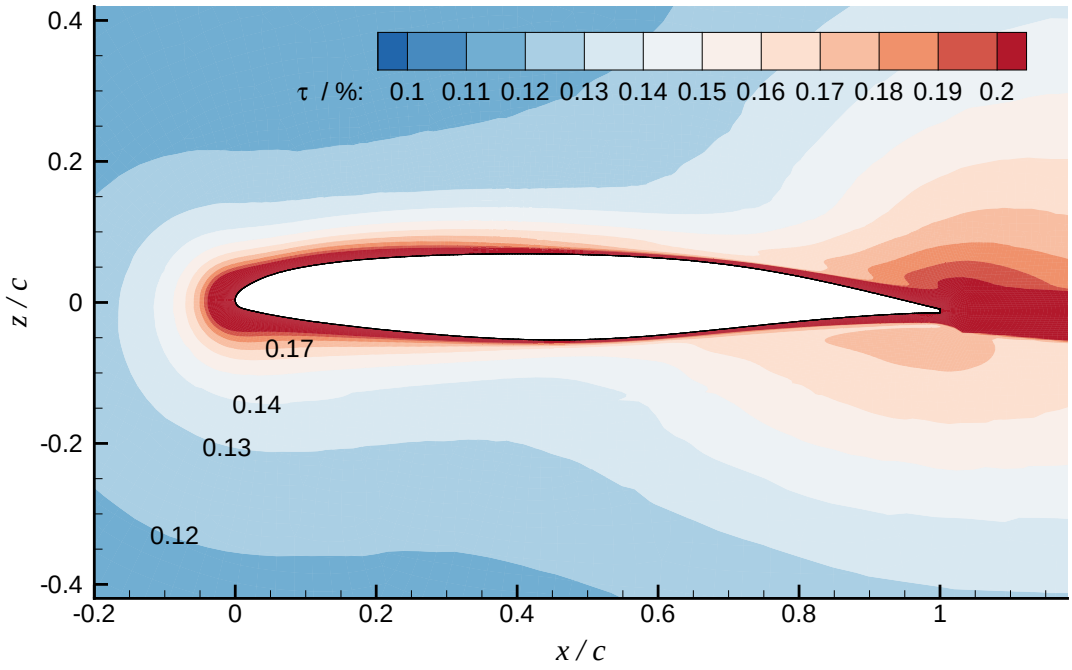

Figure 4.6: Transition model deficiencies: Turbulence level τ

$\widetilde{Re}_{\theta t}$ Transport Equation

Figure 4.7 depicts the $\widetilde{Re}_{\theta t}$ and the intermittency distribution in a transonic flow on the suction side of an airfoil close to the leading edge. The flow is accelerated, $\widetilde{Re}_{\theta t}$ increases strongly, and the information on the transition onset Reynolds number is transported into the boundary layer. At some point downstream, the transition criterion is given and the intermittency increases.

From experimental data, it is known that the transition onset is influenced by the history of the boundary layer flow and not the local value of the pressure gradient and turbulence level (Abu-Ghannam and Shaw 1980). This supports the idea of a transport equation for $\widetilde{Re}_{\theta t}$. Abu-Ghannam and Shaw (1980) investigate the history effect of adverse and favorable pressure gradients in a flat plate experiment. A qualitative description is given on how the flow history affects the transition behavior, but no correlation is proposed. The effect described by Abu-Ghannam and Shaw (1980) is therefore hardly quantifiable.

The $\widetilde{Re}_{\theta t}$ transport equation is calibrated with flat plate experiments (Langtry 2006). The low speed experiments show transition at low Reynolds numbers ($Re_x < 0.5 \cdot 10^6$) in a low turbulence environment. There is no information given, how history effects change with Mach and Reynolds number. In addition, Abu-Ghannam and Shaw (1980) point out that flow history has no effect on transition in flows with continuously increasing $|\lambda_\theta|$, which is not considered in the γ-Re_θ transition model.

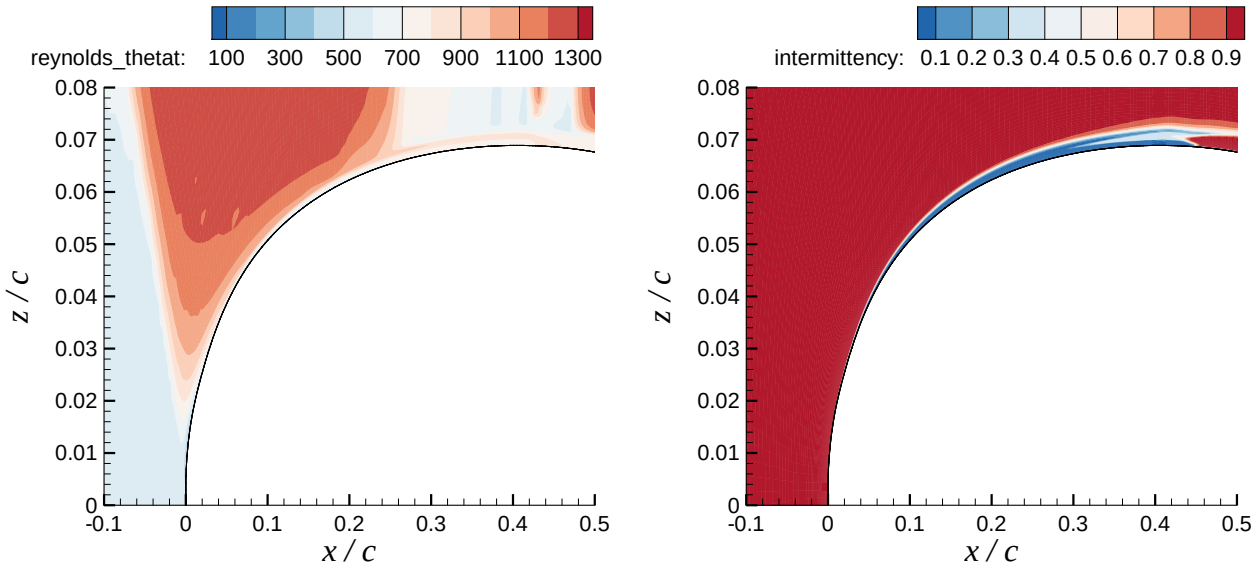

Figure 4.7: Transition model deficiencies: $\widetilde{Re}_{\theta t}$ transport

The ratio of convection (history effects) to diffusion (local effects) is controlled by the parameter $\sigma_{\theta t}$. A higher value reduces the history effects as the diffusion of $\widetilde{Re}_{\theta t}$ into the boundary layer increases (Langtry 2006). Content and Houdeville (2010) use a value of $\sigma_{\theta t} = 10$ compared to $\sigma_{\theta t} = 2$ in the original model (Langtry 2006), which requires a recalibration of the intermittency transport equation. The recalibrated model by Content and Houdeville (2010) gives equivalent transition locations for the flat plate test cases presented by Langtry (2006). Because no physical effect of the receptivity process is included in the model, there is no way to determine any physical correct ratio of diffusion to convection for different flow conditions.

In addition, the choice of turbulence limiters has a strong effect on the $\widetilde{Re}_{\theta t}$ transport. As shown by Langel et al. (2016), this influence increases with Reynolds number. The $\widetilde{Re}_{\theta t}$ transport equation increases the calibration expenditure, but the upstream flow history effect on transition can as well be modelled based on the intermittency equation.

4.2 γ Transition Model

4.2.1 Transition Model Description

The transition model is transformed into a one-equation model by calculating the transition onset Reynolds number $Re_{\theta t}$ directly inside the boundary layer. The transition model is reduced to the transport equation for the intermittency variable γ to exclude any effect of the $\widetilde{Re}_{\theta t}$ transport equation. The transport equation for $\widetilde{Re}_{\theta t}$ is replaced by an algebraic computation. The model is named γ transition model. It is similar to the predecessor model of the γ-Re$_\theta$ transition model proposed by Menter et al. (2002). The intermittency transport equation is given by:

$$\frac{\partial \rho \gamma}{\partial t} + \frac{\partial \rho\, u_j \gamma}{\partial x_j} = P_\gamma - E_\gamma + \frac{\partial}{\partial x_j}\left[(\mu + \mu_t)\,\frac{\partial \gamma}{\partial x_j}\right] \tag{4.12}$$

The production term P_γ and the destruction term E_γ are modified compared to the γ-Re_θ transition model. The new production term reads:

$$P_\gamma = F_{length}\,\rho\, S\, F_{onset}\,(1-\gamma) \tag{4.13}$$

$$\text{with } F_{length} = 14$$

In the γ-Re_θ transition model, the transition zone length is scaled by $F_{length} = f\left(\widetilde{Re}_{\theta t}\right)$. For the calibration test cases considered, a constant value of F_{length} is sufficient to give reliable results. The term F_{onset} activates the intermittency production once the transition onset Reynolds number is reached:

$$F_{onset} = max\,(F_{onset2} - F_{onset3},\, 0) \tag{4.14}$$

$$F_{onset2} = min\,(F_{onset1},\, 2) \tag{4.15}$$

$$F_{onset3} = max\left(1 - \left(\frac{R_T}{2}\right)^3,\, 0\right) \tag{4.16}$$

$$F_{onset1} = \frac{Re_\nu}{\xi\, Re_{\theta t}} \tag{4.17}$$

The denominator in equation 4.16 is changed to 2 compared to 2.5 in the γ-Re_θ transition model, the term F_{onset2} is simplified, and $Re_{\theta t}$ is used directly instead of $Re_{\theta c}$. The viscosity

ratio R_T is defined as[3]:

$$R_T = \frac{\mu_t}{\mu} = \frac{\rho\, k}{\omega\, \mu} \tag{4.18}$$

The transition criterion is given in equation 4.17. The momentum loss thickness Reynolds number at the transition onset $Re_{\theta t}$ is compared to the scaled vorticity Reynolds number Re_ν/ξ. The scaling parameter $\xi = f(M_e)$ contains a compressibility correction based on the local, isentropic Mach number M_e, which is obtained from the inflow Mach number M_∞, inflow pressure p_∞, and the local static pressure p. The static pressure is approximately constant across the boundary layer at each station along the body. It is identified as a boundary layer edge value $p = p_e$. The boundary layer edge pressure p_e gives the isentropic boundary layer edge Mach number M_e (Anderson 2007):

$$M_e = \sqrt{\left[\frac{1 + \frac{\kappa-1}{2} M_\infty^2}{(p_e/p_\infty)^{\frac{\kappa-1}{\kappa}}} - 1\right] \frac{2}{\kappa - 1}} \tag{4.19}$$

In the γ-Re_θ transition model, $Re_\nu = (\rho\, \hat{y}^2 S)\,/\mu$ is computed based on the density ρ and dynamic viscosity μ inside the boundary layer. In the γ transition model, the vorticity Reynolds number is computed based on the boundary layer edge values ρ_e and μ_e for the following reason: The value of ζ in equation 4.9 is given by a similarity solution of the Falkner-Skan equation[4]. The Falkner-Skan equation is solved in terms of the non-dimensional wall distance η and the non-dimensional velocity $f'(\eta)$ for different Hartree parameters β (Schlichting and Gersten 2006):

$$f''' = -\left[f f'' + \beta\,(1 - f f')\right] \tag{4.20}$$

From the solution of equation 4.20, ζ is found:

$$\zeta = \frac{Re_{\nu,\,max}}{Re_\theta} = \frac{max\,(\eta^2 f'')}{\int_0^{\eta\infty} f'\,(1 - f')\,d\eta} \tag{4.21}$$

Re_θ is only defined in terms of boundary layer edge quantities. Re_ν has to be computed accordingly as no variation of the density and viscosity across the boundary layer is included in equation 4.21:

$$Re_\nu = \frac{\rho_e\, \hat{y}^2 S}{\mu_e} \tag{4.22}$$

[3]Inside the boundary layer, μ_t is computed based on the absolute value of the vorticity (Menter 1994).

[4]In the case of the γ transition model, the value of ξ in equation 4.17 is obtained for a similarity solution of a compressible, zero pressure gradient flow and the same argument applies.

From the isentropic relations and the Sutherland equation, ρ_e and $\mu_e = f(T_e)$ are derived (Anderson 2007):

$$\frac{p_e}{p_\infty} = \left(\frac{\rho_e}{\rho_\infty}\right)^{\kappa} = \left(\frac{T_e}{T_\infty}\right)^{\frac{\kappa}{\kappa-1}} \tag{4.23}$$

$$\frac{\mu_e}{\mu_0} = \left(\frac{T_e}{T_0}\right)^{\frac{3}{2}} \frac{T_0 + 110\,\mathrm{K}}{T_e + 110\,\mathrm{K}} \tag{4.24}$$

with $\mu_0 = 1.7894 \cdot 10^{-5}\,\mathrm{kg/(m\ s)}$ and $T_0 = 288.16\,\mathrm{K}$ (Anderson 2007)[5].

The destruction term E_γ in equation 4.12 is given by:

$$E_\gamma = c_{a2}\,\rho\,\Omega\,\gamma\,F_{turb}\,(c_{e2}\,\gamma - 1) \tag{4.25}$$

$$\text{with } c_{a2} = 0.06,\ c_{e2} = 50$$

F_{turb} equals 0 outside the laminar boundary layer to disable the intermittency destruction. In the case of shocks and in the vicinity of a turbulent wake, an intermittency decrease can occur for the γ-Re$_\theta$ transition model outside of the laminar boundary layer. Therefore, the original term of the γ-Re$_\theta$ transition model given by $F_{turb\,1}$ is extended to:

$$F_{turb\,1} = \exp\left[-\left(\frac{R_T}{4}\right)^4\right] \tag{4.26}$$

$$F_{turb} = F_{turb\,1}\,F_{\theta t} \tag{4.27}$$

$F_{\theta t}$ is taken from Langtry (2006). It is computed based on $Re_{\theta t}$ instead of $\widetilde{Re}_{\theta t}$.

Figure 4.8 depicts $F_{onset\,3}$ and $F_{turb\,1}$ for an increasing viscosity ratio R_T. Three different states can be identified:

- State I: The boundary layer flow is laminar with $R_T \ll 1$ inside the boundary layer. The intermittency starts to increase, once the transition criterion is given by $F_{onset\,1} > 1$.

- State II: As R_T increases inside the boundary layer, $F_{onset\,3}$ decreases, which enables an increased intermittency production. Once R_T increased far enough, intermittency is produced even without $F_{onset\,1} > 1$.

[5] In the DLR TAU-Code, the reference values for the Sutherland equation are given by $\mu_0 = 1.716{\cdot}10^{-5}\,\mathrm{kg/(m\ s)}$ and $T_0 = 273\,\mathrm{K}$.

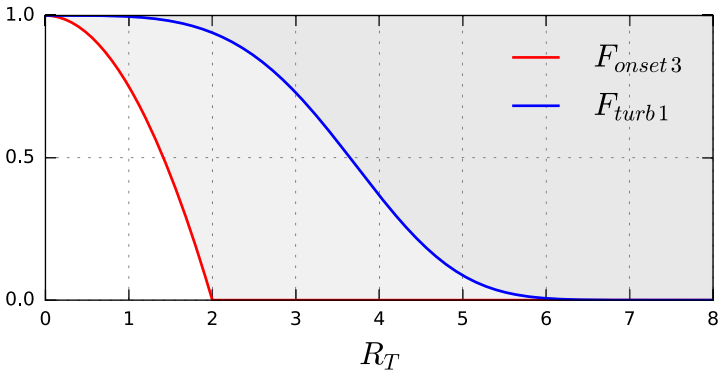

Figure 4.8: F_{onset3} and F_{turb1} for an increasing viscosity ratio R_T

- State III: The intermittency destruction E_γ decreases with F_{turb1}. The boundary layer is fully turbulent once $F_{turb1} = 0$.

A valid transition prediction starts in a boundary layer state I with $R_T \ll 1$. The γ transition model is calibrated for an ambient value $R_T = 1$ in the freestream. The desired viscosity ratio and turbulence level are obtained by additional source terms in the turbulence model equations (Spalart and Rumsey 2007).

There is no special treatment of laminar separations in the model as it is given by Langtry and Menter (2009). The coupling to the SST k-ω turbulence model is not changed from Langtry and Menter (2009).

4.2.2 Transition Criterion

The γ transition model is based on an empirical correlation that includes the effect of turbulence level and pressure gradients. The disturbance environment is described by the farfield turbulence level τ_∞ and the acceleration parameter K. The definition of the turbulence level by τ_∞ is in agreement with the choice of a single critical N_{TS} factor. Based on both correlation parameters, the momentum loss Reynolds number at transition onset $Re_{\theta t}$ is determined:

$$Re_{\theta t} = f(\tau_\infty, K) = 120 + 380\, k_t\, \tau_\infty^{-\frac{2}{5}} \tag{4.28}$$

The effect of the pressure gradient is given by k_t:

$$k_t = \exp\left\{[3.2 - 3.2\, min\,(\sqrt{\tau_\infty}, 1)]\, K_t\right\} \tag{4.29}$$

K_t is based on the acceleration parameter K described in Section 2.5.3, which is also used in the first version of the γ-Re_θ transition model (Menter et al. 2006). It is discarded in the later

version of the model (Langtry and Menter 2009). As Schreiber et al. (2002) point out, K is inversely proportional to the unit Reynolds number. Therefore, K is scaled by the Reynolds number to obtain a general non-dimensional pressure gradient parameter K_t:

$$K_t = K \cdot Re = \frac{\nu_e}{U_e^2} \frac{dU_e}{ds} \cdot Re \tag{4.30}$$

The correlation for the transition onset Reynolds number $Re_{\theta t}$ is depicted in Fig. 4.9. On the left, the influence of the turbulence level is depicted. On the right, the combined influence of pressure gradient and turbulence level is given.

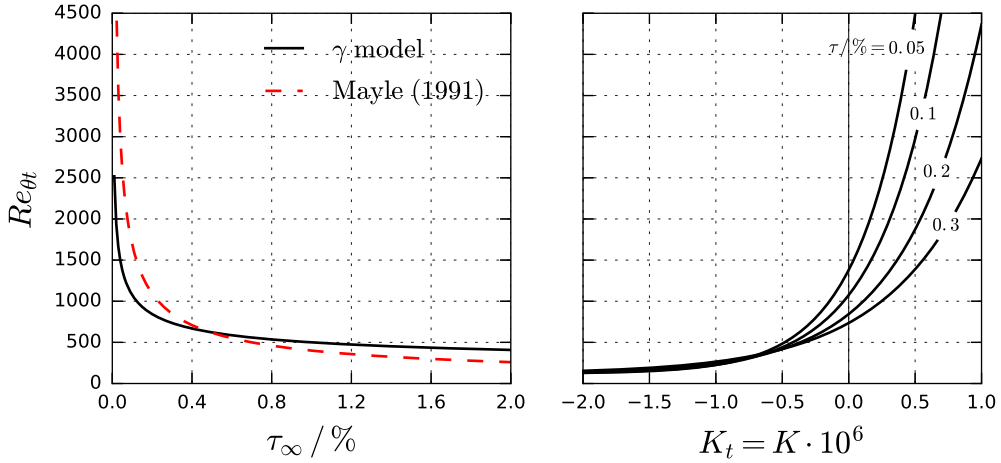

Figure 4.9: Effect of turbulence level and pressure gradient on $Re_{\theta t}$ for $Re = 10^6$

K is computed based on the isentropic boundary layer edge values as described above. The Reynolds number dependence is depicted on the left in Fig. 4.10. For different chord Reynolds numbers $Re_c = 2 \cdot 10^6$, $20 \cdot 10^6$, and $60 \cdot 10^6$, the c_p distribution is computed for a NACA $65_{215} - 114$ airfoil in a fully turbulent flow. Once the Reynolds number dependence of K is considered, the curves for K_t collapse to a single curve for identical pressure coefficient distributions. The effect of K_t and Re_c on the transition onset is depicted on the right in Fig. 4.10: As the Reynolds number increases for a constant disturbance environment, the transition location moves upstream.

The velocity gradient dU_e/ds in equation 4.30 is replaced by the pressure gradient, noting that (Schlichting and Gersten 2006):

$$U_e \frac{dU_e}{ds} = -\frac{1}{\rho_e} \frac{dp}{ds} \tag{4.31}$$

The pressure gradient along the streamline is given by projecting the pressure gradient vector

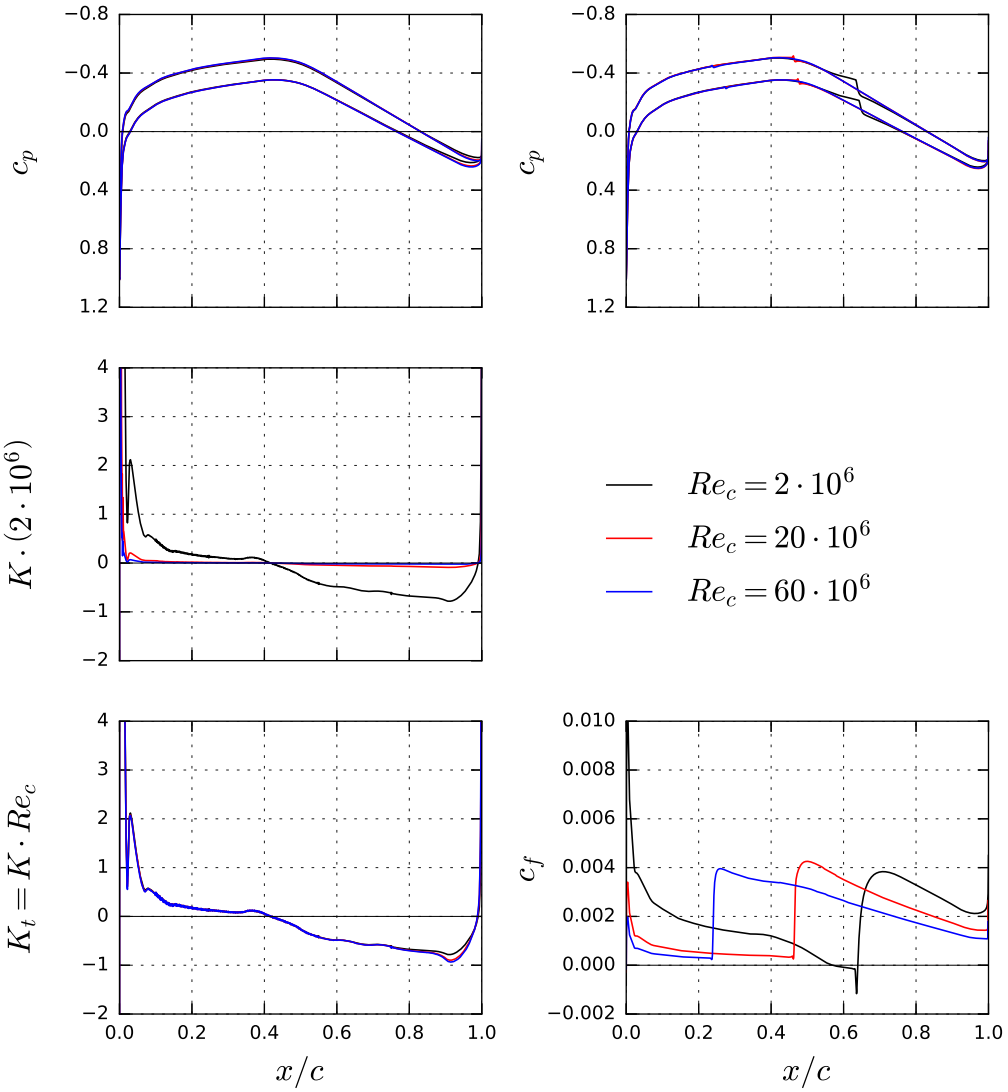

Figure 4.10: Reynolds number dependence of K and influence on the transition location

onto the normalized velocity vector:

$$\frac{dp}{ds} = \overrightarrow{u}/|\overrightarrow{u}| \cdot \nabla p = \frac{u}{|\overrightarrow{u}|}\frac{dp}{dx} + \frac{v}{|\overrightarrow{u}|}\frac{dp}{dy} + \frac{w}{|\overrightarrow{u}|}\frac{dp}{dz} \tag{4.32}$$

4.2.3 Compressibility Correction

The ratio $\xi = Re_{\nu,\,max}/Re_\theta$ changes with the Mach number as the boundary layer velocity profiles are influenced by compressibility. To account for the influence of compressibility on Re_ν, a compressibility correction for ξ is computed. A two-dimensional compressible flow over a flat plate with zero pressure gradient is considered. The boundary layer equations are solved numerically to obtain the parameter ξ as a function of the freestream Mach number:

$$\xi = \frac{Re_{\nu,\,max}}{Re_\theta} = f(M_\infty) \tag{4.33}$$

The method described by Mack (1965) and Criminale et al. (2003) is used. The non-dimensional momentum and energy equation for the similarity variable η read (Criminale et al. 2003):

$$\frac{\mathrm{d}}{\mathrm{d}\eta}\left(\mu\frac{\mathrm{d}U}{\mathrm{d}\eta}\right) + g\frac{\mathrm{d}U}{\mathrm{d}\eta} = 0 \tag{4.34}$$

$$\frac{\mathrm{d}}{\mathrm{d}\eta}\left(\frac{\mu}{Pr}\frac{\mathrm{d}\theta}{\mathrm{d}\eta}\right) + g\frac{\mathrm{d}\theta}{\mathrm{d}\eta} = -2\mu\left(\frac{\mathrm{d}U}{\mathrm{d}\eta}\right)^2 \tag{4.35}$$

$$g' = \frac{U}{2\,T} \tag{4.36}$$

for the local non-dimensional velocity U, the scaled temperature θ, the non-dimensional viscosity μ, the non-dimensional temperature T, and Prandtl number Pr.

The solution procedure is taken from Mack (1965): Equation 4.34 and 4.35 are rewritten as a system of four first-order equations and a fourth-order Runge-Kutta scheme is used for the numerical integration. The computations are performed for a constant Prandtl number $Pr = 0.72$ and a constant specific heat ratio $\kappa = 1.4$ (Criminale et al. 2003).

Figure 4.11 presents the effect of a Mach number increase on the boundary layer in terms of the non-dimensional variables. Figure 4.12 depicts $\xi = f(M)$ for the numerically computed boundary layer flow and the polynomial approximation for $M = [0,\, 4]$:

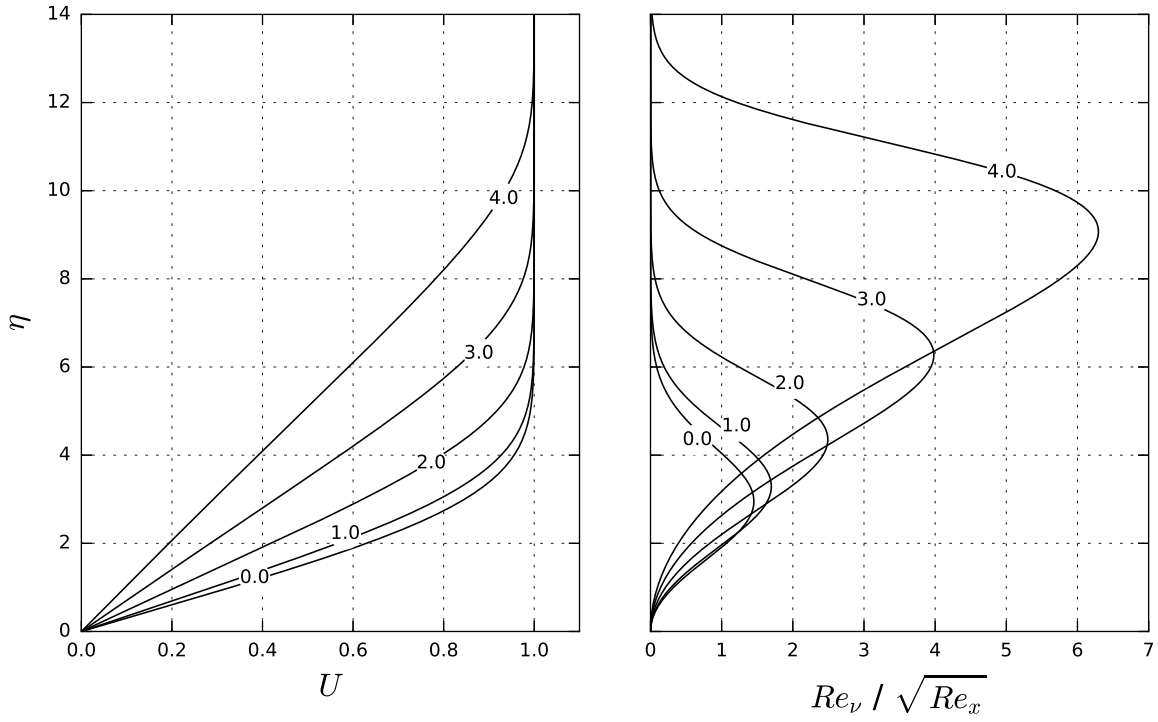

Figure 4.11: Effect of increasing Mach number on the velocity profile and Re_ν. The line numbers indicate the Mach number.

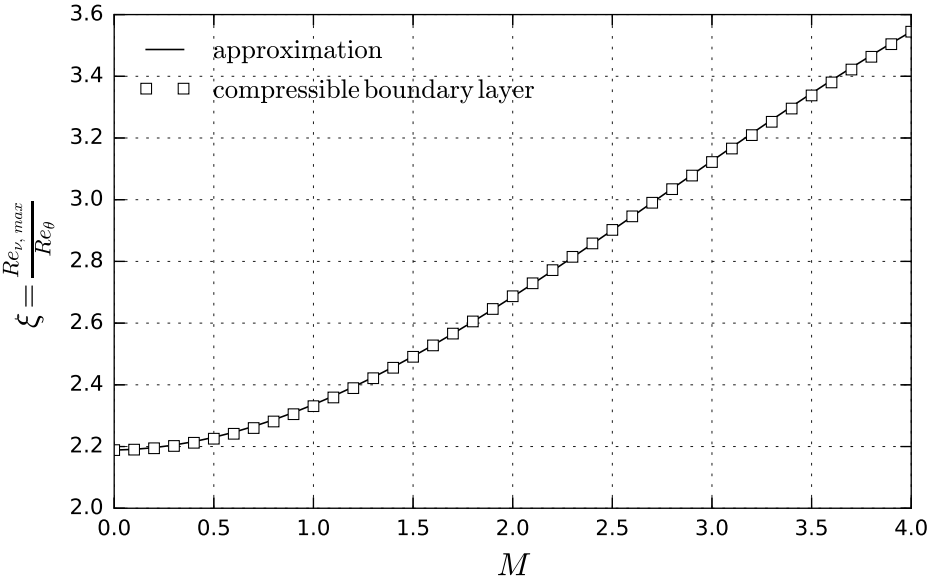

Figure 4.12: ξ as a function of freestream Mach number

$$\xi = a_3\, M^3 + a_2\, M^2 + a_1\, M + a_0 \tag{4.37}$$
$$\text{with } a_3 = -0.0186,\ a_2 = 0.1569,\ a_1 = 0.0091,\ a_0 = 2.18844$$

Higher Mach numbers are not included as the main focus is on transonic, external applications. The correction for ξ given by equation 4.37 is computed using the local isentropic Mach number in the γ transition model.

The variation of $\xi = f(M)$ is less than the variation of $\zeta = f(\beta)$ described in Section 4.1.2. However, no correction for ζ is included. As stated by Menter et al. (2015), the variation of ζ is already given by an appropriate correlation for pressure gradient effects. Once enough experimental data for the effect of compressibility is available, the correction of ξ can be replaced by a compressibility correlation.

4.2.4 Transition Model Calibration

Basic Idea

The γ transition model is calibrated for high Reynolds number flows ($Re > 10^6$) at moderate to high Mach numbers ($M > 0.3$) in a low turbulence environment $\tau \leq 0.5$ %. Similar conditions are found in external aerodynamic flows over airfoils and wings. For a constant value of F_{length}, all coefficients of the transition onset correlation $Re_{\theta t} = f(\tau_\infty, K)$ are determined.

The effect of the turbulence level τ is based on a modified version of the correlation given by Mayle (1991). The asymptotic behavior of $Re_{\theta t}$ for $\tau \to 0$ allows a variation of $Re_{\theta t}$ that covers the strong scatter of experimental results for $\tau \ll 0.1$ %. Equation 4.28 is likely to overpredict $Re_{\theta t}$ for bypass transition ($\tau > 0.5 \ldots 1$ %) as the direct comparison to the correlations of Abu-Ghannam and Shaw (1980) and Mayle (1991) suggests.

For the influence of pressure gradients, it is assumed that the boundary layer transition is given by a correlation similar to the theoretical results of Wazzan et al. (1968). The acceleration parameter K is used rather than λ_θ because K can be computed directly without any iteration. Although no correlation $Re_{\theta t} = f(K)$ is found in literature, the basic behavior can be taken from Figure 16 in the lecture article by Mayle (1991).

The exact values of the coefficients in the transition correlation are found by matching the transition locations for different two-dimensional flows. These cases are listed in Tab. 4.1. The NLR 7301 case is used to calibrate the model for adverse pressure gradient flows. The NACA $65_{215} - 114$ and NLF(1)-0414F cases are used to calibrate the model for favorable pressure gradient flows. Especially cases for transition under a favorable pressure gradient are rare in

literature, which increases the difficulties to develop a sound basis for the model calibration and validation. A detailed description of the experimental data and the numerical set-up for each case can be found in Chapter 5.

Table 4.1: Calibration cases for the γ model

airfoil	τ / %	M	Re / 10^6
NLR 7301	0.05	0.299	1.1
NACA $65_{215} - 114$	0.05	0.2	30
NLF(1)-0414F	0.08	0.4	9.5

Solver Settings

Second order central discretization schemes are applied for the spatial discretization of the transport equations. In the case of the turbulence equations, a second order Roe scheme is used. An implicit LUSGS-time scheme is used for time integration with a local time stepping to accelerate the computation. For low Mach number cases, the TAU-Code low Mach number preconditioning is used (for detailed description see DLR AS 2015). All calibration computations are performed on sufficiently fine grids to obtain a grid independent transition location. The first cell height gives $y^+_{max} < 1$.

NLR 7301

The data presented by Zwaaneveld (1979) for the NLR 7301 at $M = 0.299$, $Re = 1.1 \cdot 10^6$ is used to build the basic correlation for adverse pressure gradient effects. At $M = 0.299$ a strong adverse pressure gradient exists on the upper surface downstream of the suction peak. On the lower surface, the boundary layer separates under an adverse pressure gradient. The detached flow undergoes transition and reattaches in a turbulent state. The model is calibrated to capture the transition location, the length of the transition zone on the upper surface, and the size of the laminar separation on the lower surface. The calibrated result is depicted on the left in Fig. 4.13.

NACA65(215)-114

Braslow and Visconti (1948) present experimental results for a NACA 65_{215}-114 with free boundary layer transition at high chord Reynolds numbers. To calibrate the model for a low

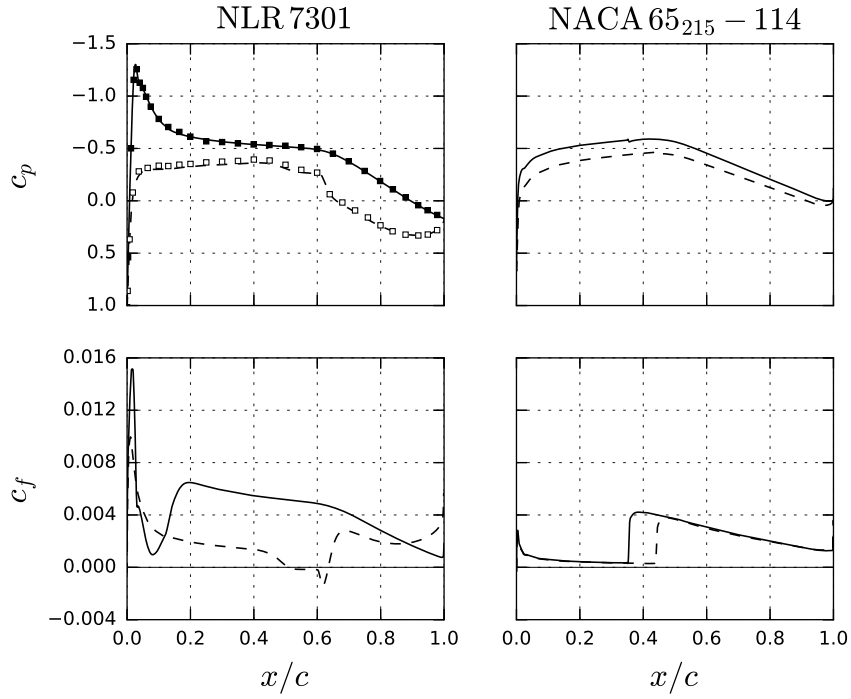

Figure 4.13: Transition model calibration for the NLR 7301 and NACA 65_{215}-114

turbulence level, high Reynolds number flow, the $Re = 30 \cdot 10^6$ case at $M = 0.2$ is used. The experimental transition location is $x/c \approx 0.375$ on the upper surface and $x/c \approx 0.43$ on the lower surface.

The model is calibrated to predict the transition location on the upper surface of the airfoil. The result is depicted on the right in Fig. 4.13. The local maximum in c_f is found at $x/c \approx 0.386$. At the point of the first intermittency increase, the scaled acceleration parameter K_t gives an increase of about 25 % in $Re_{\theta t}$ compared to a zero pressure gradient flow.

NLF(1)-0414F

Two angles of attack from Run 15 ($Re = 9.5 \cdot 10^6$, $M = 0.4$) from the experimental data of McGhee et al. (1984b) for the NLF(1)-0414F are used to determine the effect of favorable and adverse pressure gradients on the transition location.

The lower limit of the laminar drag bucket in Run 15 is reached at $\alpha = -2.52°$. For a small increase of α, the transition location on the lower surface moves downstream towards the trailing edge. At $\alpha = -0.97°$, the minimum drag is reached inside the drag bucket. At this angle of attack, large regions of laminar flow exist on the upper and lower surface. The CFD results for both angles of attack are given by full symbols in Fig. 4.14.

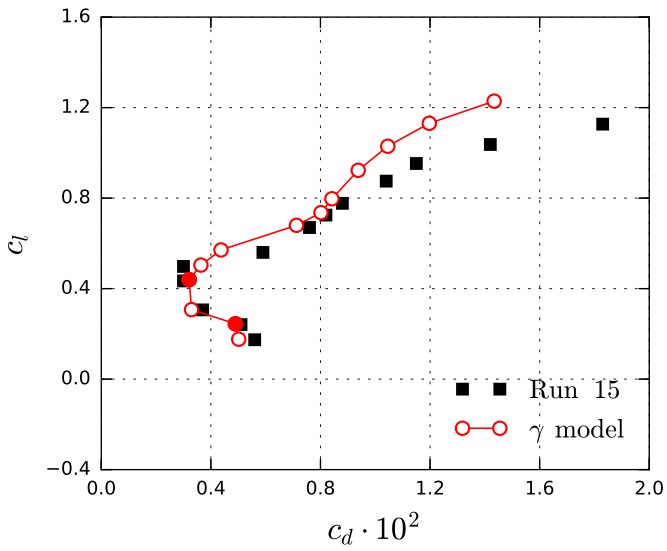

Figure 4.14: Transition model calibration for the NLF(1)-0414F: Drag curve

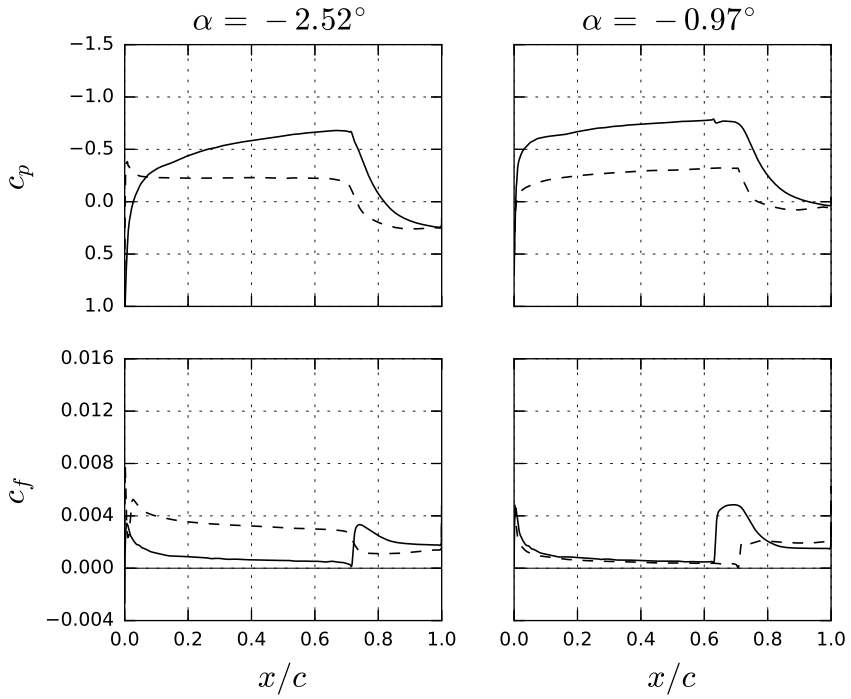

Figure 4.15: Transition model calibration for the NLF(1)-0414F: Pressure and skin friction coefficients

Figure 4.15 depicts the pressure and skin friction coefficients for both angles of attack computed with the γ transition model. The flow at $\alpha = -2.52°$ is accelerated up to $x/c \approx 0.7$ on the upper surface and the favorable pressure gradient stabilizes the boundary layer. On the lower surface, a small suction peak exists that causes transition. For $\alpha = -0.97°$, the favorable pressure gradient on the suction side reduces and the transition location moves towards the leading edge. The transition location on the lower surface is moved to the recompression area at 70 % chord as the suction peak at the leading edge vanishes.

5 Results

5.1 Flat Plate Test Cases

This section presents results for boundary layer flows on flat plates without pressure gradient. It will be shown that the calibrated γ transition model gives reasonable results for a certain range of turbulence conditions. All results are obtained on a computational grid with 500x100 nodes along the plate. The first cell height gives $y^+_{max} < 1$ for all cases with a growth ratio of 1.1 normal to the wall. The grid spacing in flow direction is refined at the leading edge. Table 5.1 presents the flow conditions for the cases investigated. In the following discussion, the subscript t denotes the start of the transition process, the subscript T gives the end of the transition region.

Table 5.1: Flow conditions for flat plate test cases

test case	U_∞ / (m/s)	τ / %	ρ / (kg/m^3)	μ / (kg/m/s)
Bennett (1953)	38.56	0.15 ... 0.45	1.2	$1.8 \cdot 10^{-5}$
Schubauer and Klebanoff (1955)	24.38	0.03	1.2	$1.8 \cdot 10^{-5}$
T3A	5.2	2	1.2	$1.8 \cdot 10^{-5}$
T3AM	19.8	0.5	1.2	$1.8 \cdot 10^{-5}$

5.1.1 Bennett (1953)

Bennett (1953) presents experimental results for zero pressure gradient flows on a flat plate. The flow velocity is $U_\infty = 120$ ft/s $= 36.58$ m/s for different turbulence levels. The Reynolds number at the end of transition Re_{xT} is read from Figure 12 in the report by Bennett (1953). The Reynolds number Re_{xT} and the turbulence level are given in Tab. 5.2. In addition, the momentum loss Reynolds number is given by (Schlichting and Gersten 2006):

$$Re_\theta = 0.664\sqrt{Re_x} \tag{5.1}$$

Table 5.2: Reynolds number at transition Re_{xT} from Bennett (1953)

τ / %	Re_{xT} / 10^6	$Re_{\theta T}$
0.15	3.827	1299
0.2	3.541	1249
0.25	3.255	1198
0.35	2.663	1084
0.45	1.969	932

The Reynolds number Re_{xT} from the γ transition model is defined as the point of the local maximum in the skin friction distribution downstream of the transition onset. The left part of Fig. 5.1 depicts Re_{xT} from the experiment and the γ transition model. The right part depicts $Re_{\theta T}$ given by equation 5.1 based on Re_{xT}. In addition, the transition onset correlation for $Re_{\theta t}$ from equation 4.28 is included.

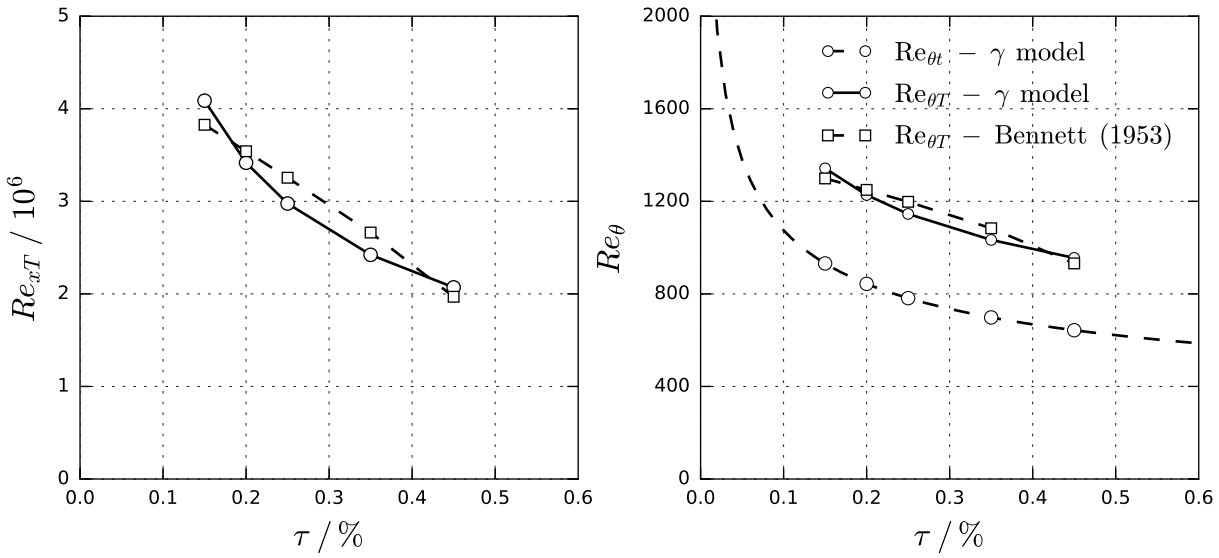

Figure 5.1: Flat plate experiment by Bennett (1953): Transition locations for different turbulence levels

The transition location is matched reasonably well for all turbulence levels. From the right part of Fig. 5.1 it can be seen that a constant offset between the end of transition and the

transition onset is given. The offset is determined by the value of F_{length} for a given transition onset correlation.

5.1.2 Schubauer and Klebanoff (1955)

Schubauer and Klebanoff (1955) present a flat plate transition experiment with a low turbulence levels of $\tau = 0.03$ %. No skin friction coefficients are given, but Figure 3 in the report by Schubauer and Klebanoff (1955) depicts intermittency measurements for different x-coordinates for a flow velocity of $U_\infty = 80$ ft/s = 24.38 m/s. The intermittency values are used to compute a friction coefficient based on the assumption of Emmons (1951):

$$c_f = c_{fL}\,(1-\gamma) + c_{fT}\gamma \tag{5.2}$$

The laminar skin friction coefficient is approximated by (Schlichting and Gersten 2006):

$$c_{fL} = 0.664/\sqrt{Re_x} \tag{5.3}$$

and the turbulent skin friction coefficient by (White 1991):

$$c_{fT} = 0.027/Re_x^{1/7} \tag{5.4}$$

Figure 5.2 depicts the results for the γ transition model and the computed skin friction coefficients from the intermittency data of Schubauer and Klebanoff (1955). The transition model is not able to reproduce the transition location and a laminar flow is predicted. In addition, the result for the γ-Re_θ model with freely decaying turbulence is depicted. The inflow conditions are set according to Langtry and Menter (2009) with $\tau_\infty = 0.3$ % and $R_{T\infty} = 1$. Langtry and Menter (2009) state a local freestream turbulence intensity[1] of $\tau = 0.18$ %. The transition location is met for these conditions. However, for the increased turbulence level, the γ model is also able to predict the experimental transition location.

Figure 5.3 depicts the Re_θ distribution given by the γ transition model on the left. The velocity profiles are integrated to compute θ by (Schlichting and Gersten 2006):

$$\theta = \int_0^\infty \frac{u}{U}\left(1-\frac{u}{U}\right) dy \tag{5.5}$$

In addition, $Re_\theta = Re_{\nu,\,max}/\xi$ is depicted. Both Re_θ distributions are in good agreement. In the case of the experiment, the fully turbulent state is reached at $Re_{xT} = 3.96 \cdot 10^6$, which gives $Re_{\theta T} = 1321$. In the right part of Fig. 5.3, $Re_{\theta T}$ is compared to the transition onset correlation.

[1]The value is most likely taken at the location of the first intermittency increase.

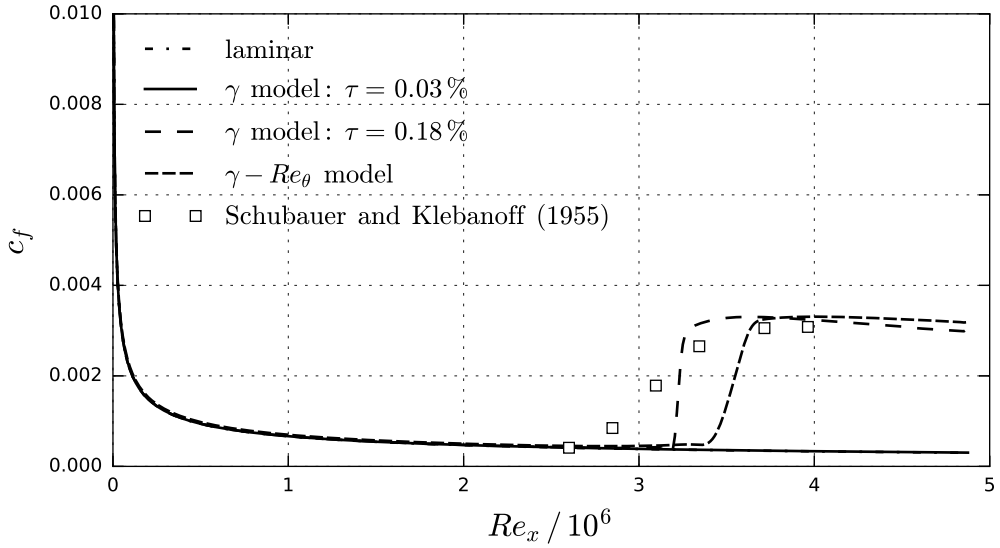

Figure 5.2: Skin friction coefficients computed from intermittency distribution (Schubauer and Klebanoff 1955) and from the transition models

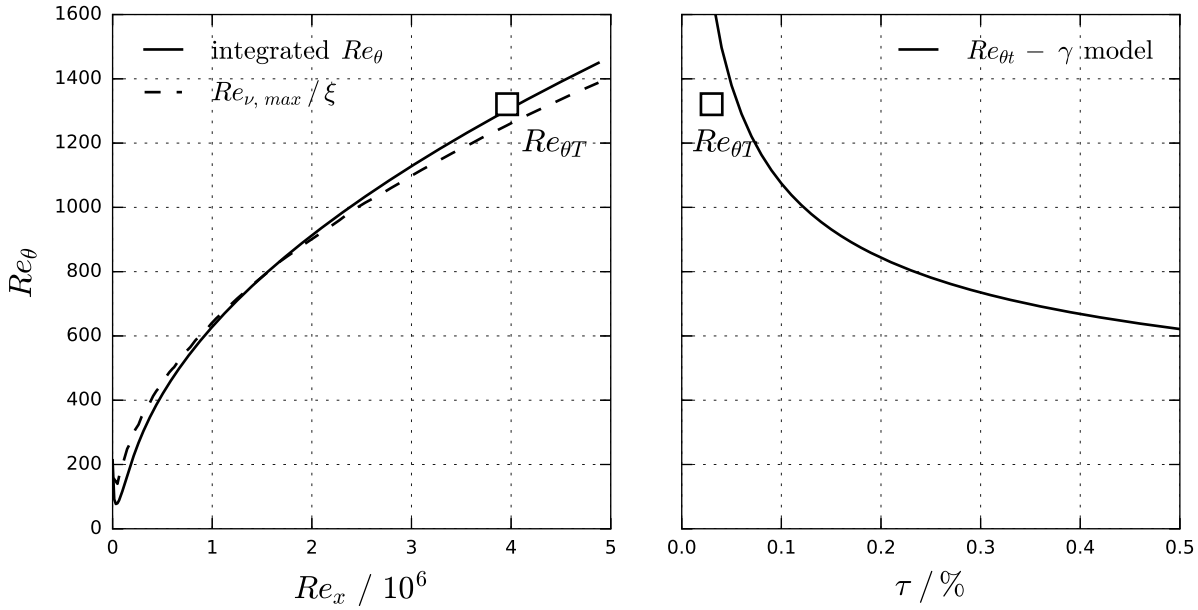

Figure 5.3: Re_θ and $Re_{\theta t}$ from the γ transition model and $Re_{\theta T}$ from Schubauer and Klebanoff (1955)

$Re_{\theta t}$ from the γ transition model is too large to predict the transition onset correctly. The computation for the Bennett (1953) test case for $\tau = 0.15$ % gives an offset of $Re_{\theta T} - Re_{\theta t} \approx 411$. To predict the Schubauer and Klebanoff (1955) test case correctly, a value as low as $Re_{\theta t} = 920$ is required in the onset correlation if the same offset is assumed. This value contradicts test cases presented later.

5.1.3 ERCOFTAC T3 Series

Series Description

The ERCOFTAC T3 flat plate series contains well documented test cases for zero and non-zero pressure gradient flows (Roach and Brierly 1992; Savill 1992). The T3 data is often used to calibrate transition models (see e.g. Menter et al. 2006; Langtry 2006; Krause et al. 2008; Suluksna et al. 2009; Malan et al. 2009). The test cases show high turbulence levels and low flow velocities. The T3A and T3AM cases are evaluated with the γ transition model.

T3A: Zero Pressure Gradient, High Turbulence Level

Based on the high inflow turbulence level of $\tau_\infty \approx 3$ %, a bypass transition mechanism can be expected for the T3A test case. At the transition onset, the turbulence level is $\tau \approx 2$ %. To match the high turbulence level in the experiment, a high viscosity ratio R_T is required if no sustaining turbulence approach is used. Figure 5.4 gives an example of turbulence conditions to meet the T3A turbulence level along the plate.

In the experiment, the skin friction values start to deviate from the laminar solution at $Re_{xt} = 1.348 \cdot 10^5$. The boundary layer is fully turbulent at $Re_{xT} = 2.735 \cdot 10^5$. A turbulence level of $\tau = 2$ % is used in the computation with the sustaining turbulence approach. The viscosity ratio is set to $R_T = 1$, which is the default value for the γ transition model. In addition, a computation for $R_T = 11$ is performed. The high viscosity ratio matches the value for a free turbulence decay rate at the transition location (see Fig. 5.4). The T3A case is usually computed with high R_T values (see e.g. Langtry 2006; Menter et al. 2015). A computation with the γ-Re_θ model for freely decaying turbulence is also performed. The inflow conditions are set according to Langtry and Menter (2009) with $\tau_\infty = 3.3$ % and $R_{T\infty} = 12$.

Figure 5.5 presents the experimental results, the γ transition model results for $R_T = 1$ and $R_T = 11$ for a turbulence level of $\tau = 2$ %, and the results for the γ-Re_θ model. In addition, results for $R_T = 1$ and $\tau = 0.2$ % are included for the γ model. The transition location is neither met for the $R_T = 1$ cases nor the $R_T = 11$ case with the γ model. The results depend strongly on the viscosity ratio. The $R_T = 1$ case with $\tau = 2$ % shows an erroneous transition

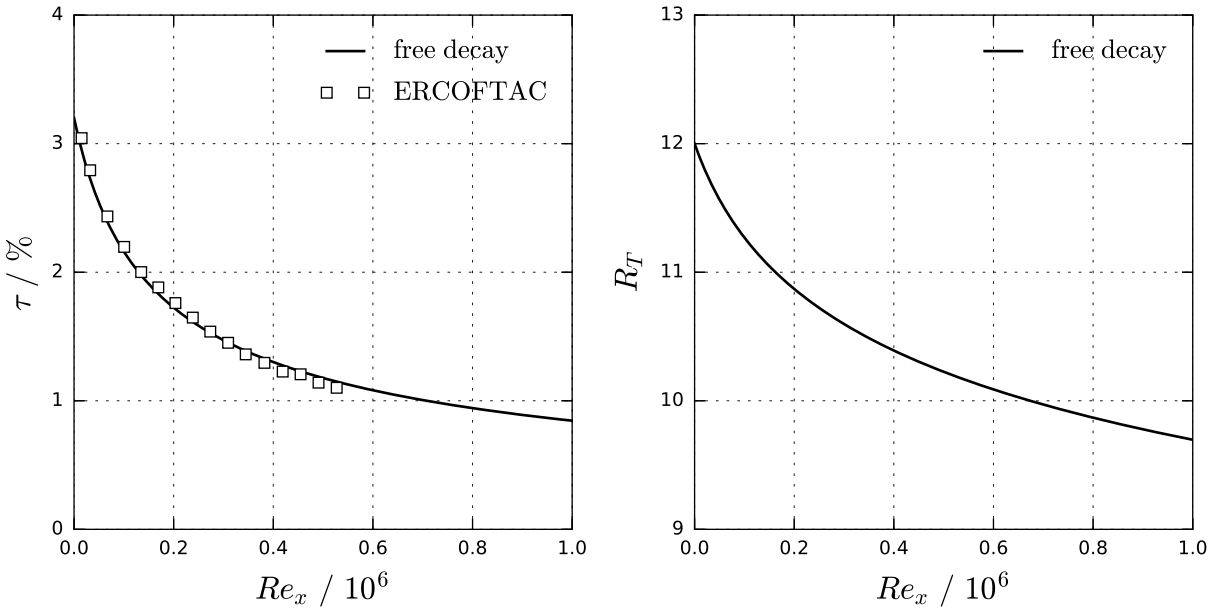

Figure 5.4: T3A: Turbulence decay

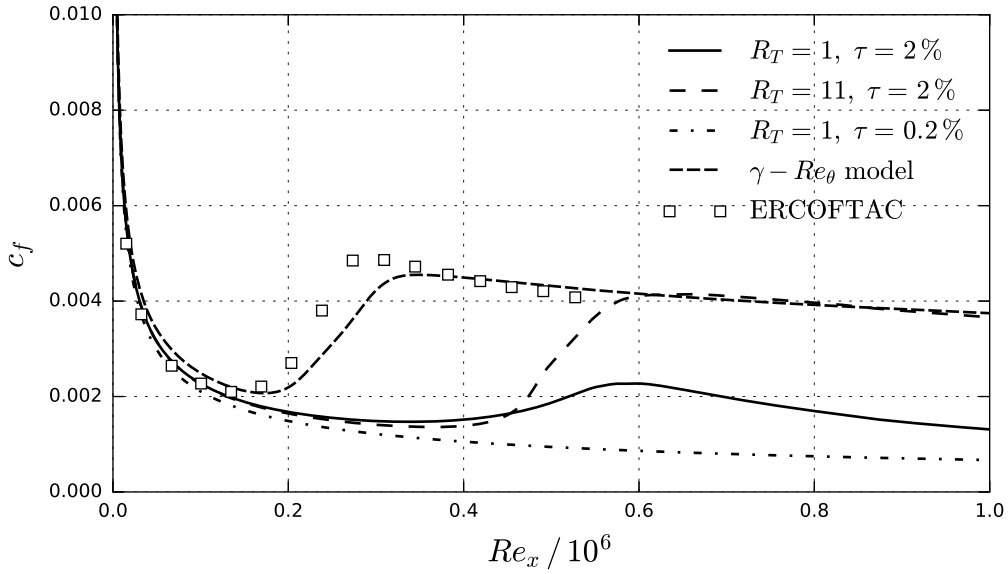

Figure 5.5: T3A: Skin friction coefficients

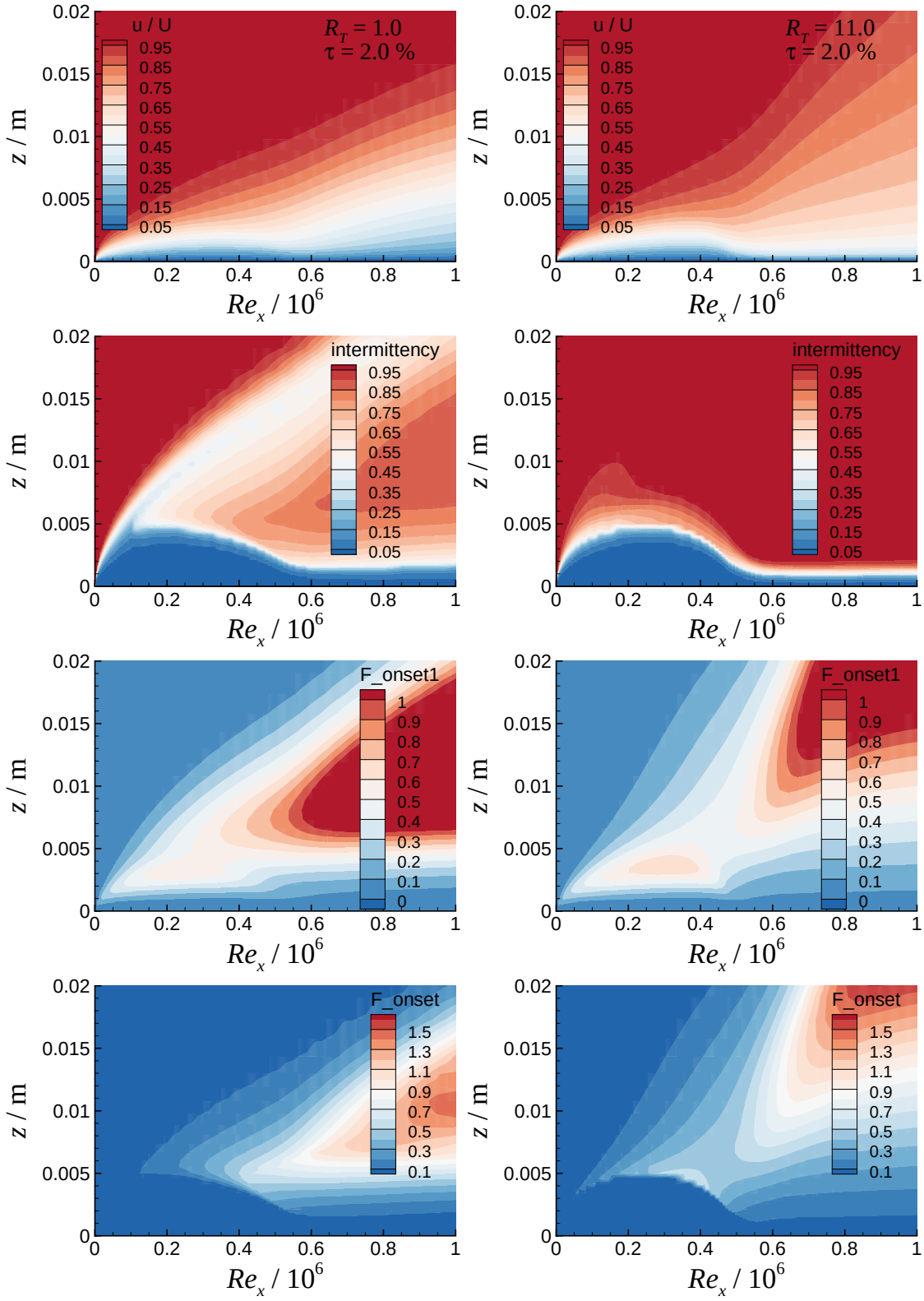

Figure 5.6: T3A: Velocity, intermittency, F_{onset1}, and F_{onset} for $R_T = 1$ and $R_T = 11$, $\tau = 2$ %

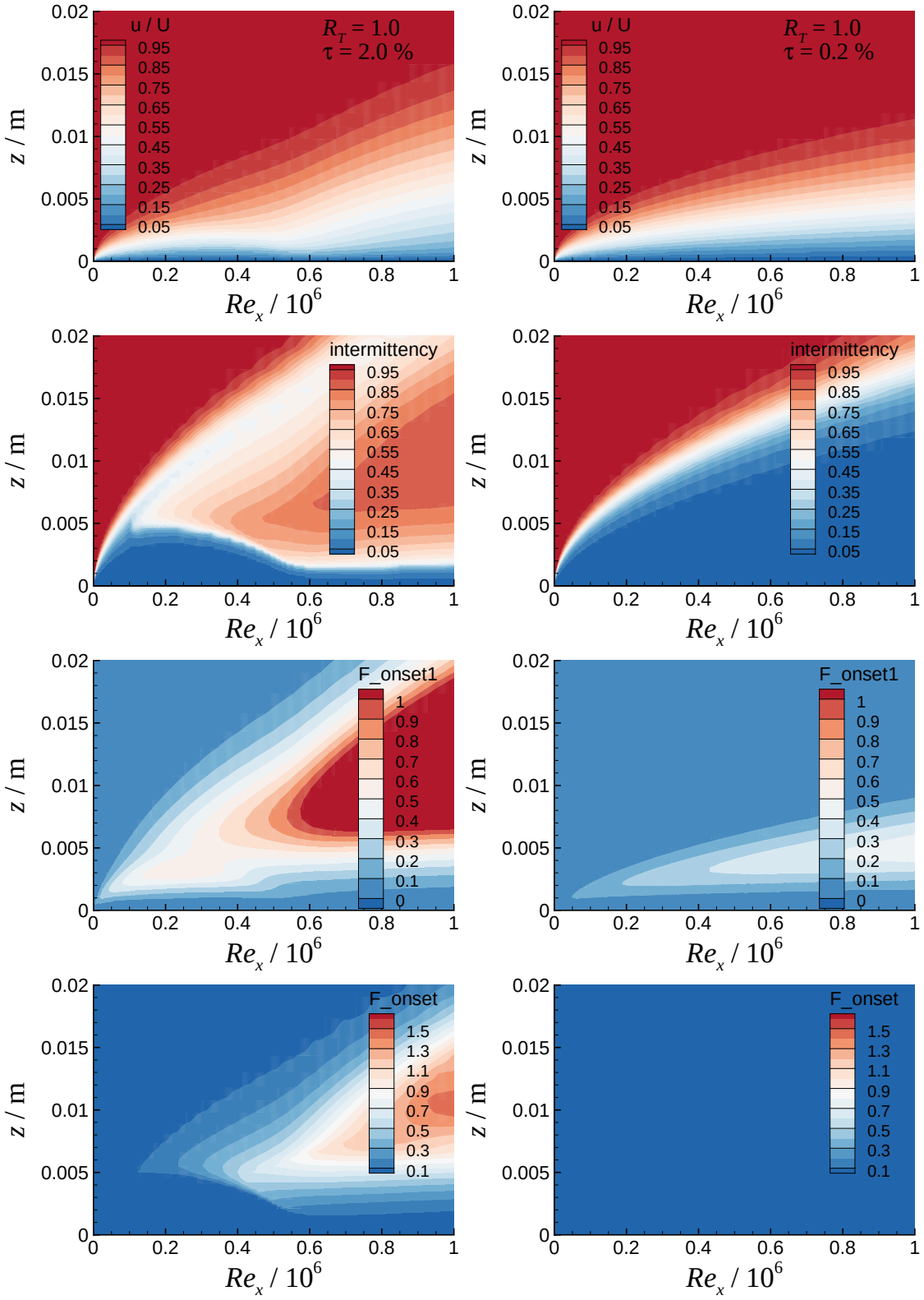

Figure 5.7: T3A: Velocity, intermittency, F_{onset1}, and F_{onset} for $\tau = 2$ % and $\tau = 0.2$ %, $R_T = 1$

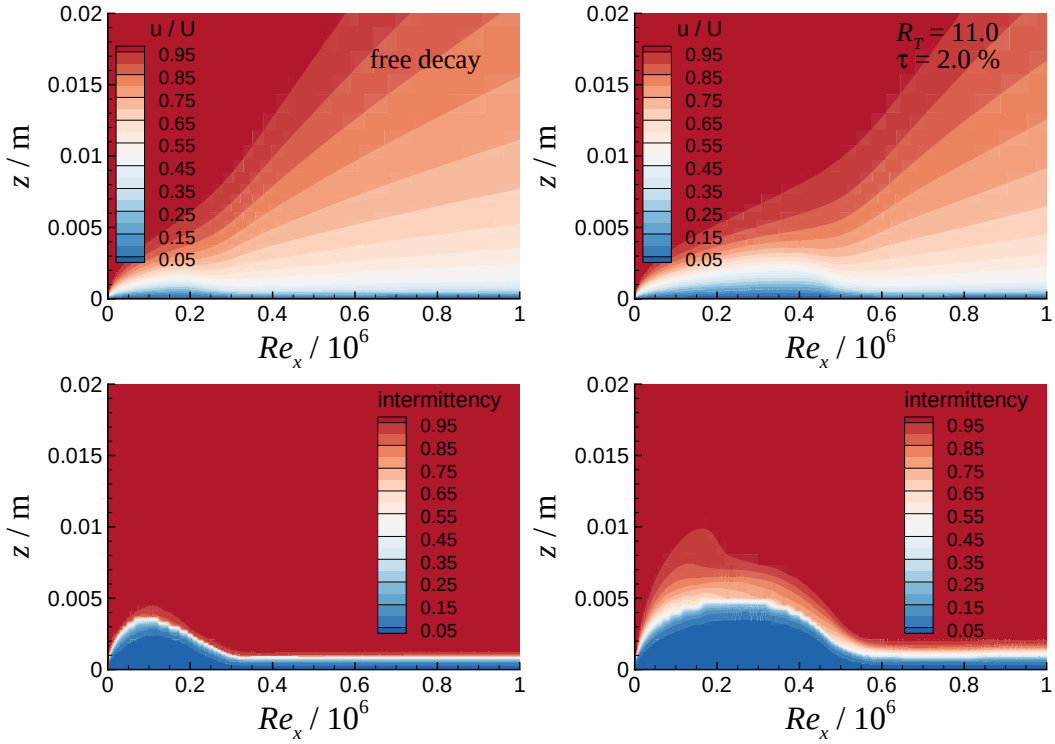

Figure 5.8: T3A: γ-Re_θ model with decaying turbulence (left) and γ model with sustaining turbulence (right)

behavior as the skin friction coefficients deviate from the laminar solution, but a fully turbulent state is not reached. The γ-Re_θ model reproduces the experimental results within the expected accuracy.

Figure 5.6 and 5.7 depict the velocity distribution, the intermittency distribution, the term F_{onset1}, and F_{onset} for the γ transition model. For both high turbulence cases in Fig. 5.6, the intermittency starts to grow at the boundary layer edge. At the bounday layer edge, the transition criterion is not given as $F_{onset1} < 1$. For $R_T = 11$, the high viscosity ratio at the boundary layer edge gives a decrease of F_{onset3}, which allows an intermittency production without $F_{onset1} > 1$. This behavior is required to maintain the intermittency production for cases with a long transition region or a confined transition mechanism (suction peak). For the $R_T = 11$ case, the model behavior is erroneous as the F_{onset1} transition criterion has not been reached at the first intermittency increase. The $\tau = 2$ % case with $R_T = 1$ shows a similar misbehavior. For $\tau = 0.2$ % in Fig. 5.7, the boundary layer stays laminar as F_{onset} is not affected by the freestream turbulence.

Figure 5.8 depicts the velocity distribution and the intermittency increase for the γ-Re_θ model (left) and the γ model (right). The γ-Re_θ model shows the same intermittency increase

initiated from the freestream. The actual transition criterion with $F_{onset1} > 1$ is not given at this location.

The γ transition model should not be used with freestream viscosity ratios $R_T > 1$ for T-S transition as R_T is used in the transition onset criterion. Any intermittency increase should start inside the boundary layer at the local maximum of the vorticity Reynolds number Re_ν for a T-S transition mode. The γ transition model shows a similar transition behavior as the γ-Re_θ model in a high turbulence environment, which is associated with bypass or wake-induced transition. The high freestream viscosity ratio initiates an intermittency growth, starting at the boundary layer edge. In the case of the γ transition model, this effect is not calibrated or tested systematically to account for any bypass or wake-induced transition yet.

T3AM: Zero Pressure Gradient, Low Turbulence Level

The T3AM case is the experimental setup with the highest flow velocity $U_\infty = 19.8$ m/s and the lowest turbulence level $\tau \approx 0.5$ % at the transition location. The low turbulence level allows T-S transition. Therefore, the case is suited to test the γ transition model's prediction capabilities. In addition to the γ model, the results for the γ-Re_θ transition model are included. The inflow conditions are set according to Langtry and Menter (2009) with $\tau_\infty = 0.874$ %, $R_{T\infty} = 8.72$, and freely decaying turbulence for the γ-Re_θ model. In the case of the γ transition model, the turbulence level is set to $\tau_\infty = 0.5$ % and $R_{T\infty} = 1$ with sustaining turbulence.

Figure 5.9 depicts the skin friction coefficients. In addition to the experimental and computed values, the theoretical curve for a laminar boundary layer from equation 5.3 is given. The experimental c_f values start to deviate from the laminar solution at about $Re_x \approx 1.7 \cdot 10^6$. The γ transition model gives the main c_f increase at this location. The gradual increase in skin friction from the experiment is not reproduced by the γ transition model. The γ-Re_θ transition model gives a good prediction of the onset and the slope of the skin friction increase.

Figure 5.10 depicts the momentum loss thickness Reynolds number Re_θ. The boundary layer velocity profiles from the γ transition model are integrated to give Re_θ. In addition, the correlated momentum loss thickness Reynolds number given by $Re_{\nu,\,max} \,/\, \xi$ is depicted and compared to the experimental ERCOFTAC data. Both, the integrated and correlated values of Re_θ are in good agreement with the experimental data up to $Re_x = 10^6$. The intermittency starts to increase at this point and the agreement is lost for the correlated value $Re_\theta = Re_{\nu,\,max} \,/\, \xi$ as the intermittency changes du/dy. The effect is less pronounced for the integrated value of Re_θ based on the flow field data. The intermittency distribution for the γ model is depicted in Fig. 5.11.

Based on the skin friction coefficients, the transition onset given by the γ transition model is

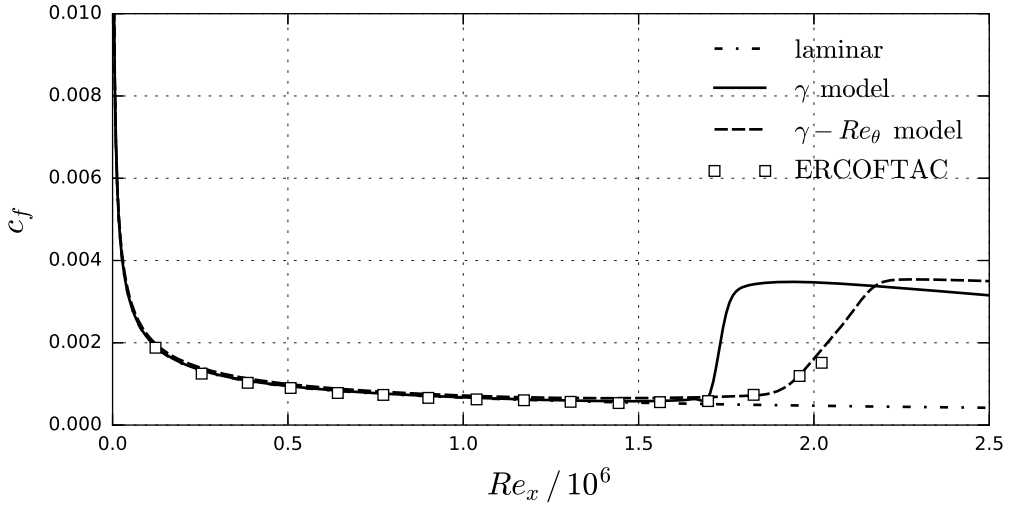

Figure 5.9: T3AM: Skin friction coefficients

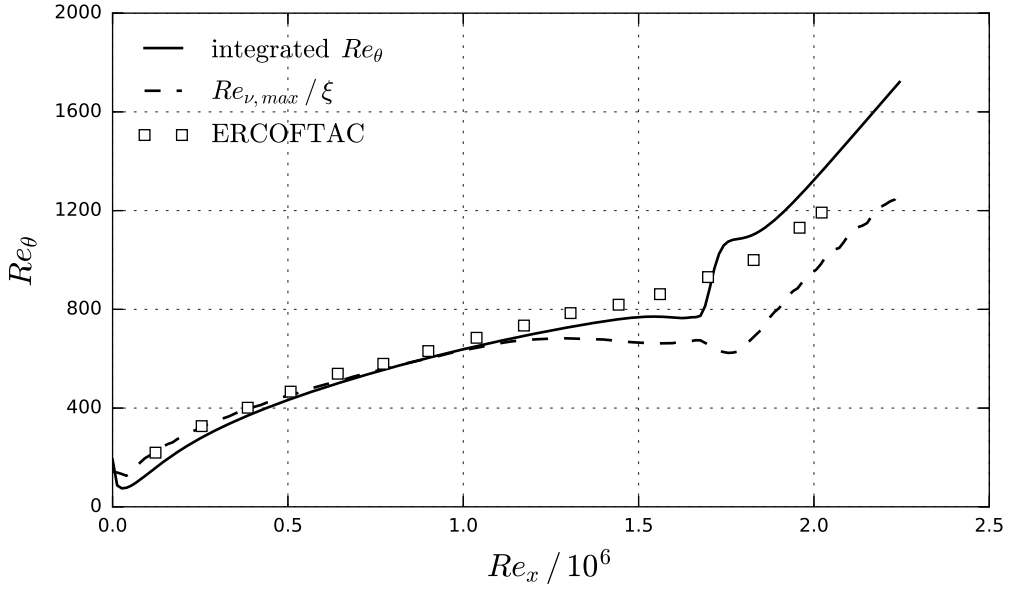

Figure 5.10: T3AM: Momentum loss thickness Reynolds number

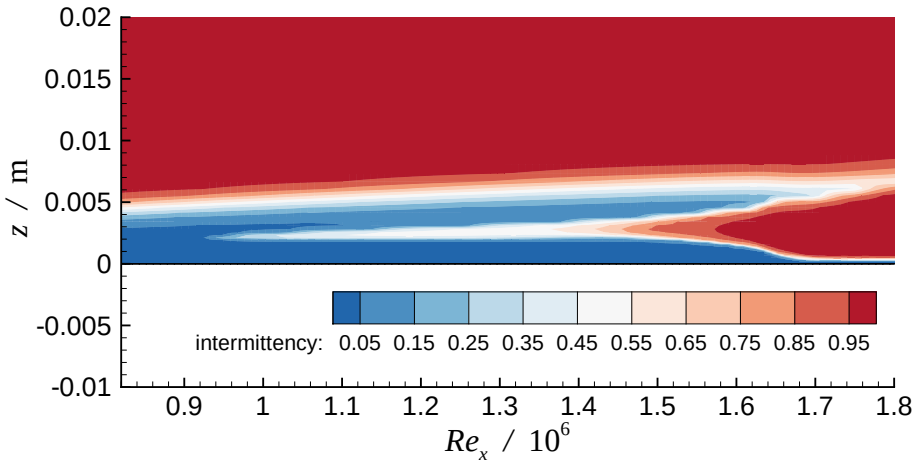

Figure 5.11: T3AM: Intermittency distribution

in good agreement with the experiment. The increase in skin friction is caused by the changed velocity gradient at the wall $(du/dy)_w$ and the intermittency has to grow towards the wall to change this velocity gradient. The intermittency increases from $Re_{xt} = 10^6$ to $Re_{xT} \approx 1.7 \cdot 10^6$ in the boundary layer, but there is no significant increase of skin friction in this transition region upstream of $Re_x \approx 1.7 \cdot 10^6$. Based on the first intermittency increase, the transition onset is too far upstream.

The intermittency variable of the γ transition model does not represent the intermittent boundary layer behavior in a flow. The slow increase in c_f in the experimental data is most likely linked to the time averaged effect of turbulent fluctuations (physical intermittency). This process is not represented in the γ transition model as the intermittency is used as a blending function for the production of turbulent kinetic energy k. For this reason, a comparison of $Re_{\theta t}$ given by the transition model and the experimental $Re_{\theta t}$ can be misleading. The end of the transition process given by Re_{xT} or $Re_{\theta T}$ is more precise in a comparison between transition model and experimental results.

5.1.4 Grid Dependency: Flat Plate

The grid dependency of the γ transition model is similar to the γ-Re$_\theta$ transition model described by Langtry (2006). The grid density in the streamwise direction has to be higher, compared to fully turbulent computations. On very coarse grids, the intermittency production will be altered and the transition behavior changes. The T3AM test case is used to depict this grid dependency. Table 5.3 lists the different grids with the number of grid points along the wall p and the overall number of grid points n in one symmetry plane.

Table 5.3: T3AM: Grid dependency

	p	n	$n^{-1/2} \cdot 10^3$
very coarse	125	66 036	3.891
coarse	250	124 683	2.832
medium	500	195 425	2.262
fine	1000	350 463	1.689

Figure 5.12 depicts the results for the four grids in terms of the global skin friction coefficient C_f and the local skin friction coefficients c_f. On the very coarse grid, the development of c_f deviates from the finer grids although the fully turbulent boundary layer is given at the same location. No benefit exists for the fine grid compared to the medium grid. The transition behavior does not change significantly.

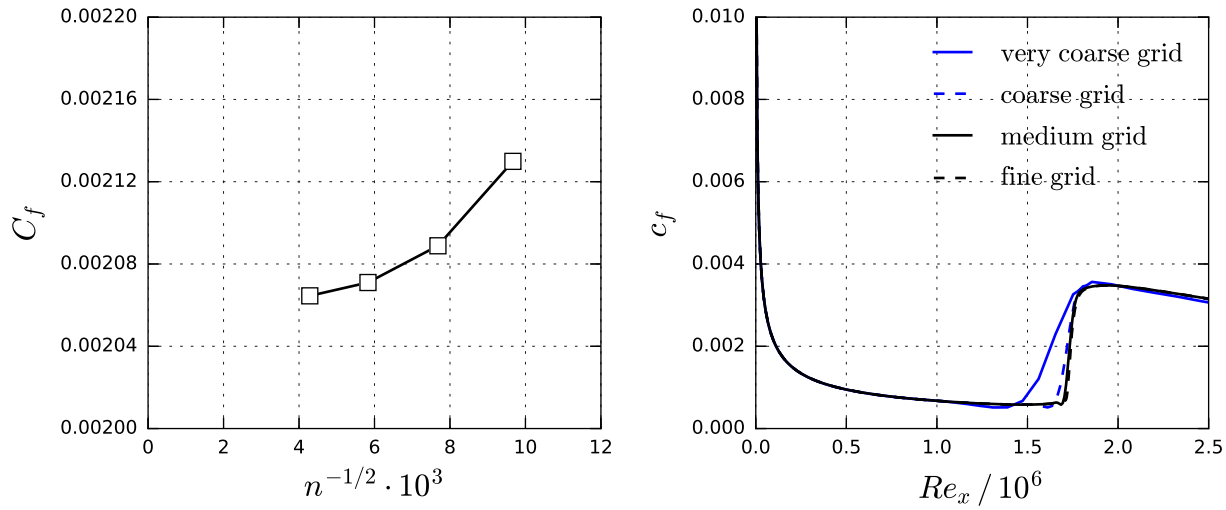

Figure 5.12: T3AM: Grid dependency

5.2 Steady Airfoil Test Cases

5.2.1 NLR 7301

Airfoil and Test Case Description

The AGARD report AR-138 (Zwaaneveld 1979) contains a wind tunnel test for the NLR 7301 airfoil with free boundary layer transition. The measurements are contributed by the National Aerospace Laboratory (NLR), Amsterdam. A detailed description of the test is given by Zwaaneveld (1976). The NLR 7301 is an aft-loaded, supercritical airfoil with a maximum thickness $t/c = 16.3$ %. In potential flow, the shock-free design point is given at $Ma = 0.721$ with $c_l = 0.595$. The airfoil represents the 42 % half-span section of a supercritical wing (Zwaaneveld 1976). The design method is described by Boerstoel and Huizing (1975).

In the wind tunnel test, the theoretical airfoil geometry is cut-off at $x/c = 0.985$ to obtain a finite trailing edge. This results in a rotation of the airfoil by $\Delta\alpha = -0.194°$ compared to the design coordinate system. The airfoil coordinates are taken from Zwaaneveld (1979). The NLR 7301 is depicted in Fig. 5.13.

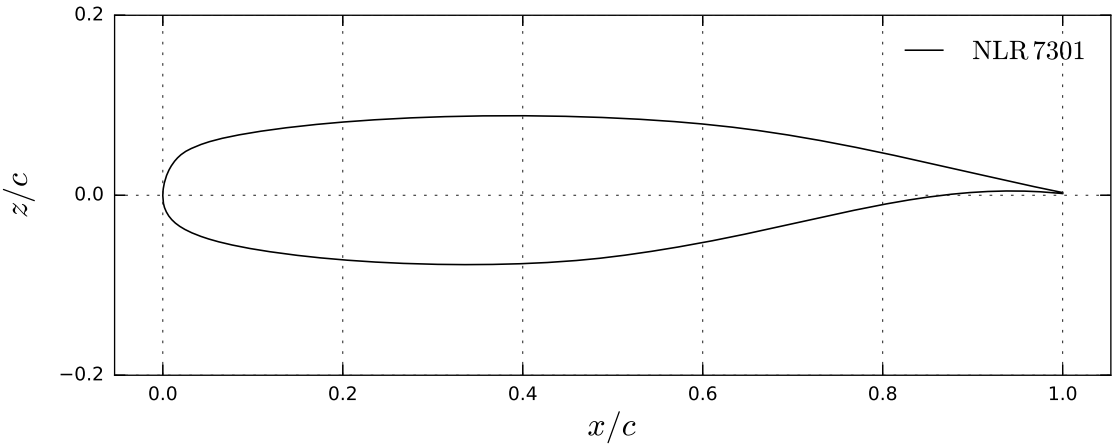

Figure 5.13: NLR 7301: Geometry

The experimental data contain fully turbulent and transitional results for a Mach number variation at a constant angle of attack and an angle of attack variation at a constant transonic Mach number. For the fully turbulent flow, the boundary layer is tripped at $x/c = 0.3$. In certain cases, transition takes place upstream of the transition tripping.

The experiments are performed in the NLR Pilot tunnel, which is a continuous, closed circuit wind tunnel with slotted top and bottom walls (Zwaaneveld 1979). The turbulence level is given in terms of pressure fluctuations $c_{p,\,rms}$. Under the assumption of plane sound waves, the pressure fluctuations are transformed to velocity fluctuations (Michel and Froebel 1988):

$$Tu = \frac{\sqrt{\overline{u'^2}}}{U_\infty} = \frac{1}{2}\, c_{p,\,rms}\, M \tag{5.6}$$

Table 5.4 gives the turbulence level $c_{p,\,rms}$ (Zwaaneveld 1979, Fig 4.5) and τ for the NLR Pilot tunnel. The turbulence level increases for increasing Mach numbers. Turbulence measurements are prone to measurement errors, and there is no information available on the size of the measurement errors. In addition, equation 5.6 only represents the effect of plain sound waves. Fluctuations due to acoustical standing waves or free shear layers and boundary layers are not included (Michel and Froebel 1988).

Table 5.4: NLR Pilot Tunnel: $c_{p,\,rms}$ and τ

M	$c_{p,\,rms}$ / %	τ / %
0.4	0.35	0.07
0.45	0.37	0.083
0.5	0.38	0.095
0.55	0.41	0.113
0.6	0.42	0.126
0.65	0.425	0.138
0.7	0.425	0.149
0.75	0.42	0.158
0.8	0.4	0.16
0.825	0.375	0.15

Mach Number Sweep

The Mach number sweep presented by Zwaaneveld (1979) is computed with the γ transition model. The wind tunnel test is conducted at a constant, nominal angle of attack of $\alpha_n = 0.85°$ (except for $M = 0.299$ with $\alpha_n = 0.84°$). For each Mach number, a wind tunnel correction for the angle of attack α_{corr} is given by Zwaaneveld (1979), based on the measured lift coefficient, moment coefficient, and Mach number. For the CFD computations, an angle of attack is used that gives the correct suction peak on the upper surface of the airfoil. The flow conditions are listed in Tab. 5.5.

Table 5.5: NLR 7301: Mach number sweep

$Re\,/\,10^6$	M	α_{corr} / deg	α_{CFD} / deg	τ / %	$c_{p,crit}$
1.1	0.299	0.3966	0.78	0.05	−6.998
1.7	0.502	0.3909	0.58	0.095	−2.112
1.9	0.599	0.3832	0.52	0.126	−1.301
2.0	0.649	0.3833	0.48	0.138	−1.014
2.1	0.699	0.388	0.4	0.149	−0.783
2.2	0.724	0.378	0.3	0.153	−0.684
2.2	0.747	0.2152	0.41	0.158	−0.602
2.2	0.774	0.2544	0.75	0.159	−0.513
2.3	0.8	0.4251	1.2	0.16	−0.435
2.3	0.825	0.5681	1.2	0.155	−0.366

Figure 5.14 depicts the transition locations read from Zwaaneveld (1979, Fig. 4.7, p. A4-16) and the computational results for the γ transition model. Zwaaneveld (1979) does not give detailed information on how the transition location is defined or measured. Surface flow visualizations are mentioned without any further explanation. It is most likely that the transition location identifies the end of the transition region. Therefore, the local maximum in the c_f distribution from the CFD results is given in Fig. 5.14. In the case of a laminar separation, the point is given at which the intermittency has grown towards the wall. An example is depicted in Fig. 5.15: The separated flow undergoes transition. Inside the separation bubble the intermittency increases at the recirculation vortex. The transition position is defined as $x/c \approx 0.61$ for this case, as the intermittency has grown towards the wall at this location.

The transition positions from the γ transition model and the experimental results agree reasonably well for most Mach numbers. Especially the transition movement towards the trailing edge for $M > 0.7$ on the upper surface is captured. For most Mach numbers, laminar separation bubbles occur. For high Mach numbers, the laminar separations are connected to shocks.

Figure 5.16 to 5.20 depict the pressure and skin friction coefficients for the Mach number sweep. The symbols indicate the experimental results and the lines give the γ transition model results. Full symbols and solid lines depict the upper surface, open symbols and dashed lines depict the lower surface. In addition, the critical pressure coefficient is given by the horizontal

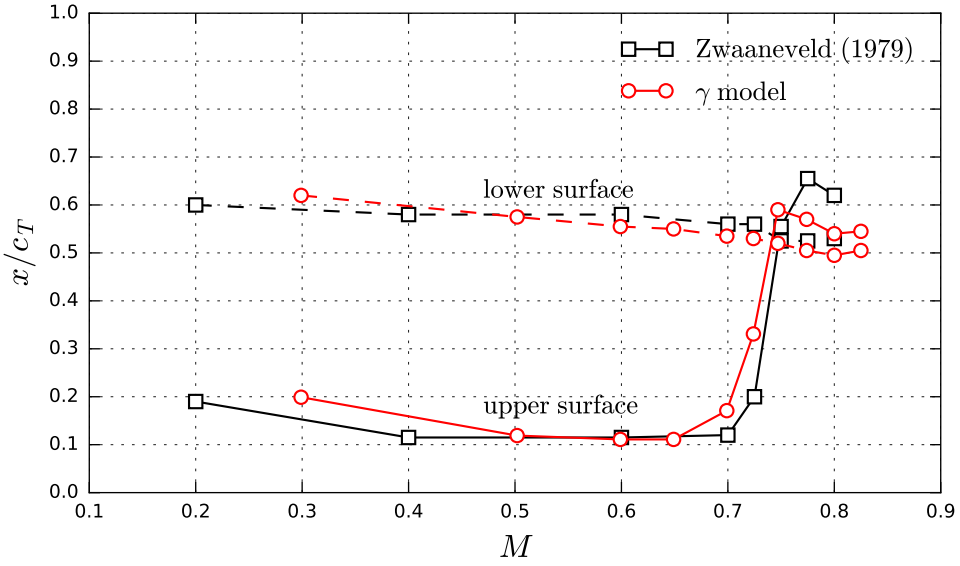

Figure 5.14: NLR 7301: Transition locations for the Mach number variation

line in the pressure distribution.

Figure 5.16: The flow is subsonic for $M = 0.299$ and 0.502. The $M = 0.299$ case is used to calibrate the model. Therefore, the pressure distribution on the upper surface and the size of the laminar separation is met. The agreement for $M = 0.502$ is almost as good as for $M = 0.299$. The transition zone length gets smaller and deviations in the pressure distribution are found at the transition location on the upper surface.

Figure 5.17: The flow is transonic at the suction peak for $M = 0.599$ and 0.649. The computed pressure distribution on the upper surface starts to deviate from the experimental data. The transition region length is predicted too small. For $M = 0.649$, the laminar flow is close to separate on the upper surface. A small laminar separation bubble downstream of the suction peak probably exists in the experiment.

Figure 5.18: Transonic flow exists on the upper surface for $M = 0.699$ and 0.724. In the case of $M = 0.699$, the predicted laminar separation on the upper surface is too small. For $M = 0.724$, the shock position moves downstream. The boundary layer does not separate in the computation and stays laminar up to the shock-induced transition at $x/c \approx 0.28$. In the experiment, the flow separates and the transition position is further upstream. The laminar separation bubble on the lower side of the airfoil is predicted too small by the transition model.

Figure 5.19: Transonic flow exists on the upper and lower surface for $M = 0.747$ and 0.774. The $M = 0.747$ test case "*is the shock-free (or practically shock-free) experimental design condition ... embedded in a M-α region with weak shocks*" (Zwaaneveld 1976, p. 6). The

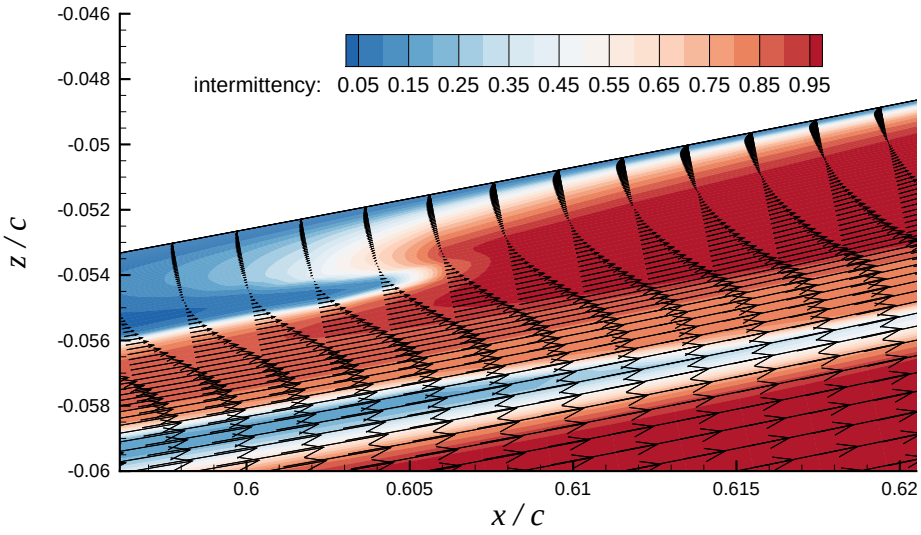

Figure 5.15: NLR 7301: Separation induced transition – Intermittency distribution and velocity vectors

computed flow matches the experimental flow at $M = 0.754$ depicted by Zwaaneveld (1976)(Fig. 2), which indicates the high Mach number sensitivity of the flow state. For $M = 0.774$ the agreement is poor. The shock is too far upstream in the CFD computation and the boundary layer reattaches only slightly. The computed flow separation on the lower surface is too far downstream.

Figure 5.20: Transonic flow on the upper and lower surface for $M = 0.8$ and 0.825. The shock position is too far upstream in the CFD computation, and the laminar flow on the lower surface separates too far downstream. For both Mach numbers, the flow is detached up to the trailing edge, which is not the case in the experimental data. The transition model is not able to reproduce the correct development of large separation bubbles in transonic flow.

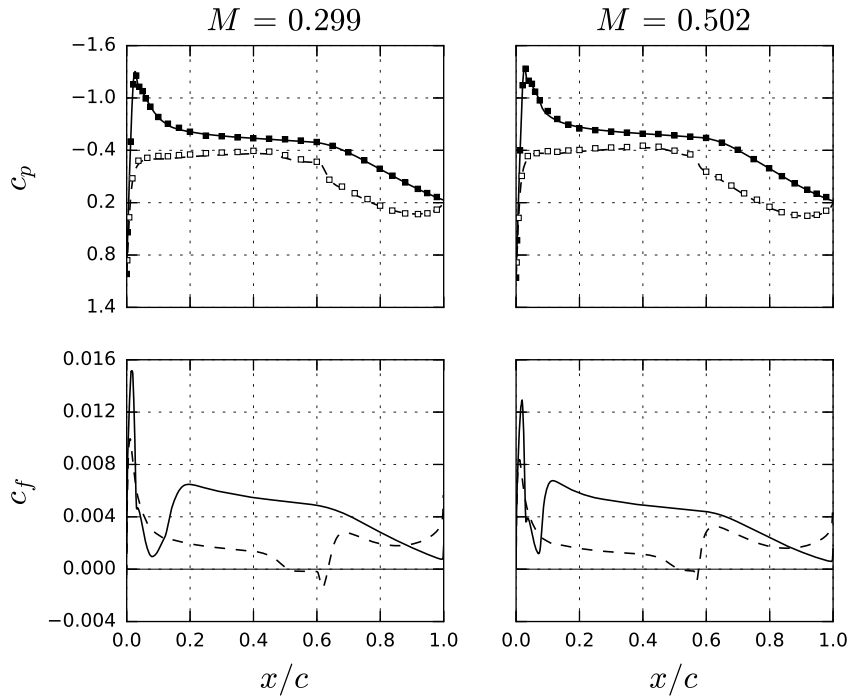

Figure 5.16: NLR 7301: Pressure and skin friction coefficients: $M = 0.299$ and $M = 0.502$

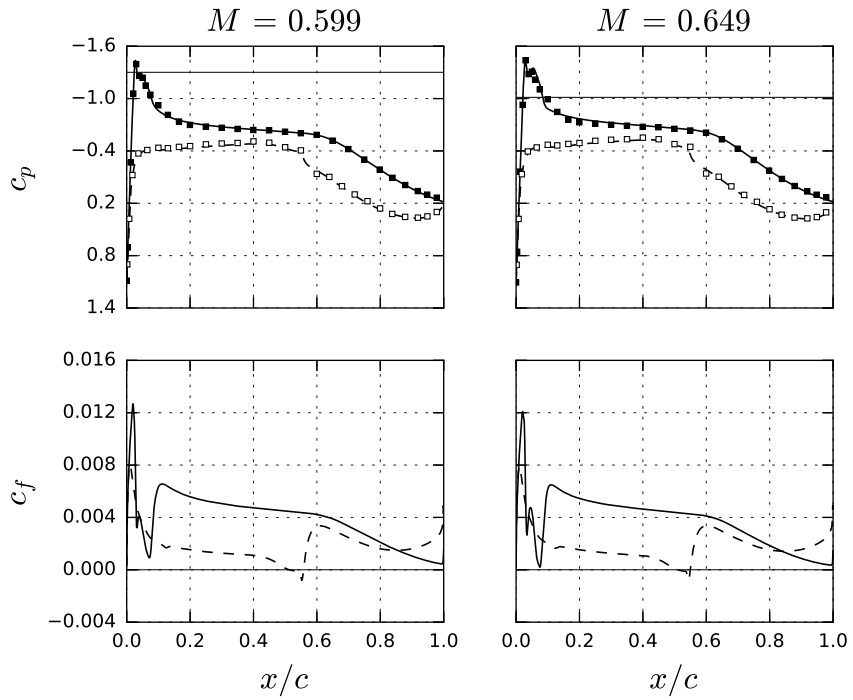

Figure 5.17: NLR 7301: Pressure and skin friction coefficients: $M = 0.599$ and $M = 0.649$

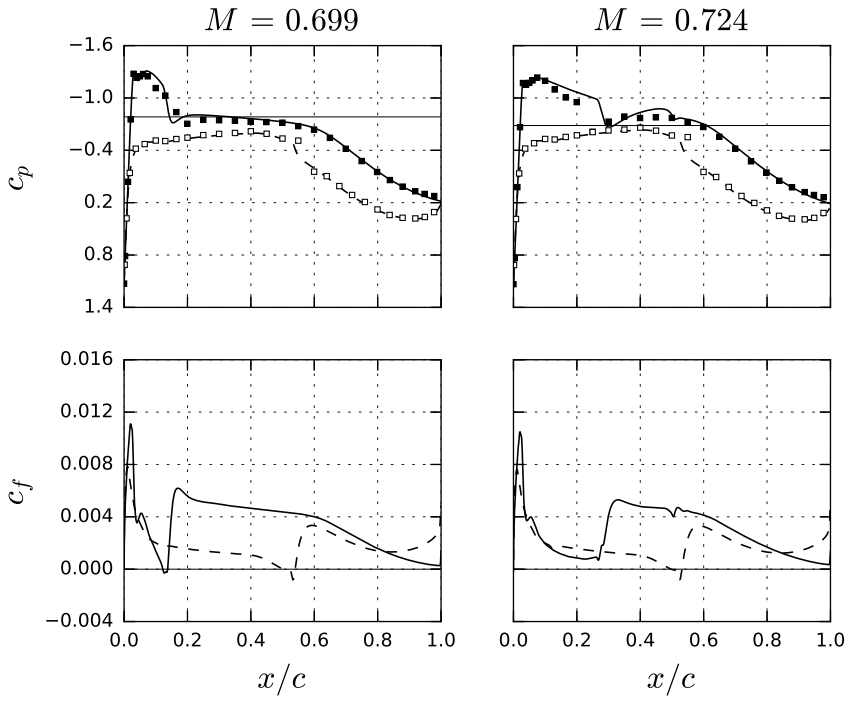

Figure 5.18: NLR 7301: Pressure and skin friction coefficients: $M = 0.699$ and $M = 0.724$

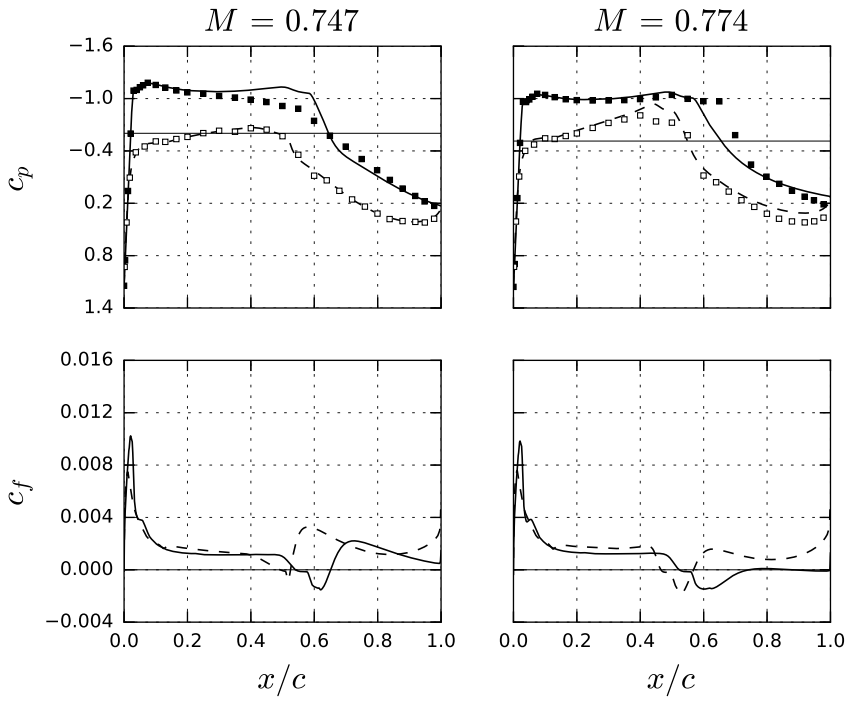

Figure 5.19: NLR 7301: Pressure and skin friction coefficients: $M = 0.747$ and $M = 0.774$

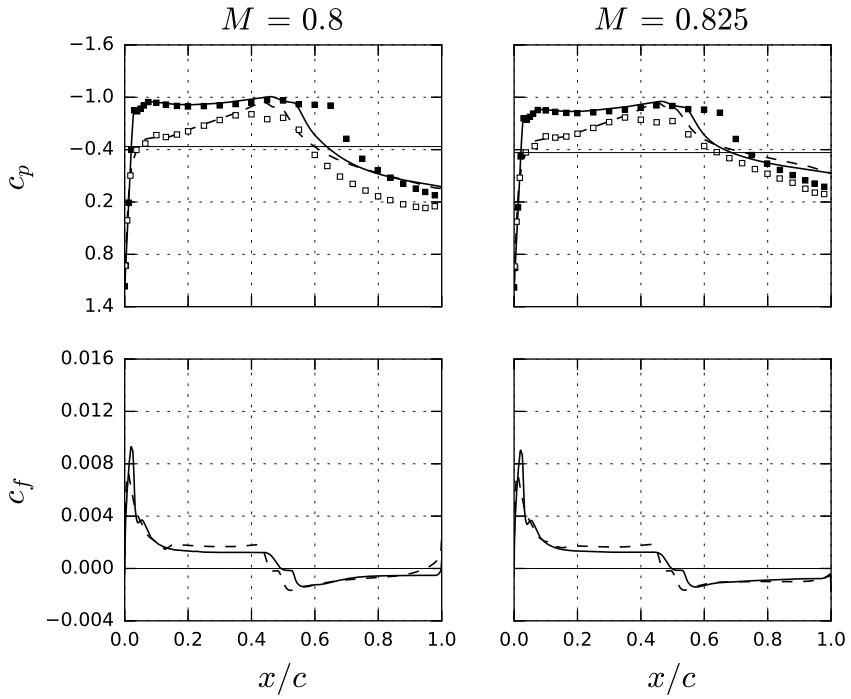

Figure 5.20: NLR 7301: Pressure and skin friction coefficients: $M = 0.8$ and $M = 0.825$

Angle of Attack Sweep

Zwaaneveld (1979) presents an angle of attack variation at a constant transonic Mach number. At $M = 0.748$ the nominal angle of attack α_n is changed from $-4°$ to $4°$. The Reynolds number for all cases is $Re = 2.2 \cdot 10^6$ and the turbulence level is $\tau = 0.158$ %. The CFD computations are performed at an angle of attack that gives the same or a similar suction distribution at the leading edge on the upper surface. Table 5.6 lists the angles of attack and the Mach numbers for each test case.

Table 5.6: NLR 7301: Angle of attack sweep

α_n / deg	α_{corr} / deg	α_{CFD} / deg	M
-4	-3.8001	-4	0.748
-2	-2.0731	-1.9	0.748
-1	-1.2861	-0.8	0.747
0	-0.3574	-0.35	0.748
0.95	0.2749	0.6	0.747
2	1.1403	1.75	0.748
4	2.9834	3.75	0.748

Figure 5.21 depicts the experimental and computed transition position (Zwaaneveld 1979, Fig. 4.7, p. A4-16)[2]. Figures 5.22 to 5.25 depict the computed pressure and skin friction coefficients and the experimental results. The full lines indicate the results from the CFD computations and the full symbols the measurements from Zwaaneveld (1979) for the upper airfoil surface. The dashed line and open symbols indicate the lower surface. The critical pressure coefficient for $M = 0.748$ is $c_{p,crit} = -0.598$ ($M = 0.747$, $c_{p,crit} = -0.6$).

Figure 5.22: The computation for $\alpha_n = -4°$ gives a shock-induced laminar separation on the lower surface. The boundary layer stays separated up to the trailing edge. In the case of the experiment, Zwaaneveld (1979) does not give any information if the flow is fully separated downstream of the shock. On the upper surface, the laminar separation is connected to a weak shock in the computation. The experimental data indicate a larger separation. For $\alpha_n = -2°$, the transition model predicts the size of the laminar separation on the upper and lower surface too small. The agreement between CFD and experimental results is reasonable for $\alpha_n = -2°$.

[2]These angles of attack do not correspond to the nominal angles of attack given for the α sweep.

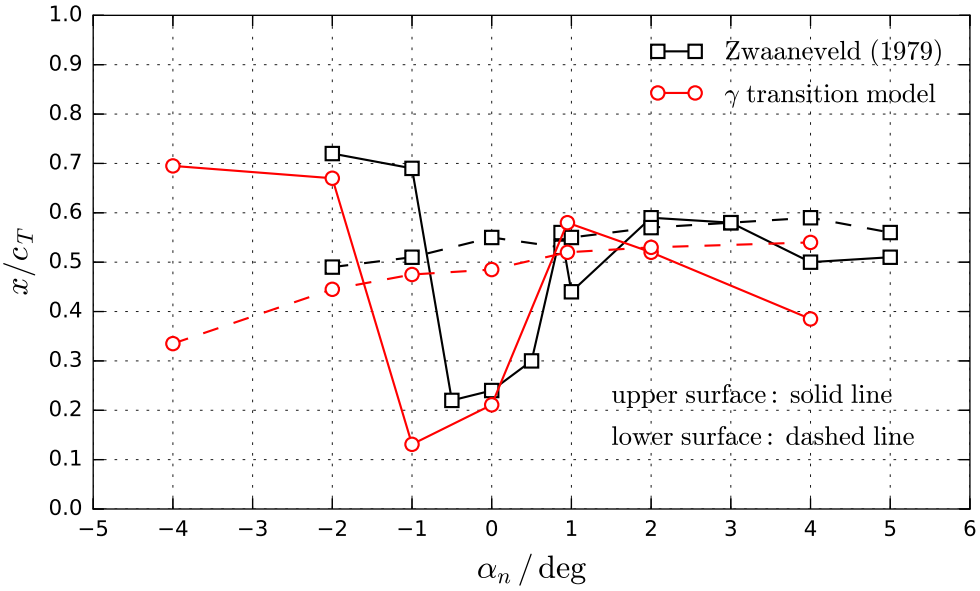

Figure 5.21: NLR 7301: Transition locations for the angle of attack variation

Figure 5.23: The experimental transition position on the upper surface at $\alpha_n = -1°$ is in the aft section of the airfoil. At $\alpha_n \approx -0.75°$ the transition position is unstable and moves towards the leading edge for increasing angles of attack (Zwaaneveld 1979). In the computation, the transition position has already moved to the leading edge at $\alpha_n = -1°$. For $\alpha_n = 0°$ the CFD model predicts a first shock close to the leading edge, which is not present in the experiment. The flow on the lower surface is well predicted.

Figure 5.24: The overall agreement for $\alpha_n = 0.95°$ is good. The shock at $x/c \approx 0.6$ is too strong and the size of the separation bubble is too large in the computation. On the lower surface, the separation bubble is too small compared to the experimental data. At $\alpha_n = 2°$ the boundary layer separates at mid-chord in the CFD computation and in the experiment. The predicted size of the separation bubble and the reattachment behavior of the flow differ from the experiment.

Figure 5.25: At $\alpha_n = 4°$ the boundary layer separates too far upstream in the computation. The predicted flow is detached up to the trailing edge downstream of the shock. There is no information on the experimental trailing edge flow. The flow on the lower side of the airfoil is probably fully attached in the experiment. The CFD model predicts a small laminar separation.

The transition behavior given by the γ transition model is qualitatively similar to the experimental results. For boundary layer flows with large separations, there is no exact way to determine the end of the transition region. This increases the uncertainties in the comparison of experimental results with CFD computations. Transonic boundary layer flows with large

separations require a further calibration of the transition model and the underlying turbulence model to give an appropriate turbulence production.

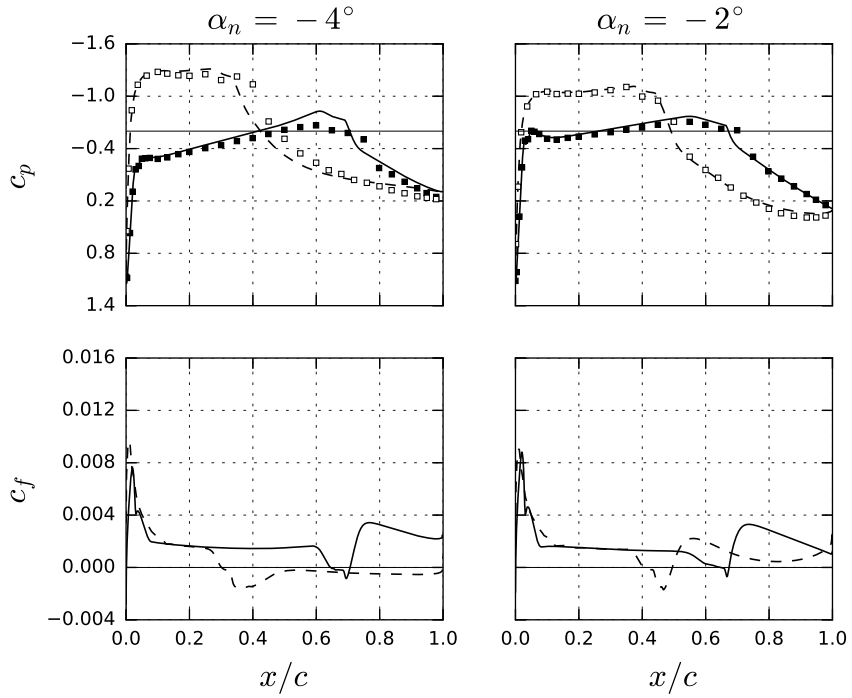

Figure 5.22: NLR 7301: Pressure and skin friction coefficients: $\alpha_n = -4°$ and $-2°$

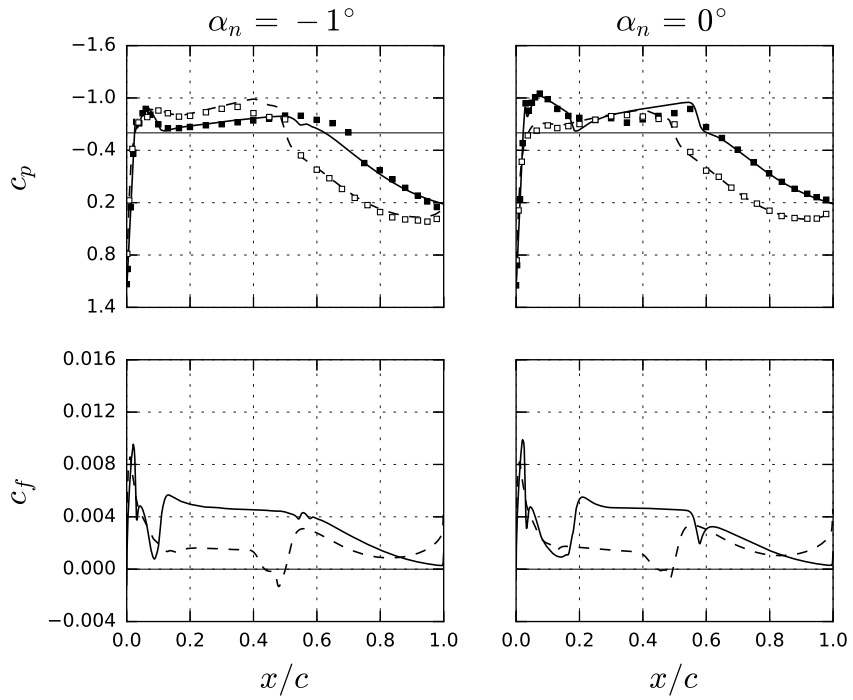

Figure 5.23: NLR 7301: Pressure and skin friction coefficients: $\alpha_n = -1^\circ$ and 0°

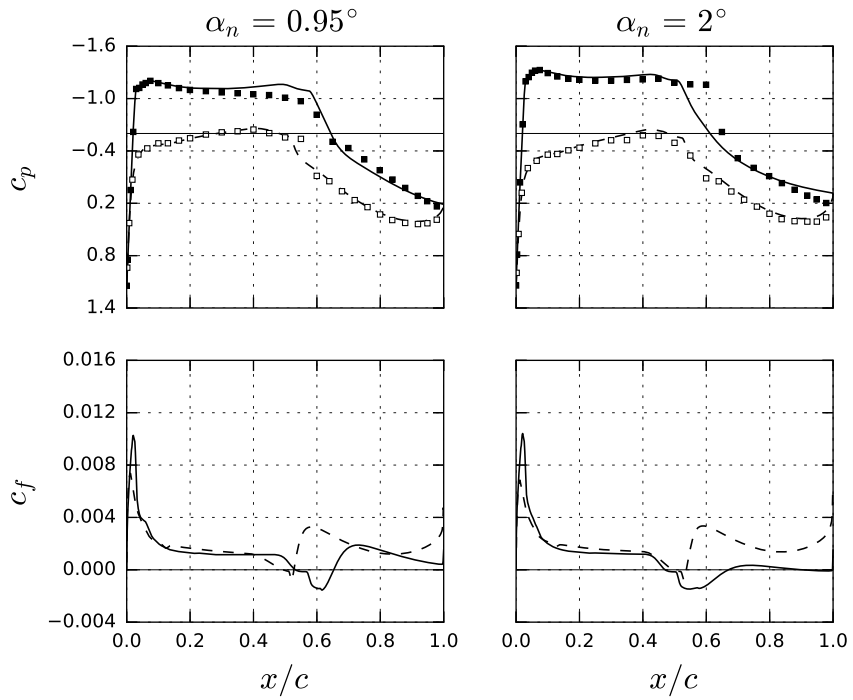

Figure 5.24: NLR 7301: Pressure and skin friction coefficients: $\alpha_n = 0.95^\circ$ and 2°

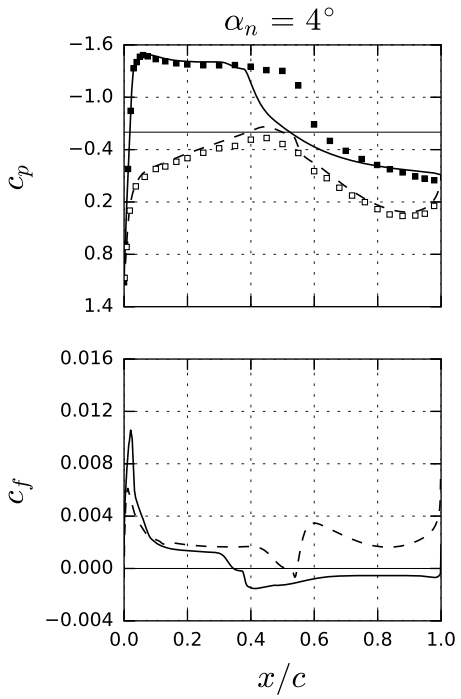

Figure 5.25: NLR 7301: Pressure and skin friction coefficients: $\alpha_n = 4°$

5.2.2 NACA 65(215)-114

The technical report by Braslow and Visconti (1948) contains experimental results for low Mach number flows at Reynolds numbers up to $Re = 60 \cdot 10^6$ with free boundary layer transition on a NACA $65_{215} - 114$ airfoil. The airfoil is depicted in Fig. 5.26. The test is conducted in the Langley two-dimensional low-turbulence pressure tunnel. The basic design idea for this airfoil is described by Abbott et al. (1945). The identification number gives the main aerodynamic characteristics of the airfoil (Abbott et al. 1945): A NACA 6 series laminar airfoil with a minimum pressure location at 50 % chord length and a maximum thickness of $t/c = 14$ %. The design lift coefficient is $c_{l,\,design} = 0.1$. For $c_l = c_{l,\,design} \pm 0.215$ a favorable pressure gradient exists on the upper and lower airfoil surface.

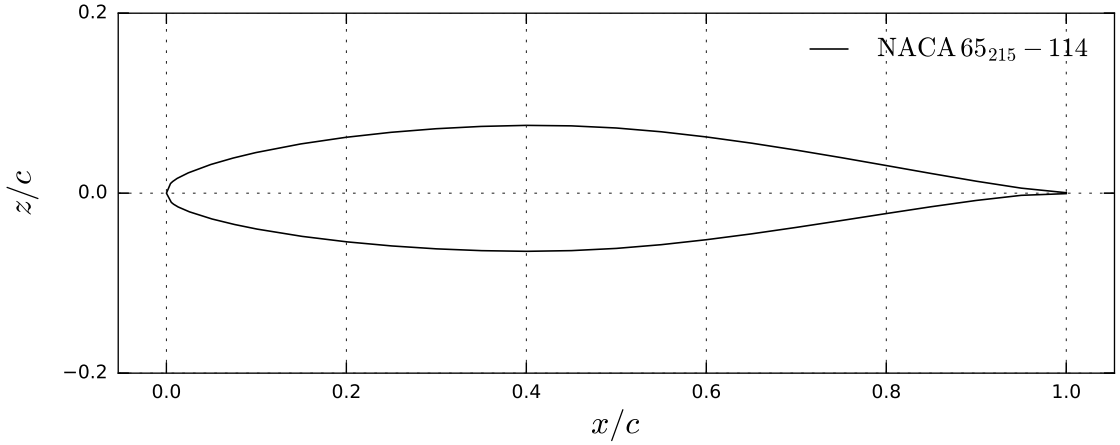

Figure 5.26: NACA $65_{215} - 114$: Geometry

Von Doenhoff and Abott (1947) present information on the turbulence level of the Langley two-dimensional low-turbulence pressure tunnel. The results of Braslow and Visconti (1948) are used by Granville (1953) to give a correlation for boundary layer transition in favorable pressure gradient flows.

Braslow and Visconti (1948) present transition locations for a variation of Reynolds number at a constant lift coefficient of $c_l = 0.14$. The short technical note only states, that "*it was possible to maintain the tunnel Mach number below 0.2 for the complete range of Reynolds number investigated*" (Braslow and Visconti 1948, p.4). Therefore, the exact Mach number is not known and set to $M = 0.2$ in the computation. The angle of attack is set to give a lift coefficient of $c_l = 0.14$.

Table 5.7 presents the data given by Braslow and Visconti (1948) and by von Doenhoff and Abott (1947). Table 5.8 lists the CFD results. The transition location is defined as the local maximum in the c_f distribution downstream of the transition onset. Braslow and Visconti

Table 5.7: NACA $65_{215} - 114$: Data presented by Braslow and Visconti (1948) and by von Doenhoff and Abott (1947)

$Re\,/10^6$	τ / %	$x/c_{T,\,up}$	$x/c_{T,\,low}$
20	0.03	0.46	0.495
30	0.05	0.375	0.43
40	0.08	0.32	0.36
50	0.16	0.275	0.28

Table 5.8: NACA $65_{215} - 114$: Results for turbulence levels given by von Doenhoff and Abott (1947)

$Re\,/10^6$	τ / %	c_l	α / deg	$x/c_{T,\,up}$	$x/c_{T,\,low}$
20	0.03	0.1399	0.365	0.524	0.536
30	0.05	0.1398	0.38	0.386	0.473
40	0.08	0.14	0.39	0.263	0.32
50	0.16	0.14	0.5	0.165	0.217

(1948) use a multitube pressure probe to obtain the airfoil pressure distribution. A pressure parameter is defined to determine the transition location. The parameter remains constant for a laminar boundary layer flow and increases for a transitional flow. There is no information on the transition zone length in the experiment.

The flow at $Re = 30 \cdot 10^6$ is used to calibrate the model. Therefore, the transition location is in good agreement with the experimental data. The agreement for the other Reynolds numbers is lower. Figure 5.27 depicts the transition location given by Braslow and Visconti (1948) and the CFD results. For Reynolds numbers above $Re = 30 \cdot 10^6$ and with increasing turbulence level, the transition position is predicted too far upstream by the γ transition model. For $Re = 20 \cdot 10^6$, the transition location is predicted too far downstream.

Table 5.9 presents the effect of the turbulence level compared to the combined effect of the turbulence level and the pressure gradient on the transition onset. The value of K_t is evaluated on the upper surface at the first intermittency increase. The increase in the turbulence level gives a decrease in $Re_{\theta t} = f(\tau)$. The transition location shifts upstream into a region with a stronger favorable pressure gradient as the Reynolds number increases. Therefore, K_t increases

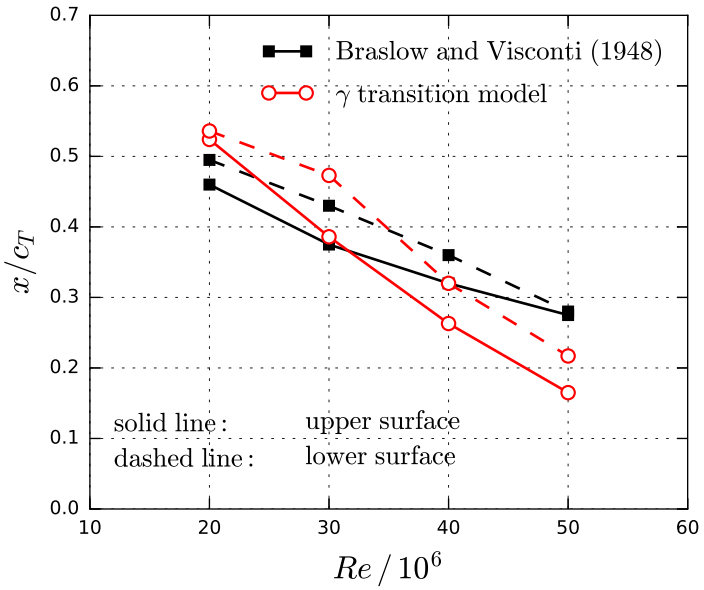

Figure 5.27: NACA $65_{215} - 114$: Transition locations from Braslow and Visconti (1948) and from the γ transition model

Table 5.9: NACA $65_{215} - 114$: Effect of turbulence level and K_t on $Re_{\theta t}$

$Re\,/10^6$	K_t	$Re_{\theta t}\,(\tau,\,K_t)\,/Re_{\theta t}\,(\tau)$	$Re_{\theta t}\,(\tau)$	$Re_{\theta t}\,(\tau,\,K_t)$
20	0.0151	1.04	1665	1732
30	0.0963	1.25	1379	1724
40	0.1538	1.38	1164	1606
50	0.2852	1.63	911	1485

with the Reynolds number, which has a stabilizing effect on the boundary layer. Overall, the stabilizing effect of K_t is canceled out by the turbulence increase.

Braslow and Visconti (1948) state, that "*the turbulence level of the tunnel is only a few hundredths of 1 percent*" (Braslow and Visconti 1948, p. 3). This is not in accordance with the data presented by von Doenhoff and Abott (1947). To account for these discrepancies, a second set of computations is performed for a turbulence level of $\tau = 0.05$ % for all Reynolds numbers.

Table 5.10 presents the flow conditions and transition locations for this set of CFD computations. Figure 5.28 depicts the transition locations compared to the data from Braslow and Visconti (1948). Except for $Re = 20 \cdot 10^6$, the transition location on the upper surface is

Table 5.10: NACA $65_{215} - 114$: Results for $\tau = 0.05$ %

$Re\,/10^6$	τ / %	c_l	α / deg	$x/c_{T,\,up}$	$x/c_{T,\,low}$
20	0.05	0.1401	0.37	0.498	0.511
30	0.05	0.1398	0.38	0.386	0.473
40	0.05	0.1403	0.385	0.322	0.391
50	0.05	0.1403	0.385	0.281	0.341

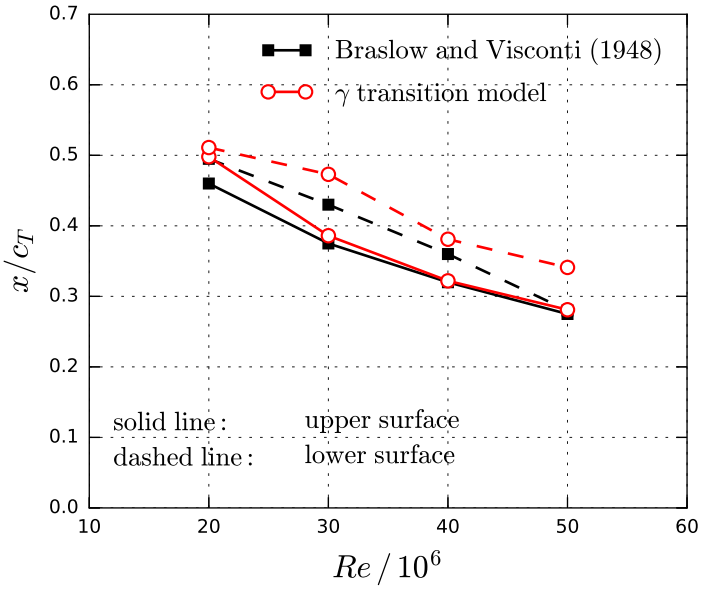

Figure 5.28: NACA $65_{215} - 114$: Transition locations from Braslow and Visconti (1948) and from the γ transition model for $\tau = 0.05$ %

met. Equation 4.28 for $Re_{\theta t}$ gives a strong variation in the low turbulence regime. A further improvement of the transition model requires detailed data on the exact turbulence level for each Reynolds number.

5.2.3 NLF(1)-0414F

McGhee et al. (1984b) present wind tunnel results for the NLF(1)-0414F airfoil for Reynolds numbers up to $Re = 10 \cdot 10^6$ at low to moderate Mach numbers $M = 0.05$ ... 0.4. The report contains aerodynamic coefficients c_l, c_d, and c_m and pressure distributions for various angle of attack sweeps. The aerodynamic coefficients are given in terms of corrected values. No wind tunnel correction is included for the pressure coefficients.

The NLF(1)-0414F is designed for a lift coefficient of $c_l = 0.4$ ... 0.45 at a Reynolds number of $Re = 10 \cdot 10^6$ and Mach numbers $M \leq 0.4$. The boundary layer flow on the upper side of the airfoil is accelerated up to $x/c \approx 0.7$ to allow a large extent of natural laminar flow. The leading edge is a compromise between a sharp nose for a wide laminar drag bucket and a blunt nose for better $c_{l,\,max}$ performance (McGhee et al. 1984b). The airfoil is depicted in Fig. 5.29.

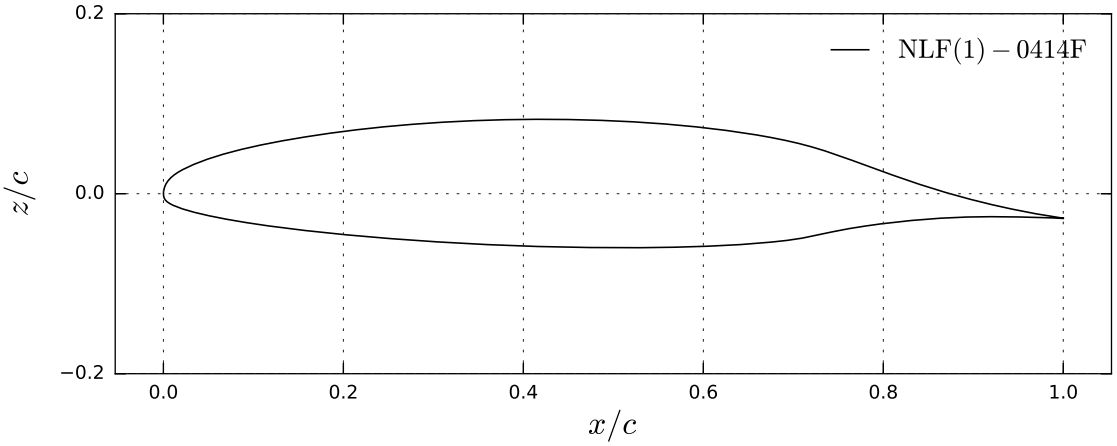

Figure 5.29: NLF(1)-0414F: Geometry

The experiment is conducted in the Langley Low-Turbulence Pressure Tunnel. McGhee et al. (1984b) state that the turbulence level is less than $\tau = 0.08$ % for unit Reynolds numbers below $6 \cdot 10^6$ 1/ft. The highest chord Reynolds number of $Re = 10 \cdot 10^6$ in the experiment results in a unit Reynolds number of $3.3 \cdot 10^6$ 1/ft. Additional information on the turbulence level is given by McGhee et al. (1984a). The turbulence level depends on the Reynolds and Mach number. Certain combinations of Re and M result in turbulence levels $\tau > 0.08$ % (McGhee et al. 1984a). Because of the uncertainties in the exact turbulence level, all computations with the γ and γ-Re_θ transition model are performed for $\tau = 0.08$ %.

Table 5.11 lists the Reynolds and Mach number for each experimental run. Each run contains an angle of attack variation. The lowest and highest angles of attack are given in Tab. 5.11. Most important for the validation of the γ transition model are the runs with a high Reynolds and a moderate Mach number (13, 15, and 28). Although the flow for these cases is

not transonic, it is a valuable test case for high Reynolds numbers.

Table 5.11: NLF(1)-0414F: Test case data from McGhee et al. (1984b)

Run	$Re\,/\,10^6$	M	$\alpha_{start}\,/\,\mathrm{deg}$	$\alpha_{end}\,/\,\mathrm{deg}$
3, 4, 6	10.0	0.12	−3.99	7.16
7	8.1	0.09	−2.98	8.23
8, 9	6.1	0.07	−4.02	6.24
10	4.4	0.05	−4.07	5.01
11, 12	3.0	0.07	−4.0	4.17
13	10.0	0.3	−4.06	8.3
15	9.5	0.4	−3.04	6.26
28	10.0	0.23	−3.0	6.32

For comparison, the aerodynamic coefficients c_l and c_d are taken from the report. McGhee et al. (1984b) use low-speed wind-tunnel corrections to give corrected values for the aerodynamic coefficients. The corrections are based on the measured coefficients at each angle of attack, e.g. $c_{l,\,corr} = f(c_l,\, c_d)$.

Figure 5.30 depicts the corrected lift and drag coefficients from McGhee et al. (1984b) and the CFD results. The overall agreement for the γ model is good as the extent of the laminar drag bucket is predicted correctly. In addition, the minimum drag coefficient is in good agreement for most cases. The lower limit of the drag bucket is in better agreement than the upper limit. Test cases with a sharp drag bucket limit (e.g. Run 10) are predicted correctly as well as cases with a smoother transition movement (e.g. Run 28). Two angles of attack from Run 15 are used for the calibration of the γ transition model. Therefore, Run 15 has to be excluded as a validation test case. Both angles of attack are given by full red symbols in Fig. 5.30.

For high angles of attack, the lift coefficient agrees reasonably well, but there are strong deviations in the drag coefficient. McGhee et al. (1984b) state that the drag rise for high angles of attack is caused by turbulent trailing edge separations. In the case of the CFD computations, the boundary layer does not separate or separations are limited to small portions of the chord length.

The γ-Re_θ transition model gives no laminar drag bucket for the high Reynolds number flows. For Run 10 and the combined Run 11, 12, a laminar drag bucket is predicted, but the agreement at the drag bucket limit is better for the γ transition model.

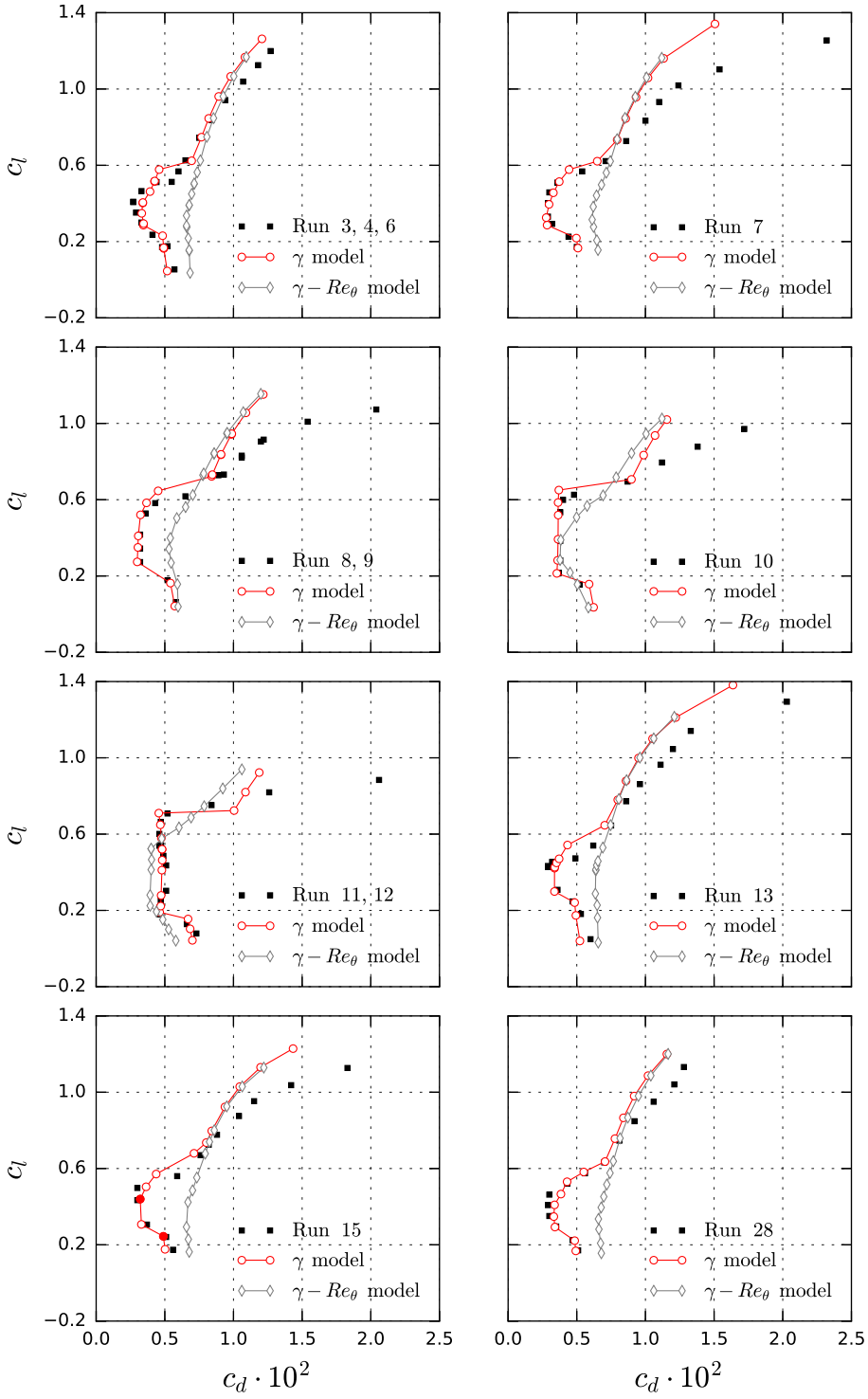

Figure 5.30: NLF(1)-0414F: Drag curves

5.2.4 NLF(2)-0415M

In the DLR project ALLEGRA, a wind tunnel model for a test campaign in the Cryogenic Wind Tunnel in Cologne (DNW-KKK) is developed. The airfoil is based on the NLF(2)-0415 and will be named NLF(2)-0415M. The airfoil is modified to reduce the aerodynamic moment. This is achieved by a modification of the aft section of the lower surface. The airfoil geometry of the NLF(2)-0415M is provided by DLR AS-HGK. The NLF(2)-0415 and the modified NLF(2)-0415M are depicted in Fig. 5.31.

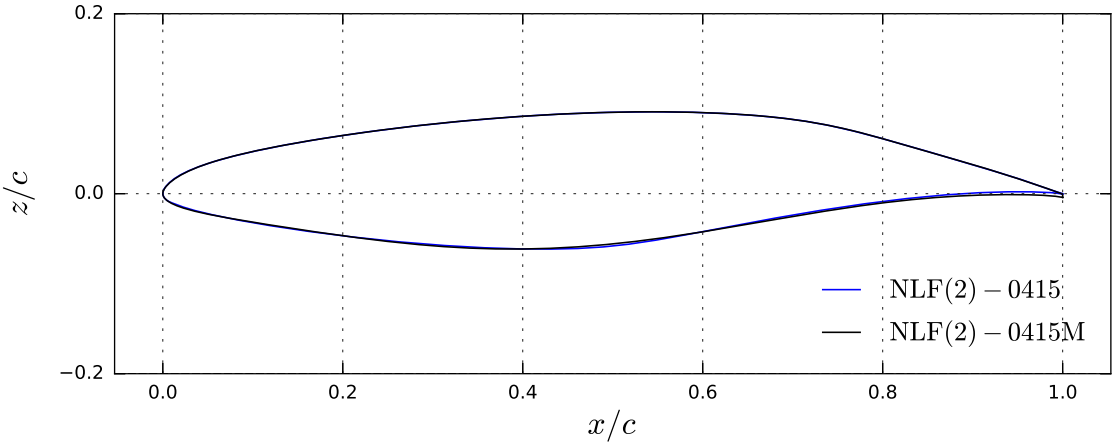

Figure 5.31: NLF(2)-0415M: Geometry

The NLF(2)-0415 is a laminar airfoil for a commuter aircraft (Somers and Horstmann 1985). The design point is the sea-level climb condition at $Re = 18 \cdot 10^6$, $M = 0.38$, and a section lift coefficient of $c_l = 0.38$. The laminar drag bucket ranges from $c_l \approx 0.1$ ... 0.5. The transition position inside the laminar drag bucket is given at $x/c = 0.7$ on the upper surface and at $x/c = 0.5$ on the lower surface. The desired low section drag over a large lift coefficient range results in a sharp drag bucket limit with a fast movement of the transition position (Somers and Horstmann 1985, p. 3).

Computations for the NLF(2)-0415M are performed at $Re = 15 \cdot 10^6$, $M = 0.38$ for a fully turbulent and transitional flow. For the fully turbulent computations, the SST k-ω turbulence model is used. The γ transition model, the γ-Re_θ transition model, and the e^N method are used for the transitional computations. The turbulence level is set to $\tau = 0.1$ %. In the case of the e^N method, a critical N factor for Tollmien-Schlichting transition $N_{TS} = 9$ is chosen. Both values correspond to disturbance environments found in modern wind tunnels. An angle of attack sweep $\alpha = -4°$ ... $4°$ is computed that covers the laminar drag bucket. The results are presented in Fig. 5.32.

The results from the γ-Re_θ transition model differ strongly from the other transition pre-

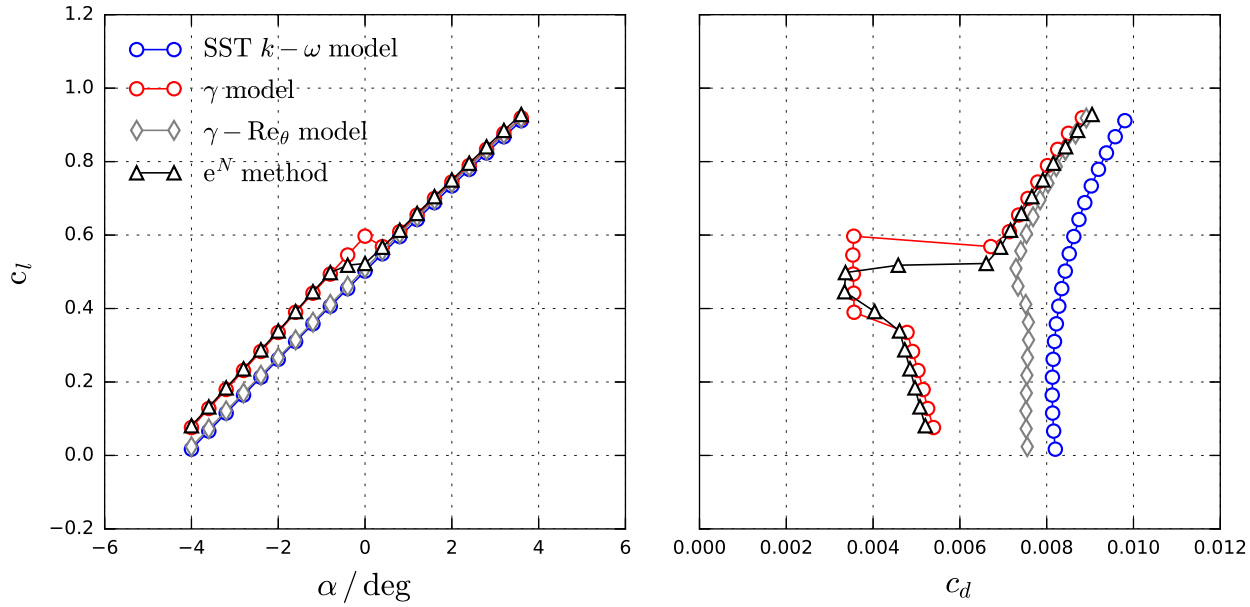

Figure 5.32: NLF(2)-0415M: Lift and drag curves

diction methods. The γ-Re_θ model does not give a laminar drag bucket. The lift coefficients are almost identical to the fully turbulent results and the drag benefit is small. The γ model predicts a drag bucket that is wider than for the e^N method and the upper drag bucket limit is sharper with a negative $\Delta c_l/\Delta\alpha$. The predicted coefficients outside the drag bucket agree for both methods. The e^N method does not give a steady solution for $\alpha = -0.4°$ as the transition position is unstable.

Figure 5.33 depicts the pressure and friction coefficients for the SST k-ω turbulence model and the γ-Re_θ transition model. The pressure distributions are almost identical for both flow types. For $\alpha = -3.2°$ and $-1.2°$, transition on the upper surface is predicted in a favorable pressure gradient region, which is unlikely for the given disturbance environment. In the case of $\alpha = -3.2°$, transition on the lower surface of the airfoil is caused by the suction peak and the γ-Re_θ model gives a reasonable result. For $\alpha = -1.2°$, the model gives an implausible transition position in a favorable pressure gradient region on the lower surface.

The e^N method and the γ transition model give the same transition behavior for the angels of attack depicted in Fig. 5.34. In the case of the e^N method, the transition position is slightly downstream and a small laminar separation bubble exists on the upper side of the airfoil. The differences are most likely caused by the fact that the definition of the disturbance environment is different for both methods. Although simple correlations exist, there is no exact translation of a N factor into a turbulence level.

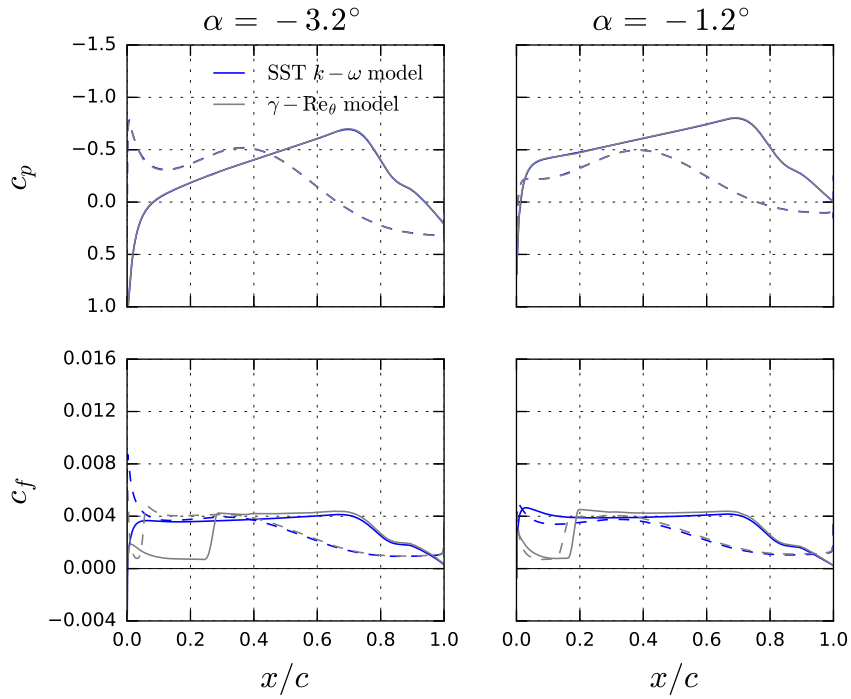

Figure 5.33: NLF(2)-0415M: Pressure and skin friction coefficients for the SST k-ω turbulence model and the γ-Re_θ transition model

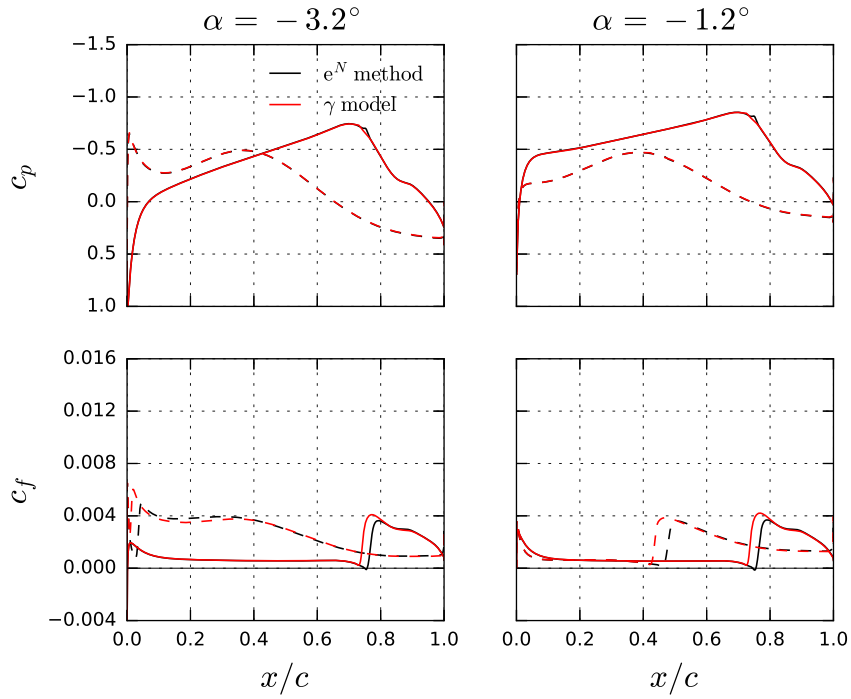

Figure 5.34: NLF(2)-0415M: Pressure and skin friction coefficients for the e^N method and the γ transition model

5.2.5 Grid Dependency: Airfoil

This section presents the effect of grid density on the NLR 7301 calibration test case at $M = 0.299$. Four different grids are tested with different chord wise grid spacings. The first cell height is not changed and gives a maximum y^+ value below 1. Table 5.12 presents the grids with the approximate number of points along one airfoil surface p, the number of points in one symmetry plane n, and the fraction of cell length to chord length $\Delta x/c$. The grid at the leading and trailing edge is slightly finer than the value given by $\Delta x/c$.

Table 5.12: NLR 7301: Grid dependency

	p	n	$n^{-1/2} \cdot 10^3$	$\Delta x/c$
very coarse	125	66 036	3.891	0.008
coarse	250	124 683	2.832	0.004
medium	500	195 425	2.262	0.002
fine	1000	350 463	1.689	0.001

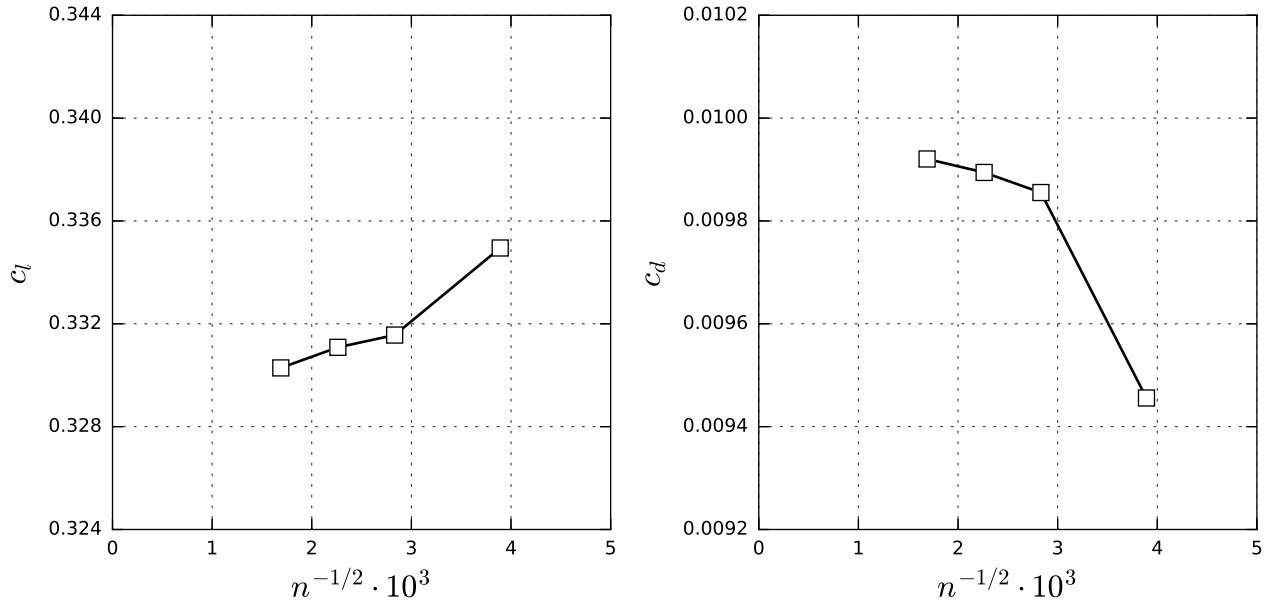

Figure 5.35: NLR 7301: Grid dependency

Figure 5.35 depicts the lift and drag coefficients for the different grids. The coarse grid is sufficient to compute the calibration test case. On the very coarse grid, the smaller grid density

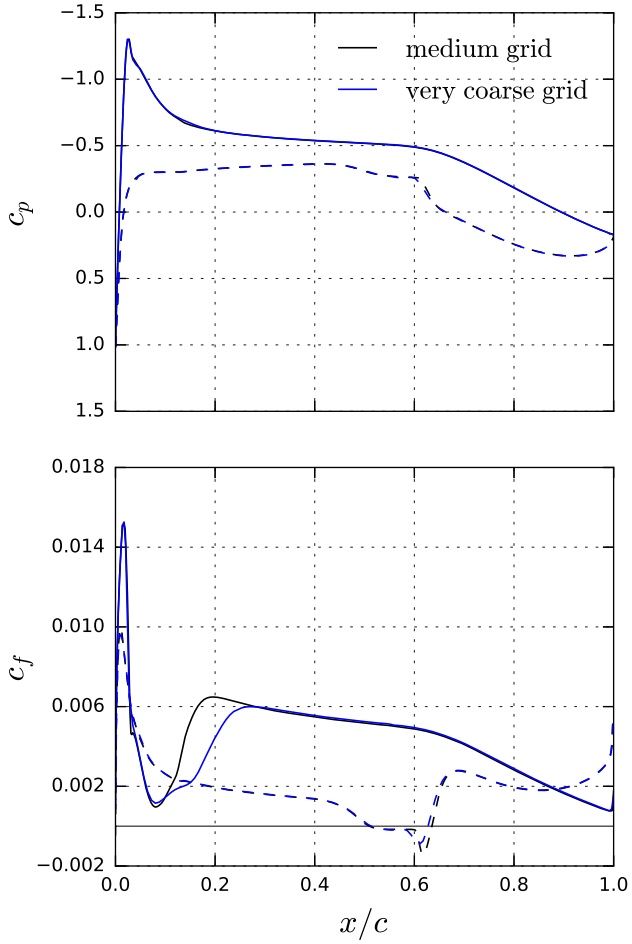

Figure 5.36: NLR 7301: Pressure and skin friction coefficient distribution for the medium and very coarse grid at $M = 0.299$

gives a smaller intermittency increase resulting in a larger transition region, which is depicted in Fig. 5.36. The transition location moves from the suction peak towards the trailing edge as the intermittency increase at the suction peak is not captured correctly. For flows that show a strong dependency on local effects, like a strong suction peak, a grid dependence study has to be performed to capture a grid independent intermittency production.

5.3 Steady Wing Test Case

The geometry considered is the forward-swept wing of the ALLEGRA design. The geometry is given by the jig-shape of the ALLEGRA-S FEM model (Klimmek 2014). The natural laminar flow wing has a leading edge sweep angle of $|\Lambda_{LE}| = 17°$ with a mean aerodynamic chord of $c_{mac} = 4.062$ m and a half-span of $b/2 = 17.95$ m. Computations are performed for $Re = 25{\cdot}10^6$, $\alpha = 2°$, and $M = 0.78$ with the γ-Re_θ transition model, the γ transition model, the TAU transition module (e^N method, LILO, SST k-ω model), and the SST k-ω turbulence model.

The critical N factors are given by $N_{TS} = 11$ for Tollmien-Schlichting transition and $N_{CF} = 10$ for crossflow transition (Seitz et al. 2011). For the correlation model computations, a turbulence level of $\tau = 0.05$ % is used. The critical N_{TS} value and the turbulence level describe low disturbance environments found in free flight.

The boundary layer grid contains 400 grid points in chord direction, 250 grid points in span direction, and 100 prism layers with a growth ratio of 1.1 and $y^+_{max} < 1$. In total, the grid contains $23 \cdot 10^6$ grid points. In the case of the e^N method, 38 streamlines along the wing span are used in the TAU transition prediction module. The streamlines are distributed approximately equidistant in span direction. The first streamline is given at about $y = -1$ m. For positions closer to the symmetry plane, the TAU transition module is not able to trace the streamline.

Figure 5.37 depicts the skin friction coefficient distribution on the upper and lower side of the ALLEGRA-S wing for the different transition prediction methods. The transition mechanism is Tollmien-Schlichting transition for all streamlines investigated with the TAU transition module. Therefore, a direct comparison of the different methods is possible. The e^N method and the γ transition model agree reasonably well on the suction and pressure side. The γ model gives a more upstream transition onset in the wing inboard region for both sides and on the wing tip on the suction side. The strong shock-induced separation at $y \approx -2$ m to -4.5 m is reproduced. The γ-Re_θ transition model is not able to reproduce the transition behavior of the e^N method on either side of the wing.

Table 5.13 gives the lift and drag coefficients for the different transition prediction methods and the fully turbulent computation. The e^N method and the γ transition model give similar results. The drag and lift benefit by a partly laminar flow compared to the fully turbulent solution is clearly given.

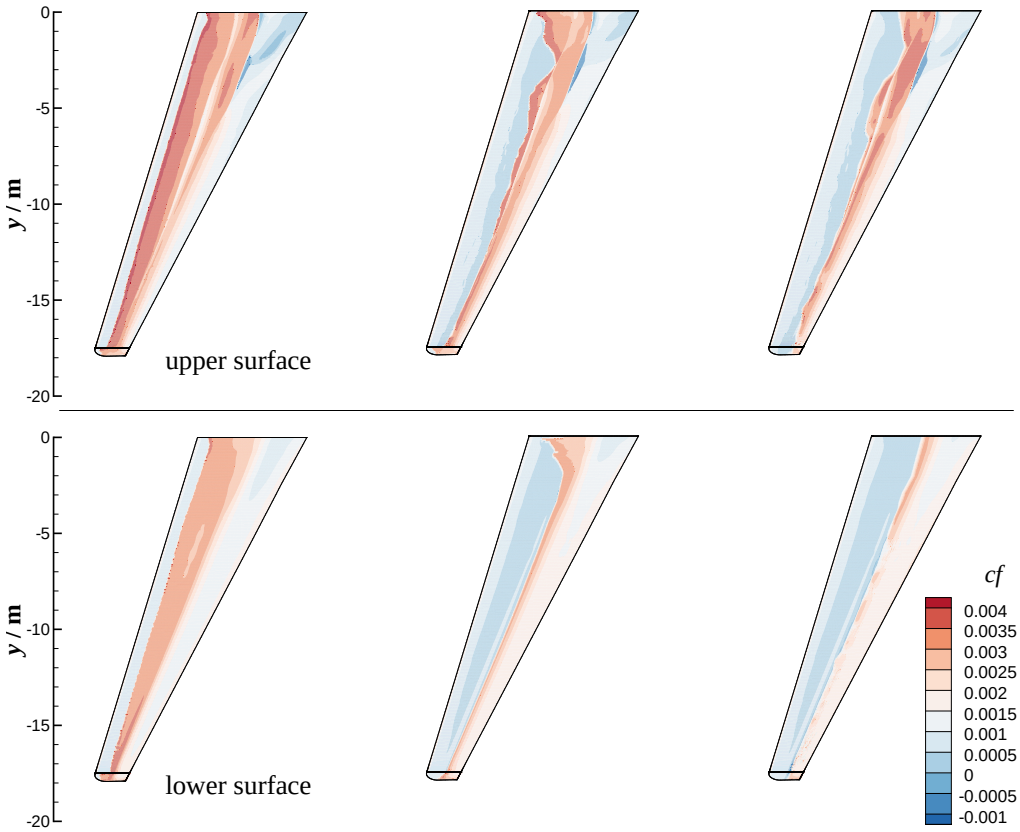

Figure 5.37: Skin friction coefficient distribution for the ALLEGRA-S wing geometry: γ-Re_θ transition model (left), γ transition model (middle) and e^N method (right)

Table 5.13: Lift and drag coefficients for the ALLEGRA-S wing

method	C_L	C_D
γ-Re_θ transition model	0.4997	0.01996
γ transition model	0.5458	0.01892
e^N method	0.5514	0.01867
SST k-ω model	0.4887	0.02029

5.4 Unsteady Airfoil Test Cases

5.4.1 CAST10-2: Unsteady Validation

CAST10-2: Test Case Description

The unsteady transition behavior of the γ transition model is investigated for the CAST10-2. The CAST10-2 is part of a family of airfoils designed for a transonic commercial transport aircraft. The design methodology is given by Stanewsky and Zimmer (1980). The design constraints for the CAST10-2 include a small pitching moment and a thick trailing edge to include a flap system (Stanewsky et al. 1984). The design point is given at $M = 0.76$, $\alpha = 0.2°$, and $c_l = 0.595$ (Stanewsky and Zimmer 1980). The section coordinates are documented by Dress et al. (1983).

In the given coordinate system, the trailing edge is located below the reference line. If a chord line from the leading to the trailing edge is defined, this line is 0.88° nose-up compared to the reference line (Mineck 1989). All results are computed in the reference coordinate system according to Dress et al. (1983). The CAST10-2 is depicted in Fig. 5.38.

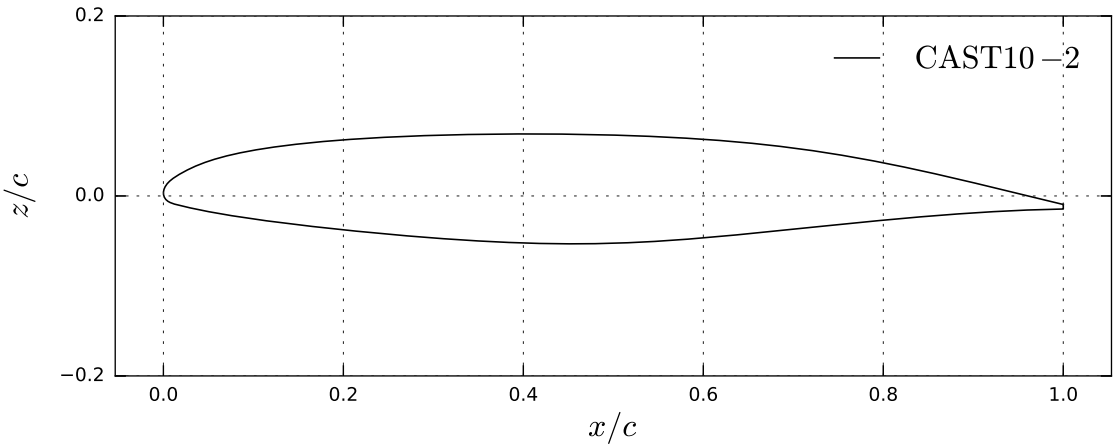

Figure 5.38: CAST10-2: Geometry

The unsteady aerodynamics of the CAST10-2 have been investigated in the Transonic Wind Tunnel Göttingen (DNW-TWG) (Mai and Hebler 2011; Hebler 2013; Hebler et al. 2013). The wind tunnel campaign ALF[3] 3 in the DLR project ALLEGRA[4] provides flow measurements at transonic Mach numbers and $Re = 2 \cdot 10^6$ for the CAST10-2. The measurements show nonlinearities in the lift curve caused by a strong movement of the transition location with

[3] Aeroelastik des Laminarflügels
[4] Aeroelastic stability and loads prediction for enhanced green aircraft

angle of attack. Forced pitch oscillations are used to investigate the unsteady aerodynamics with free boundary layer transition. The wind tunnel model is equipped with hot-film sensors to detect the boundary layer state, accelerometers to measure the pitch motion, and unsteady pressure sensors to determine the pressure distribution (Hebler et al. 2013).

The ALF 3 results for $M = 0.7$ and $Re = 2 \cdot 10^6$ are used to validate the unsteady transition behavior of the γ model. First, the steady lift curve is computed to evaluate any difference in the steady predictions. The results are compared to the experimental data in terms of lift, drag, and pressure coefficients. Second, a forced motion computation is used to evaluate the unsteady transition behavior at $k = 0.05$.

The turbulence level in the DNW-TWG depends amongst other parameters on the Mach number. For the 2011 turbulence measurement campaign, Meyer et al. (2012) report an increase of the turbulence level up to $M = 0.75$ for the adaptive wind tunnel section. Fehrs (2015) proposes a turbulence range of $\tau = 0.25$ % to 0.4 % based on the unfiltered and rigorously filtered energy spectral density of the velocity fluctuations for $M = 0.7$. In the computations with the γ transition model, a turbulence level of $\tau = 0.35$ % is used.

The computations are performed on a computational grid with a cell length of $\Delta x/c \approx 0.002$ and $y^+_{max} < 1$. The farfield is about 100 chord lengths away from the airfoil.

CAST10-2: Steady Results

Figure 5.39 depicts the lift and drag coefficients from the ALF 3 experiment (Hebler 2013) and from the computation with the γ transition model. The experimental lift coefficients are obtained from the integrated pressure measurements. In addition to the mean value of c_l, the standard deviation is indicated by the error bars. The investigated angles of attack are steady with only minor deviations from the time-averaged mean value. The experimental drag coefficients are based on wake measurements.

The computational results reproduce the lift curve with a certain offset in the angle of attack. The upper laminar drag bucket limit is given at slightly higher lift coefficients by the γ transition model. There is a reversal of the lift curve slope in the CFD computation, which is not found in the experimental data. The drag coefficients are matched reasonably well. The minimum drag inside the low drag range is predicted correctly as well as the behavior above the drag bucket limit.

The wind tunnel experiment is conducted in the closed circuit, adaptive test section of the DNW-TWG. The top and bottom walls of the wind tunnel are adapted to have a minor effect on the airfoil pressure distribution. No wind tunnel corrections exist for the DNW-TWG that account for circulation, blockage, or sidewall effects. In the computation, a farfield condition is

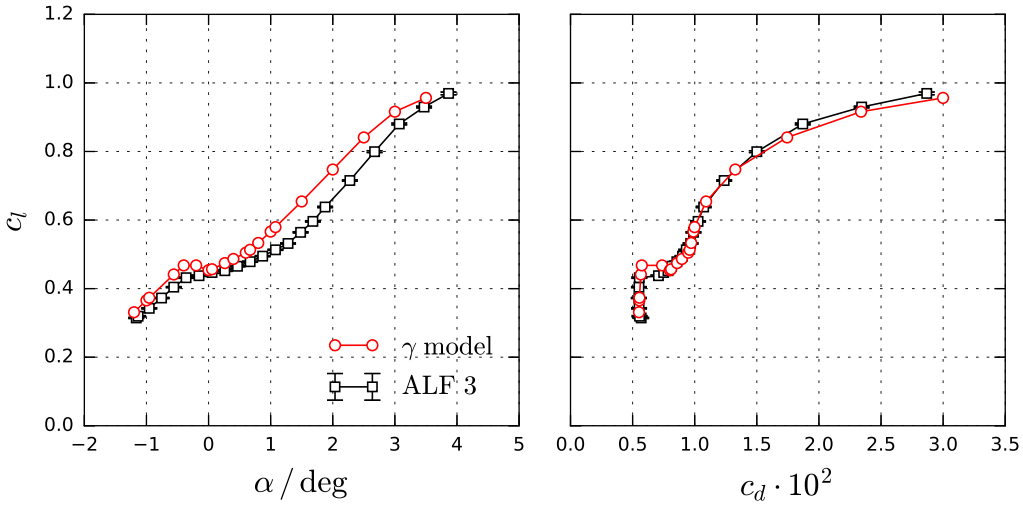

Figure 5.39: CAST10-2: Lift and drag curves

used. A slight buckling of the model downstream of $x/c = 0.5$ is given under loading (Hebler 2013). Although the model deformations are small, any difference in camber or the trailing edge influences the circulation over the airfoil. The model deformation is not included in the computation. Hebler et al. (2013) use a wind tunnel correction of $\Delta\alpha_{corr} = -0.3°$ and an additional Mach number correction of $\Delta M_{corr} = -0.01$ to reproduce the steady lift curve at $M = 0.75$ with MSES. A similar angle of attack correction would improve the lift coefficient results.

Figure 5.40 to 5.42 depict the pressure coefficient distributions for certain angles of attack along the lift curve. The dashed black line gives the critical pressure coefficient. In addition, the skin friction coefficient distributions are depicted for the γ transition model. Figure 5.40 depicts two angles of attack inside the laminar drag bucket. The laminar boundary layer separates on both sides of the airfoil. The γ transition model predicts a smaller separation bubble than indicated by the experimental pressure distribution for $\alpha = -0.955°$. The experimental pressure distribution for $\alpha = -0.56°$ is reproduced by the transition model.

Figure 5.41 depicts two angles of attack at the drag bucket limit in the range of the nonlinear lift increase. The transition location moves upstream for increasing angles of attack on the suction side of the airfoil. The CFD computation gives lower pressure coefficients downstream of the leading edge compared to the experimental data. The flow is transonic in this region. Downstream of the transition location, the pressure coefficient distribution is well predicted for both angles of attack.

Figure 5.42 depicts two angles of attack above the laminar drag bucket limit. The transonic flow region in the computation is terminated by a shock, which causes a shock induced sepa-

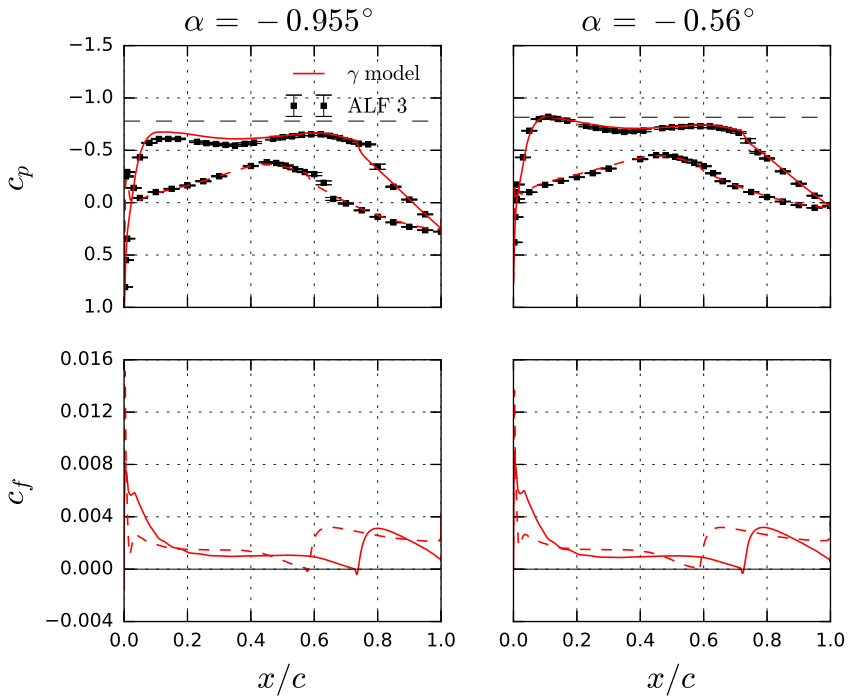

Figure 5.40: CAST10-2: Pressure and skin friction coefficients for $\alpha = -0.955°$ and $-0.56°$

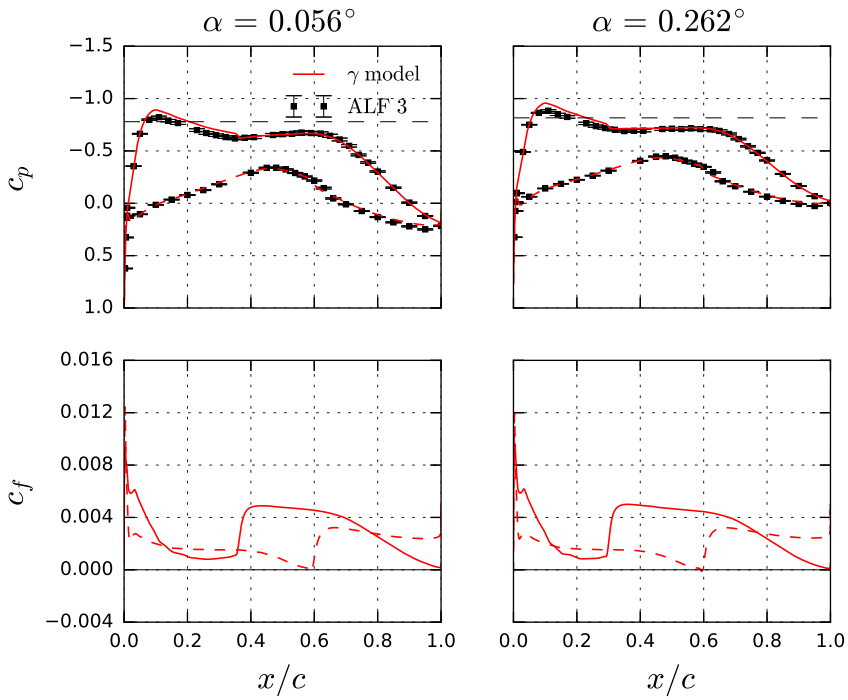

Figure 5.41: CAST10-2: Pressure and skin friction coefficients for $\alpha = 0.056°$ and $0.262°$

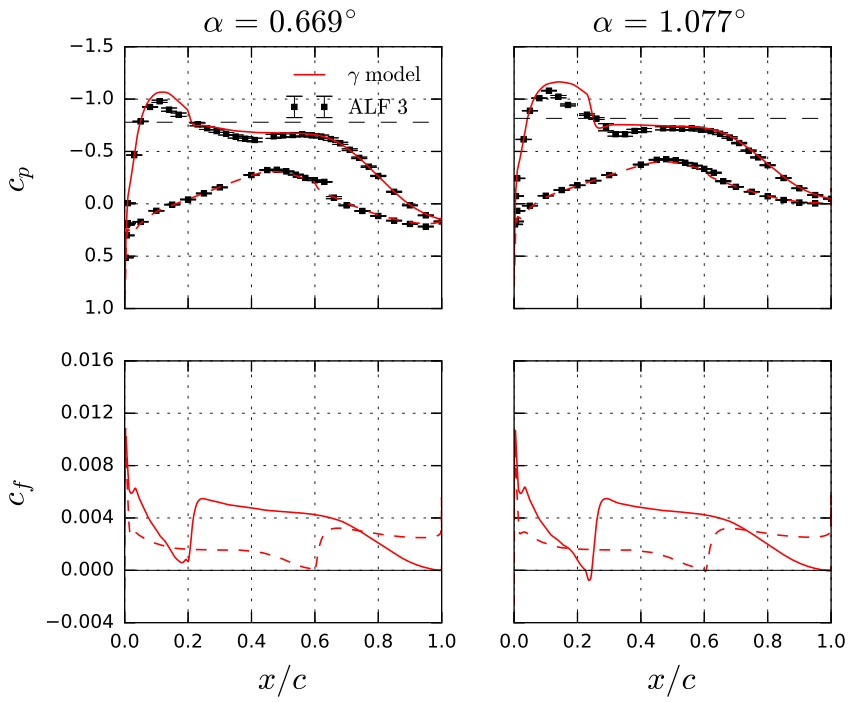

Figure 5.42: CAST10-2: Pressure and skin friction coefficients for $\alpha = 0.669°$ and $1.077°$

ration in the case of $\alpha = 1.077°$. Although there is a certain fluctuation in the experimental pressure coefficients at the predicted shock location, the experimental flow is shock free. For all angles of attack, the γ transition model predicts a separation bubble on the pressure side of the airfoil that is too small compared to the experimental data.

CAST10-2: Unsteady Results

The γ transition model is used to compute a harmonic pitch oscillation of the CAST10-2 at $M = 0.7$ for $\alpha_m = 0°$, $\widehat{\alpha} = 0.8°$, and $k = 0.05$. The mean angle of attack in the experiment is $\alpha_m = 0.034°$. Figure 5.43 depicts the unsteady lift coefficients given by the γ model and the phase averaged lift coefficients from the ALF 3 experiment. In the experiment, 128 data points are measured every period. The computational lift coefficients are depicted for a single period. For the unsteady computation, 5000 time steps per period with 1000 inner iterations (single grid) are used. The base flow at $\alpha = 0°$ is slightly unsteady in the computation. In addition to the unsteady lift coefficients, the steady lift curves are given by the open symbols on the left.

The experimental and CFD data show an unsteady lift response with nonlinear effects as the aerodynamic response includes higher harmonics. At maximum deflection in the linear lift curve region, there is little difference between the steady and the unsteady lift coefficients. The

laminar drag bucket limit shifts to higher angles of attack during the up-stroke and to lower angles of attack during down-stroke. The experimental data show a smooth variation of c_l as the transition location changes at the drag bucket limit. The γ transition model gives a more sudden change, especially during the down-stroke.

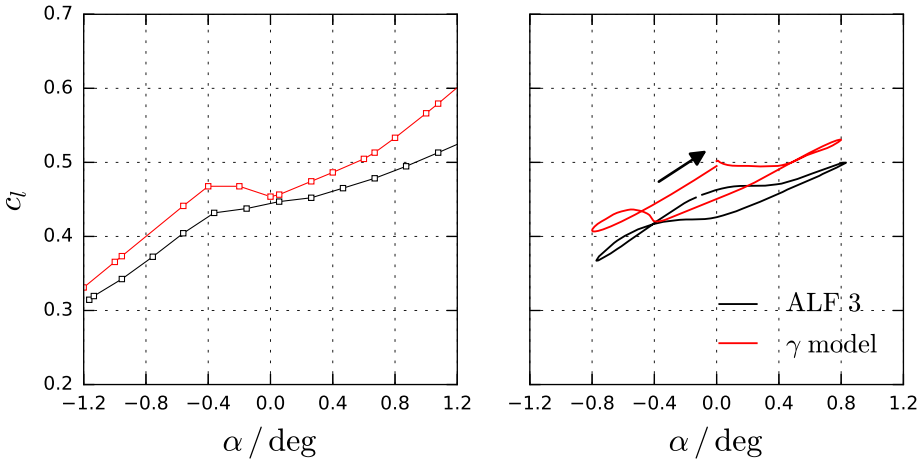

Figure 5.43: CAST10-2: Steady (left) and unsteady (right) lift coefficients for $\widehat{\alpha} = 0.8°$

Figure 5.44 depicts the transition location over one pitch period from the ALF 3 experiment and the CFD computation. The experimental data are read from Figure 209 given by Hebler (2013), which depicts the AC voltage signal for each hot-film sensor along the suction side of the CAST10-2 for one pitch period. Hebler (2013) differentiates between laminar regions, intermittent flow regions, separated boundary layer flow, and fully turbulent flow. The flow states are indicated in Fig. 5.44. In the range of $t/T \approx 0.35$ to 0.6, the actual boundary layer state is unidentified as the AC voltage signals do not give a laminar flow downstream of $x/c \approx 0.15$ up to the intermittent region.

The computational results are evaluated every 50 time steps based on the skin friction coefficient distribution. The strongest increase in c_f is detected and the downstream maximum in c_f is taken as the location, at which the fully turbulent boundary layer state is reached. In the following, this point is referred to as transition location. These locations are depicted by the red line in Fig. 5.44. In addition, any upstream laminar separation is identified by the zero-crossings (separation and reattachment) in the c_f distribution. The separation and reattachment locations are both indicated by circles. The unsteady transition behavior is captured by the γ transition model.

Based on the unsteady pressure data, large regions of separated flow are identified in the experiment for low angles of attack during up- and down-stroke (Hebler 2013). The boundary layer separation occurs at a lower angle of attack during down-stroke ($\alpha \approx -0.5°$) than the

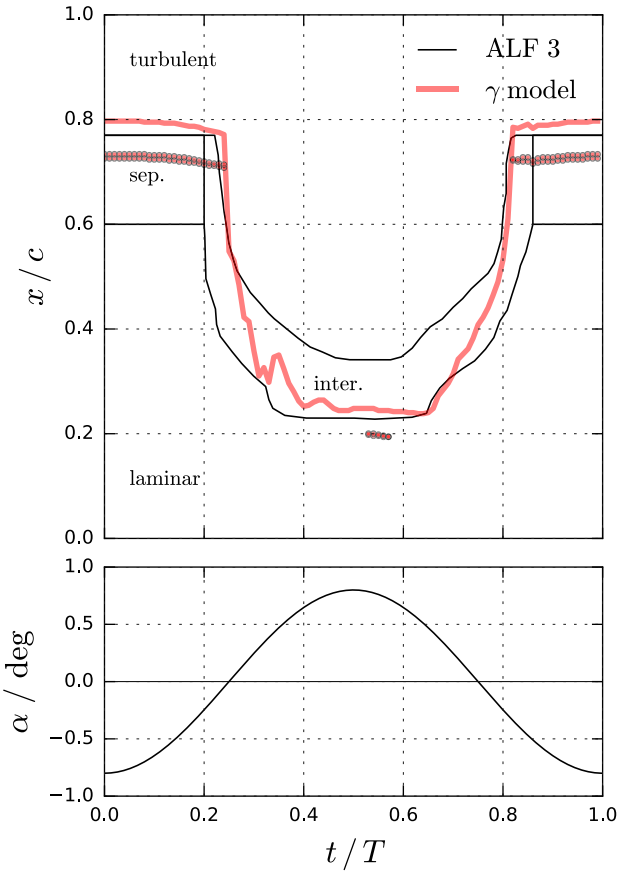

Figure 5.44: CAST10-2: Boundary layer state over one pitch period

reattachment during up-stroke ($\alpha \approx -0.25°$). This phase lag of the separation behavior is qualitatively reproduced by the γ transition model (down-stroke separation $\alpha \approx -0.25°$, up-stroke reattachment $\alpha \approx 0°$).

Similar to the experimental data, the predicted separation location does not show a large variation with angle of attack. However, separation occurs further downstream in the computation and the size of the separation bubble is small compared to the experimental data. Based on the evaluation procedure of the c_f data, there exists an offset between the reattachment point and the identified location of fully turbulent flow. One might argue that a reattachment in an adverse pressure gradient region requires a turbulent state and the transition location should be identified with the reattachment location. For consistency, the definition based on the maximum c_f value is kept.

For increasing angles of attack, the transition location in the experiment moves upstream. In addition, large intermittency regions are detected upstream of the fully turbulent boundary layer. The γ transition model shows a similar behavior, but the transition locations are not

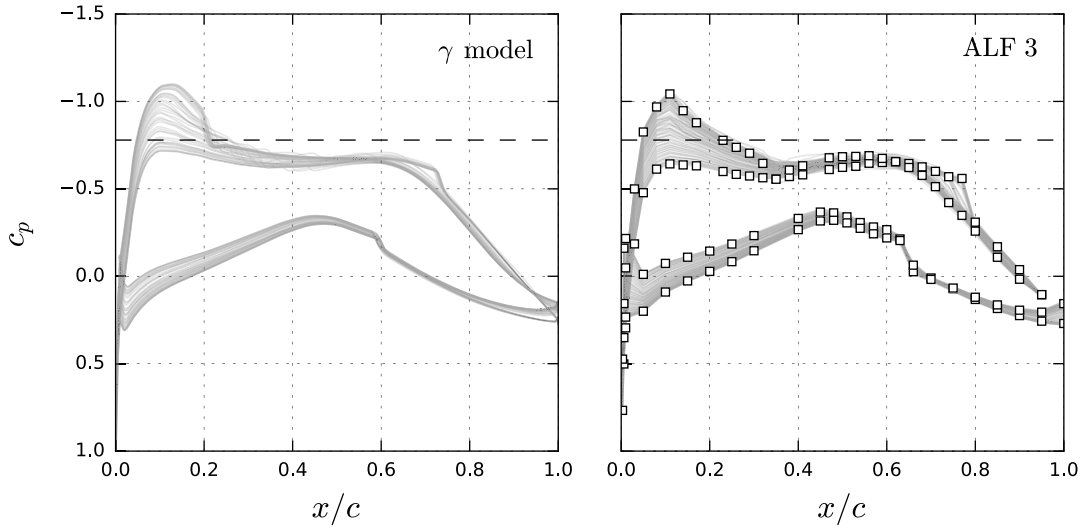

Figure 5.45: CAST10-2: Pressure coefficient distribution over one pitch period

as symmetric for the up- and down-stroke compared to the ALF 3 data. During up-stroke, there is a certain fluctuation in the transition location, which is not present for the down-stroke movement of the airfoil. In addition, there is a small shock induced separation close to the maximum deflection of the airfoil, which is not given in the experimental data.

The γ transition model predicts the fully turbulent flow too far upstream for high angles of attack. As the CFD results give a shock at these angles of attack, the transition location is connected to the shock location with the maximum c_f just downstream of the shock. The pressure coefficient distribution over one pitch period is depicted in Fig. 5.45. As seen in Fig. 5.45, the flow in the experiment is shock free over the pitch period, which gives a fully turbulent flow further downstream.

No attempt is made to assess the intermittency onset given by the γ transition model. As explained in Section 5.1, the intermittency variable γ is not suited to represent the physical intermittency in an experiment. Low values of γ downstream of the transition onset at $Re_{\theta t}$ do not alter the boundary layer flow necessarily. The intermittency onset in the computation does not represent the first intermittent boundary layer flow in the experiment.

CAST10-2: Summary

Aeroelastic considerations require valid aerodynamic models in a wide range of Mach and Reynolds numbers. The ALF 3 experimental data provide a test case for a high Mach number flow at a moderate Reynolds number. The validation approach based on farfield conditions results in an offset in the steady results compared to the experimental data, which would

require wind tunnel corrections for a further improvement. In addition, uncertainties in the turbulence level, model deformation, and wind tunnel effects aggravate the comparison between experimental data and computational results. Although the pressure coefficient distributions for single angles of attack are not matched exactly, the lift curve at the drag bucket limit, and to a larger degree the drag coefficients, match the experimental data reasonably well.

The unsteady aerodynamic lift response for a forced pitch motion from the experiment is reproduced by the γ transition model. The differences found in the steady pressure coefficient distribution are also present in the unsteady results. The basic transition behavior over the pitch period is reproduced by the model as the movement of the transition location for the up- and down-stroke is reproduced. However, large differences exist in the predicted separation behavior. The pressure measurements indicate large regions of separated flow. The γ transition model gives only minor separations. However, the CFD based detection of separated flow by c_f values is much more precise than a qualitative identification based on unsteady pressure sensors.

Flutter predictions require the determination of the frequency-depending aerodynamic loads for small excitation amplitudes. A final assessment of the γ transition model based on a single large amplitude test case is not possible as further computations in the high Mach and Reynolds number range are required.

5.4.2 NLF(2)-0415M: γ Model and e^N Method

The γ transition model is not an unsteady transition model similar to the unsteady method presented by Radespiel et al. (2007). The transition model does not include any explicit assumptions about the unsteady transition process. Besides this shortcoming, the γ transition model is applied to the unsteady base flow and the transport equation might provide some intrinsic unsteady behavior. To give some qualitative information on this unsteady behavior, the γ transition model is compared to the steady e^N method of the TAU transition module. Because there is a lack of validated unsteady transition methods, steady e^N methods are commonly used to predict unsteady aerodynamics with free boundary layer transition. The γ transition model is built to give similar results as the e^N method for Tollmien-Schlichting transition. For low reduced frequencies, both methods should give similar results once the steady state is similar.

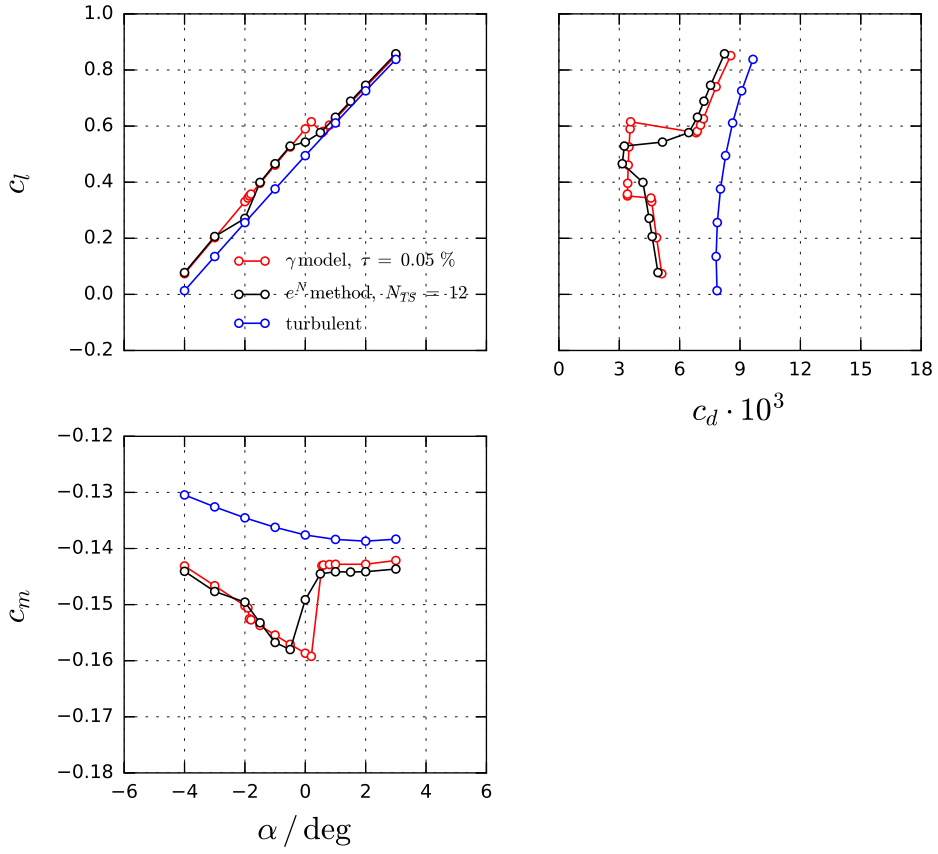

Figure 5.46: NLF(2)-0415M: Lift, drag, and moment curves predicted by the e^N method and γ model

The NLF(2)-0415M presented in Section 5.2.4 is considered for this unsteady test case at

$Re = 18 \cdot 10^6$ and $M = 0.38$. The lift curve is computed for a critical N factor $N_{TS} = 12$. The results are depicted in Fig. 5.46. The lower drag bucket limit for the e^N method is given at $\alpha = -2°$ to $-1.5°$. The TAU transition module (LILO) gives an oscillating transition location on the upper and lower surface of the airfoil in this angle of attack range. At $\alpha = 0°$ the transition location oscillates around $x/c = 0.5$ on the upper surface.

The TAU transition module gives a stable transition location for $\alpha = -1°$ inside the drag bucket. The pressure and skin friction coefficient distributions for this angle of attack predicted by the γ transition model and the e^N method are depicted in Fig. 5.47. The transition location is slightly further downstream for the e^N method. On the upper surface, the flow separates and a short laminar separation bubble is present in the case of the e^N method. The difference in the transition location has little effect on the lift coefficient.

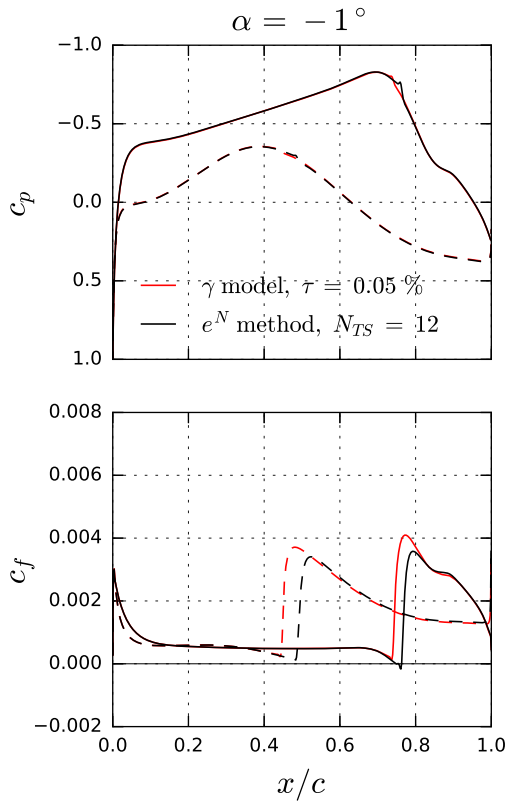

Figure 5.47: NLF(2)-0415M: Pressure and skin friction coefficient distribution at $\alpha = -1°$

Forced pitch motion computations at single frequencies for $k = 0.25$, 0.5, 0.75, and 1 are performed for both transition prediction methods. The reduced frequencies cover the relevant range for flutter calculations. The amplitude of the harmonic motion is given by $\hat{\alpha} = 1° \cdot 10^{-4}$ to obtain a linear lift response. Figure 5.48 depicts the magnitude and phase angle of the lift

coefficient derivative due to pitch $c_{l\alpha}$ for $\alpha_m = -1°$. The linear system identification results (pulse) are obtained for a maximum amplitude of $\hat{\alpha} = 1° \cdot 10^{-6}$. The single frequency results for both transition prediction methods meet the pulse results. The difference in the magnitude of $c_{l\alpha}$ given by the e^N method is vanishingly small compared to the γ transition model.

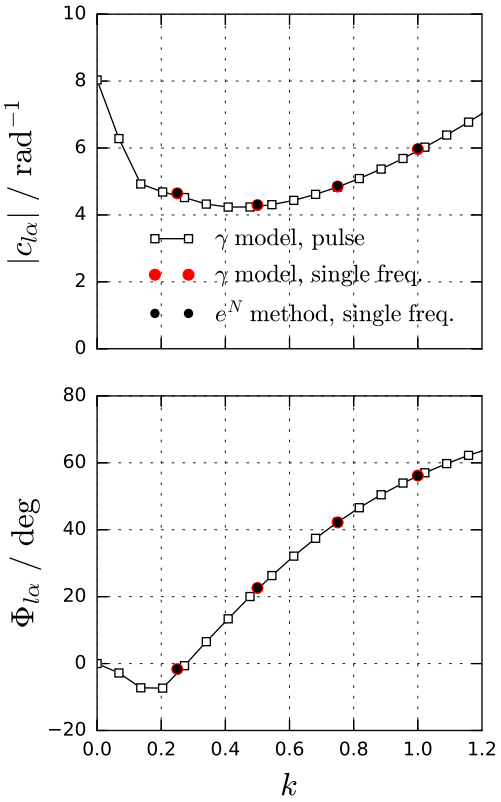

Figure 5.48: NLF(2)-0415M: Unsteady lift and moment given by the γ transition model and e^N method for $\alpha = -1°$

The e^N method gives no variation in the transition location over the pitch oscillations. In the TAU transition module, the transition location is tied to a single grid point. Once the critical N factor is reached, the turbulence production is activated downstream. The cell length of $\Delta x/c = 0.002$ is rather fine and the computational time increases significantly for a refined boundary layer grid, which could provide a better resolution of any transition location oscillation. In addition to the increase in computational time, a finer grid often results in no stable transition location at all, especially in the case of separation bubbles and shocks.

In the computation of a steady flow problem, the TAU transition module is called in a fixed interval of iterations up to a user-defined number of calls. For small transition location oscillations during the computation, a steady state and a well converged solution is often found for either transition location given in the last transition prediction step. The steady state

solution is used to initialize the unsteady computation and the transition location oscillation is most likely present in the unsteady flow as well. For aeroelastic considerations, small amplitude perturbations are used to determine the linear aerodynamic response of the system. Once the oscillation of the transition location is stronger than any disturbance introduced by the perturbation, the base flow unsteadiness renders the approach impossible because the unsteady aerodynamic response depends on the initial transition location.

The γ transition model can also encounter oscillations in the transition onset position. However, the blending given by the intermittency variable γ smoothens the transition behavior and allows the perturbation approach by pulse or single frequency excitations for a wider range of test cases.

5.4.3 NLF(2)-0415M: Laminar Airfoil

NLF(2)-0415M: Test Case Description

The NLF(2)-0415 is a laminar airfoil designed for medium-speed commuter aircrafts (Somers and Horstmann 1985). The aerodynamic and aeroelastic behavior of the modified airfoil NLF(2)-0415M is investigated at the design condition of the NLF(2)-0415. It is given by the sea-level climb condition at a Reynolds number of $Re = 18 \cdot 10^6$ and $M = 0.38$. The turbulence level is $\tau = 0.05$ % for this test case.

The steady lift curve is computed and some angles of attack are chosen for unsteady investigations. The flutter stability is evaluated based on the unsteady aerodynamic data. The structural model for the flutter analysis is partly adapted from Dietz et al. (2004). The non-dimensional structural parameters are listed in Tab. 5.14. A wing section with a chord length of $c = 0.5$ m, a mass of $m = 60$ kg, and a bending frequency of $f_h = 20$ Hz is assumed. The elastic axis is located at quarter-chord. There is no structural damping included.

The computations are performed on a computational grid with a cell length along the airfoil of $\Delta x/c \approx 0.002$ and $y^+_{max} < 1$. The farfield is about 100 chord lengths away from the airfoil. For the unsteady computations, the linear system identification approach (pulse) by Kaiser et al. (2015) is used for amplitudes of $\widehat{\alpha} = 1^\circ \cdot 10^{-5}$ to $1^\circ \cdot 10^{-6}$ and $\widehat{h} = 10^{-5}$ m to 10^{-6} m.

Table 5.14: Non-dimensional structural parameters from Dietz et al. (2004)

$x_\alpha = S_\alpha \,/\, (m\,c)$	$r_\alpha = \sqrt{I_\alpha \,/\, (m\,c^2)}$	ω_h/ω_α
0.042	0.1828	0.6991

NLF(2)-0415M: Steady Results

Figure 5.49 depicts the lift, drag, and quarter-chord moment coefficients for the transitional and fully turbulent flow. The turbulent lift increase is linear with angle of attack. The transitional flow shows a laminar drag bucket with a nonlinear lift increase at the upper drag bucket limit. No steady solution exists for $0.2^\circ < \alpha < 0.55^\circ$ at the upper limit. For the lower drag bucket limit, no unsteady flow conditions are found ($\Delta\alpha = 0.05^\circ$). The drag bucket limit is clearly found in the moment coefficient curve.

Figure 5.50 and 5.51 depict the pressure and skin friction coefficient distribution at the drag bucket limit. For comparison, the fully turbulent flow condition is given at $\alpha = -2^\circ$ for the lower limit and at $\alpha = 0^\circ$ for the upper limit. The critical pressure coefficient for $M = 0.38$

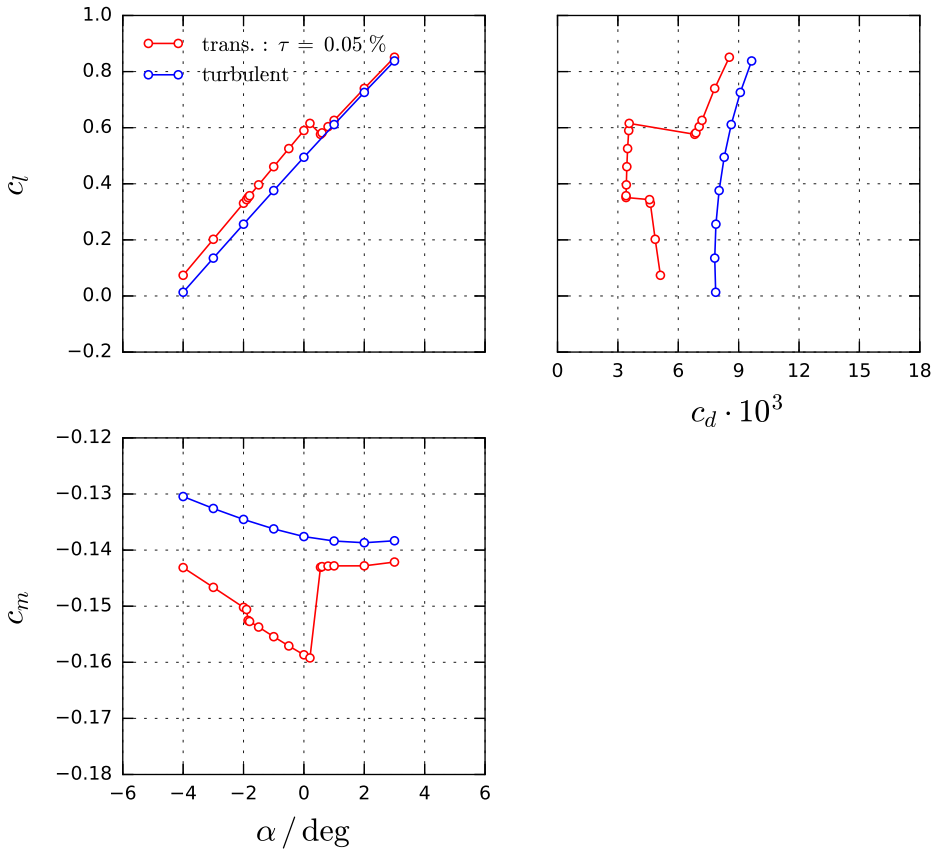

Figure 5.49: NLF(2)-0415M: Lift, drag, and moment curves

is $c_{p,\,crit} = -4.12$. The flow is subsonic for all angles of attack. The transition behavior on the pressure side determines the lower limit and the behavior on the suction side the upper drag bucket limit. A small change in the adverse pressure gradient at the leading edge gives a sudden change in the transition location. There is no stable transition location in-between the 70 % chord and the leading edge location on the suction surface. The effect of the laminar flow on the aerodynamic characteristic of the airfoil is strongest for the upper surface of the NLF(2)-0415M.

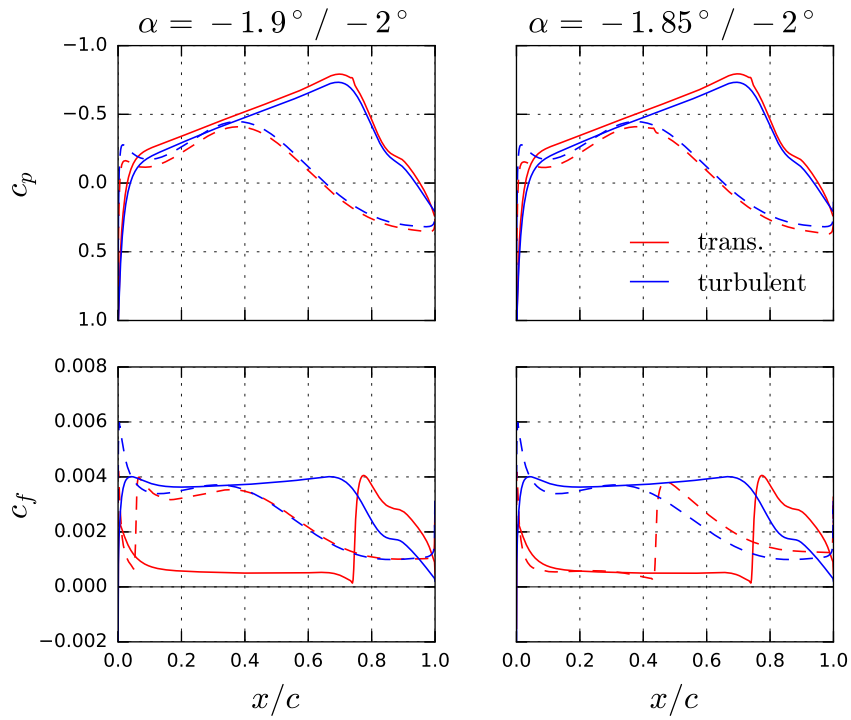

Figure 5.50: NLF(2)-0415M: Pressure and skin friction coefficient distribution at the lower drag bucket limit

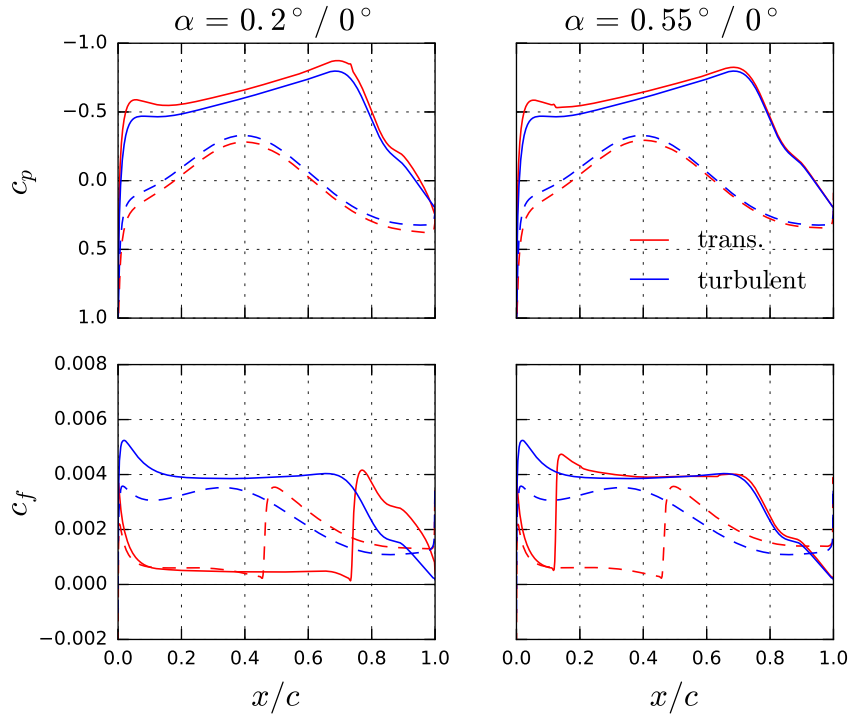

Figure 5.51: NLF(2)-0415M: Pressure and skin friction coefficient distribution at the upper drag bucket limit

NLF(2)-0415M: Unsteady Results

Figures 5.52 to 5.55 depict the unsteady results at the upper drag bucket limit. The transitional result at $\alpha_m = 0.2°$ inside the laminar drag bucket and at $\alpha_m = 0.55°$ outside the laminar drag bucket are compared to the fully turbulent results at $\alpha_m = 0°$.

The transitional unsteady lift coefficient derivative $c_{l\alpha}$ due to pitch is very similar to the fully turbulent derivative. There are only some minor differences in the phase between $k = 0.1$ and 0.3. The transitional lift coefficient derivative c_{lh} due to heave is almost identical to the turbulent derivative. In addition, there are only small differences in the transitional results as the drag bucket limit is crossed. As the lift curve slope is not changed inside and outside the laminar drag bucket, the unsteady aerodynamic behavior is hardly affected.

The unsteady transitional results for $c_{m\alpha}$ and c_{mh} resemble the turbulent results closely. The steady transitional moment coefficient curve runs parallel to the fully turbulent curve for $\alpha_m > 0.55°$. The steady results indicate a phase shift by $+180°$ at the drag bucket limit for the transitional flow, which is not found in the unsteady data. However, moving from $\alpha_m = 0.2°$ to 0.55°, the phase lag of $c_{m\alpha}$ and c_{mh} decreases as the moment curve slope changes (e.g. for $k = 0.1$ about $+80°$ for c_{mh}). This effect is more pronounced for the heave motion than for the pitch motion.

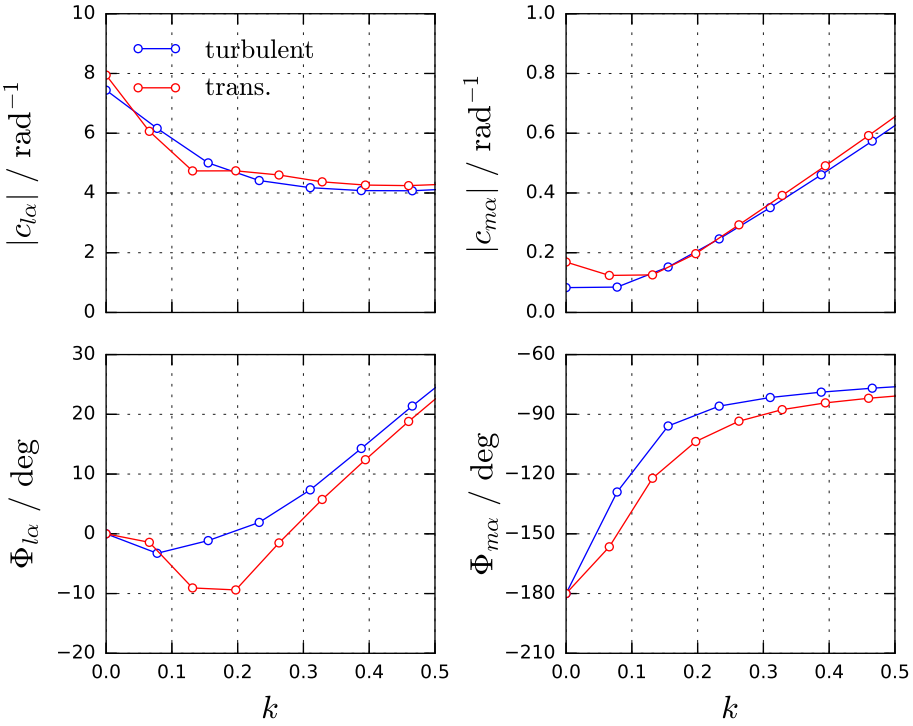

Figure 5.52: NLF(2)-0415M: Unsteady lift and moment for $\alpha_m = 0.2° \ / \ 0°$ due to pitch

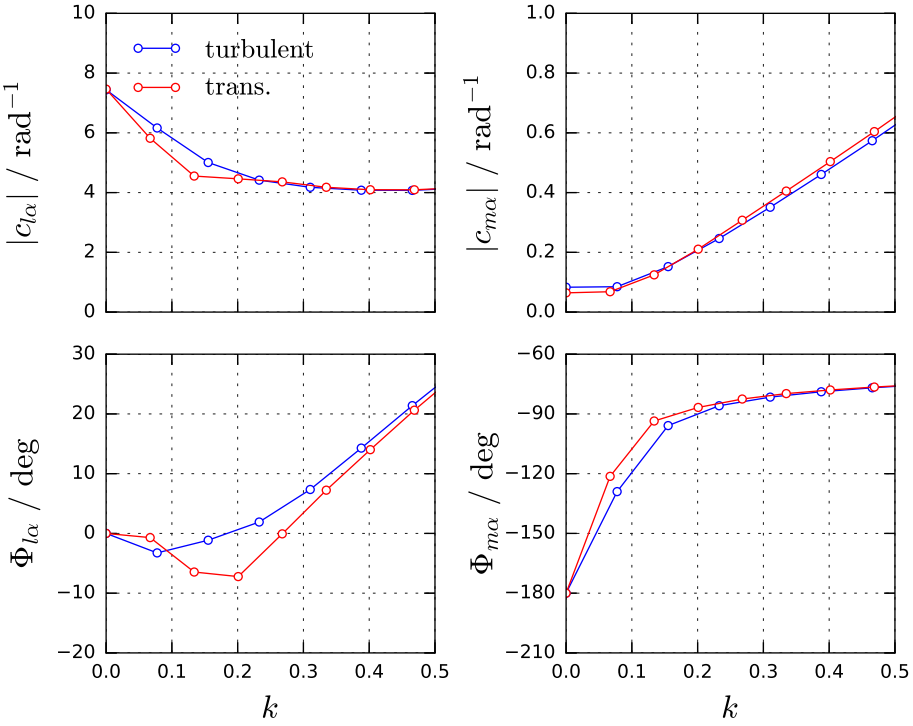

Figure 5.53: NLF(2)-0415M: Unsteady lift and moment for $\alpha_m = 0.55° \ / \ 0°$ due to pitch

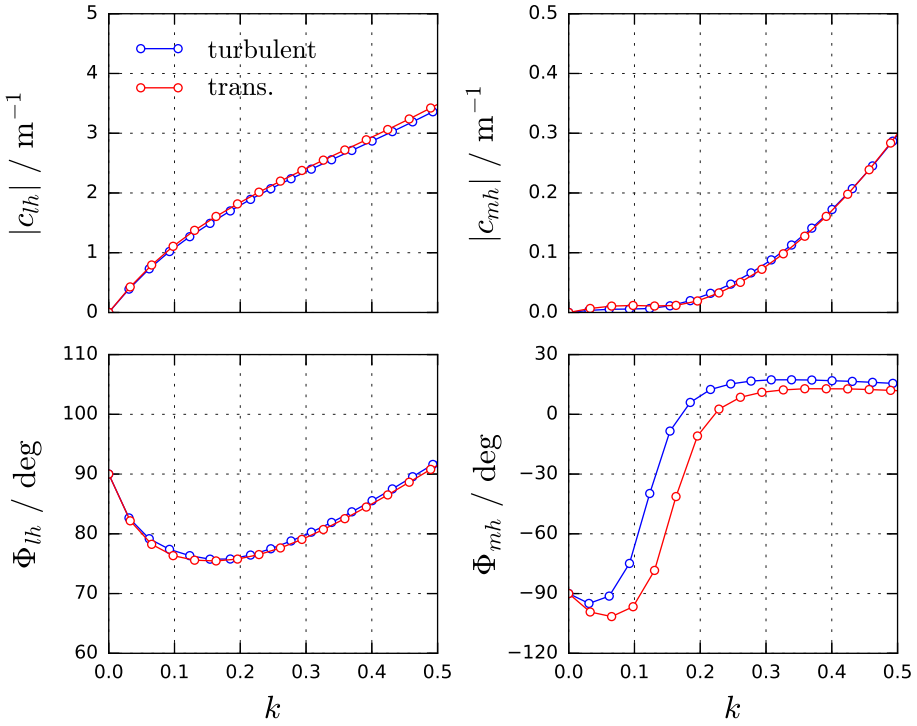

Figure 5.54: NLF(2)-0415M: Unsteady lift and moment for $\alpha_m = 0.2° \ / \ 0°$ due to heave

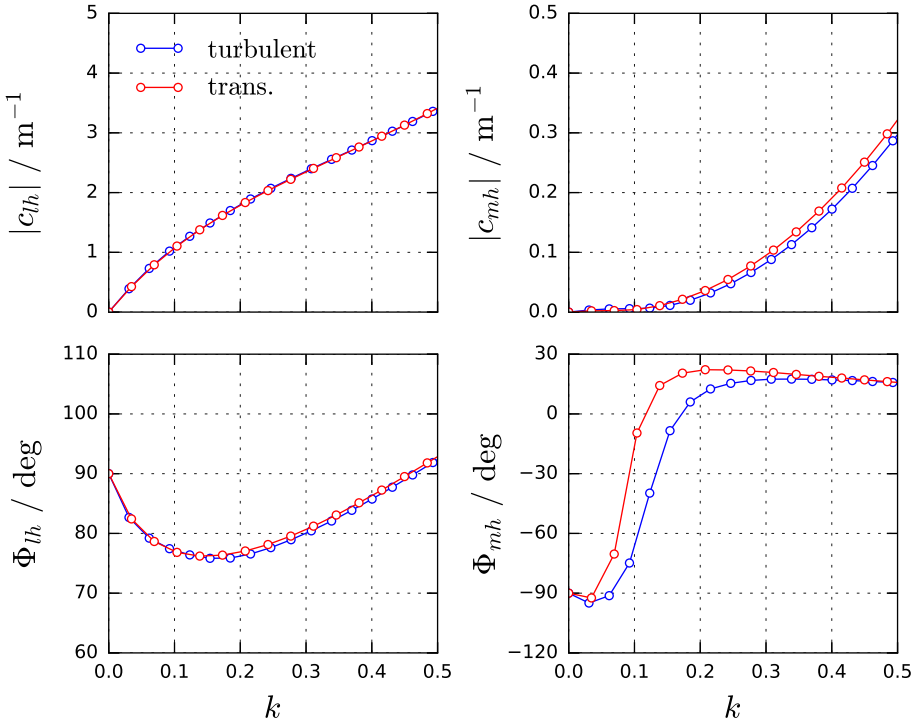

Figure 5.55: NLF(2)-0415M: Unsteady lift and moment for $\alpha_m = 0.55° \ / \ 0°$ due to heave

NLF(2)-0415M: Flutter Results

This section presents the flutter results based on the unsteady aerodynamic derivatives at the upper drag bucket limit. A p-k solver is used to compute the flutter stability for the transitional and fully turbulent flow. Table 5.15 gives the flutter speed U_{fl} and the reduced frequency at flutter k_{fl}. Figure 5.56 and 5.57 depict the frequency and reduced damping for each mode in the considered velocity range. The transitional results (red) at $\alpha = 0.2°$ and $0.55°$ are compared to the fully turbulent result (blue) at $\alpha_m = 0°$. The full vertical lines mark the zero damping crossing.

Table 5.15: NLF(2)-0415M: Flutter results

	transitional			fully turbulent		
α_m / deg	mode	U_{fl} / (m/s)	k_{fl}	mode	U_{fl} / (m/s)	k_{fl}
0				1	119.0	0.285
0.2	1	112.9	0.297			
0.55	1	113.1	0.296			

The unsteady aerodynamic data are obtained at a specific Reynolds number, Mach number, and ambient temperature ($T = 273.1$ K), which define the thermodynamic state for a given chord length. A velocity variation with a fixed Reynolds and Mach number results in a density variation in the flutter calculation. The dashed vertical line in the flutter diagram indicates the freestream velocity given in the CFD computation U_{CFD}.

The binary model shows classical bending-torsion flutter. As the frequencies of both modes converge, the damping decreases and the heave-dominated mode gets unstable. The flutter speed does not change as the laminar drag bucket is left and the difference to the fully turbulent flutter speed is small. This behavior is already indicated by the unsteady aerodynamic data. A significant difference exists neither in-between the transitional unsteady results for both angles of attack, nor for the transitional results compared to the fully turbulent results.

The nonlinearity in the lift and moment coefficient curve resembles the nonlinearities described by Fehrs et al. (2015) for the CAST10-2 airfoil at $Re = 2 \cdot 10^6$. However, there is no significant change in the unsteady aerodynamics or flutter stability as described by Fehrs et al. (2015). The reason is given by the drag bucket characteristic. For both airfoils, the drag bucket is left as the angle of attack increases with an upstream movement of the transition location. In the case of the CAST10-2 exist stable transition locations in the nonlinear lift curve region

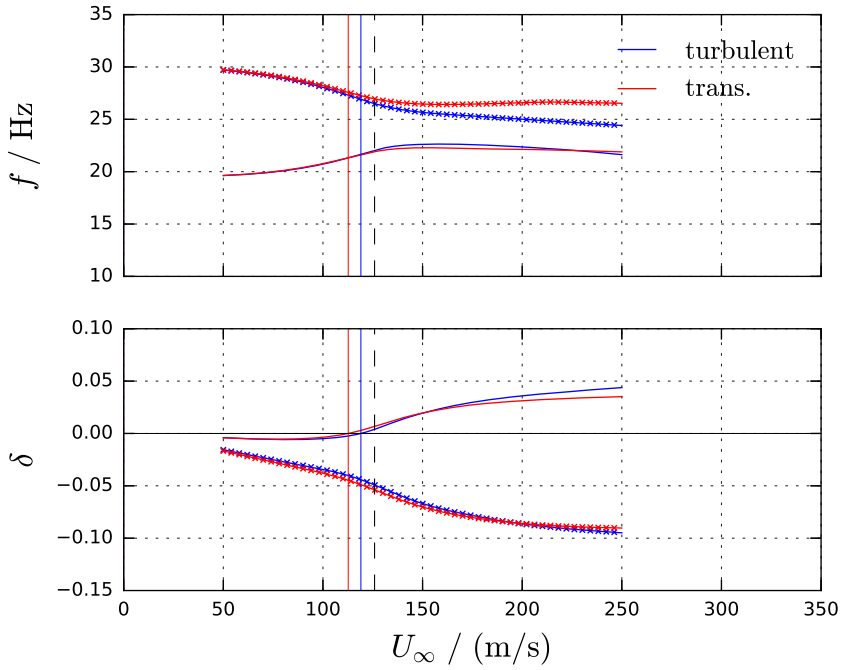

Figure 5.56: NLF(2)-0415M: Flutter results for $\alpha_m = 0.2° \ / \ 0°$

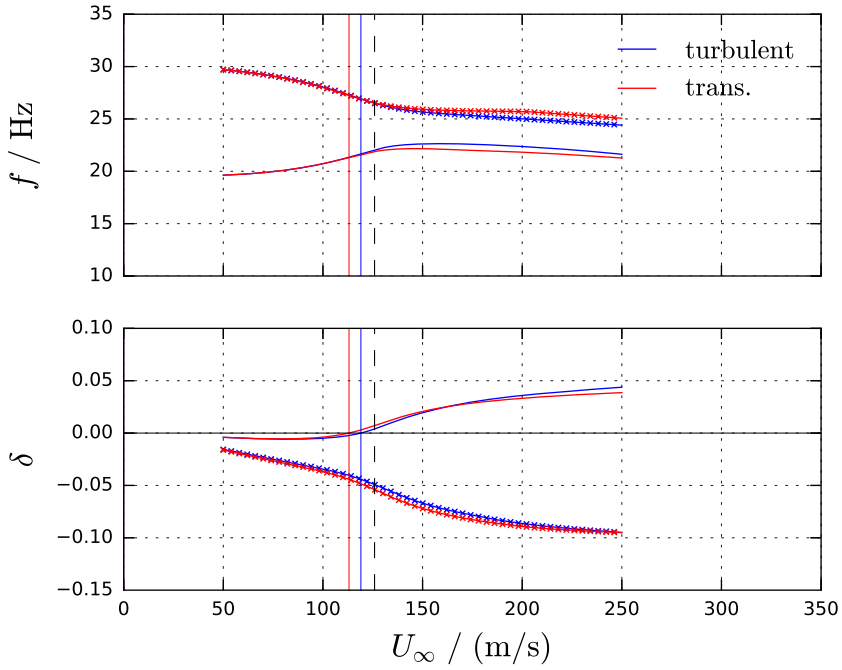

Figure 5.57: NLF(2)-0415M: Flutter results for $\alpha_m = 0.55° \ / \ 0°$

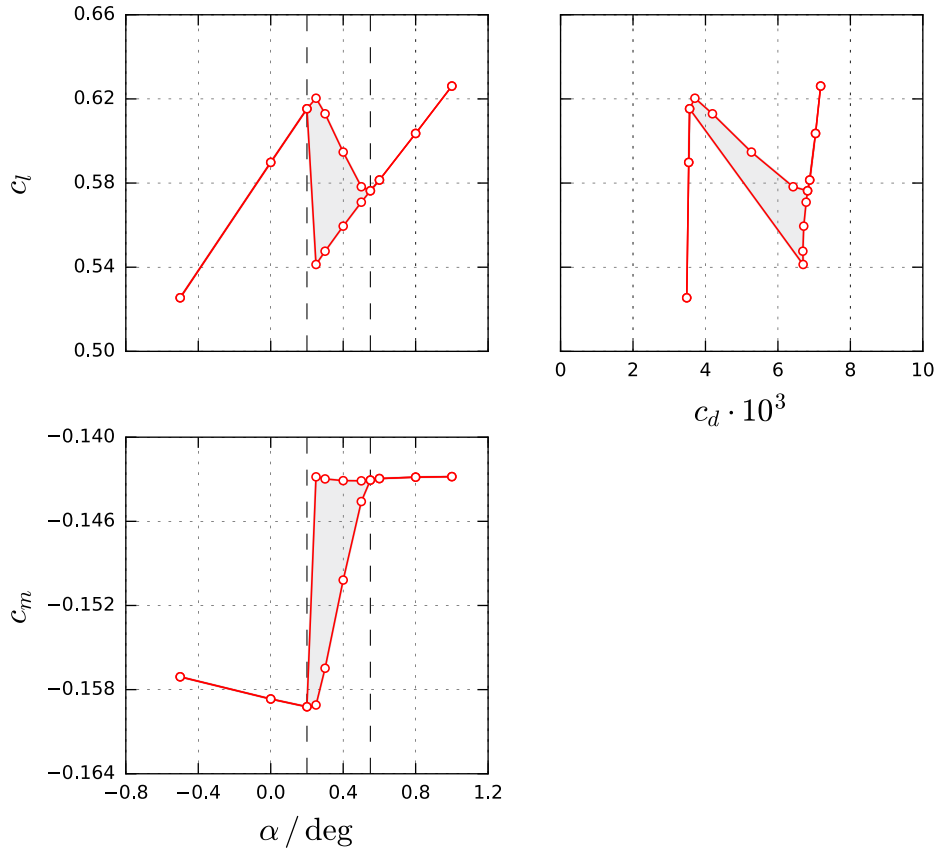

Figure 5.58: NLF(2)-0415M: Upper drag bucket limit

with transition positions at mid-chord. This is not the case for the NLF(2)-0415M.

Figure 5.58 depicts the aerodynamic coefficient curves at the upper drag bucket limit for the transitional flow. The dashed vertical lines indicate $\alpha = 0.2°$ and $0.55°$. The flow is unsteady between these angles of attack. The computation oscillates between the values limiting the gray area. There is no continuous variation of steady flow solutions at the drag bucket limit as it is found for the CAST10-2. Assuming linearity at each steady state, the lift curve slope is not changed at the local extrema of c_l at the drag bucket limit compared to the overall lift curve.

NLF(2)-0415M: Summary

The NLF(2)-0415M encounters a nonlinear lift and moment variation at the drag bucket limit. As the transition location moves upstream at the upper drag bucket limit, the lift decreases and the moment around quarter-chord increases. Unsteady computations are performed at the

drag bucket limit to obtain the aerodynamic derivatives required for a flutter computation.

It is found that there is no significant change in the unsteady aerodynamic characteristic as the drag bucket is left. Therefore, there are only minor changes in the flutter behavior. The linearization by small amplitude oscillations around the steady state solution at the drag bucket limit does not result in a changed flutter behavior. Although the steady results indicate local extrema in the lift and moment coefficients, there is no change in the unsteady aerodynamics associated with an inversed lift or moment curve slope.

5.4.4 RAE 2822: Supercritical Airfoil

RAE 2822: Test Case Description

The second unsteady test case is the supercritical airfoil RAE 2822 in transonic flow at a free flight Reynolds number. The design coordinates are given by Cook et al. (1979). The airfoil is depicted in Fig. 5.59. The flow conditions are given by $Re = 20 \cdot 10^6$, $M = 0.75$, and a turbulence level of $\tau = 0.05$ %. The inviscid design condition is given at $M = 0.66$ with $c_l = 0.56$ at $\alpha = 1.06°$ (Cook et al. 1979). For this test case, a flow condition is desired, which gives an interaction of a shock with the laminar boundary layer flow. The structural model is kept but the chord length is increased to $c = 1$ m to give flutter results closer to the matched condition at U_{CFD}.

The computations are performed on a computational grid with a cell length along the airfoil of $\Delta x/c \approx 0.004$ and $y^+_{max} < 1$. The farfield is about 100 chord lengths away from the airfoil. For the unsteady computations, the linear system identification approach (pulse) by Kaiser et al. (2015) is used for amplitudes of $\widehat{\alpha} = 1° \cdot 10^{-5}$ to 10^{-6} and $\widehat{h} = 10^{-5}$ m to 10^{-6} m.

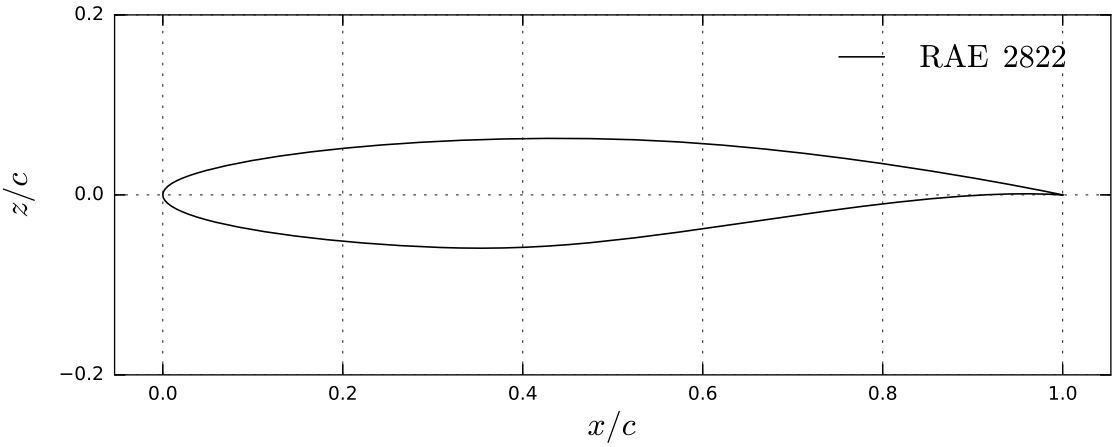

Figure 5.59: RAE 2822: Geometry

RAE 2822: Steady Results

Figure 5.60 depicts the lift, drag, and quarter-chord moment coefficient curve for the transitional and fully turbulent flow. The lift increase is linear for both flow conditions up to $\alpha = 2°$. There is no laminar drag bucket because the transition location is far downstream for the whole angle of attack range. For higher angles of attack, the lift stalls as the airfoil reaches the drag divergence Mach number.

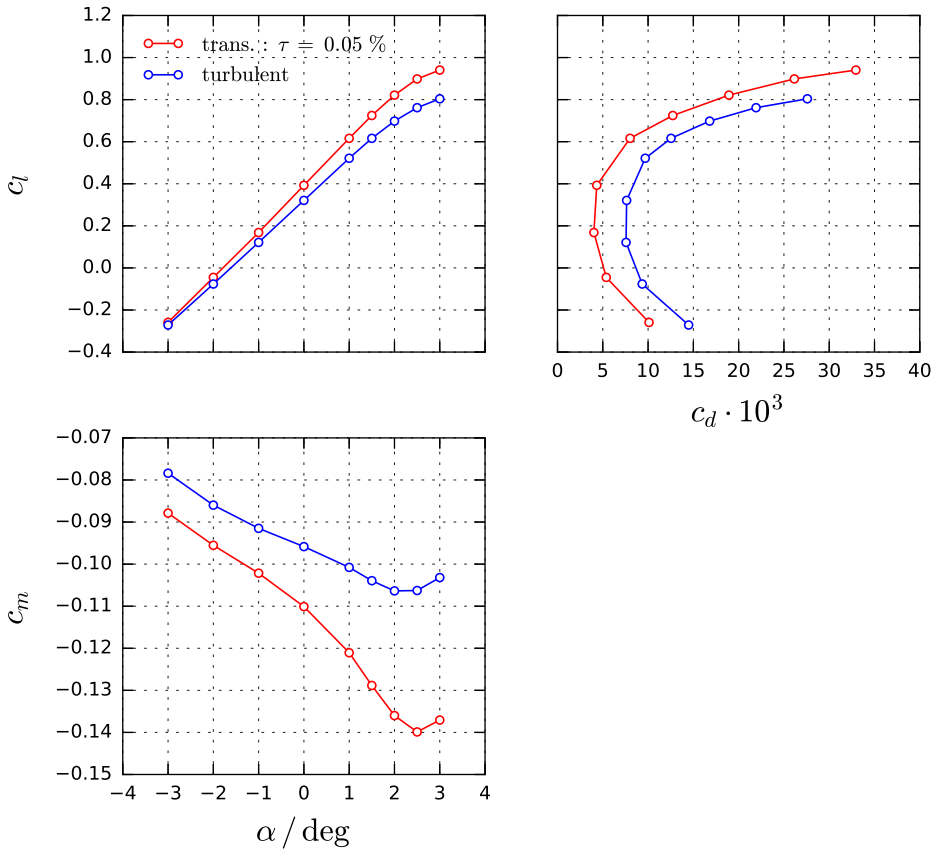

Figure 5.60: RAE 2822: Lift, drag, and moment curves

For angles of attack $\alpha < 1°$, there is some drag benefit from the laminar boundary layer flow. This drag benefit is lost for increasing angles of attack. The transitional flow encounters stronger shocks with shock-induced laminar separations, which increase the airfoil drag strongly. The moment coefficients of the transitional and fully turbulent flow diverge with increasing angle of attack. The fully turbulent flow gives a rather linear behavior up to $\alpha = 2°$. The transitional moment coefficient slope increases with angle of attack.

Figure 5.61 and 5.62 depict the pressure and skin friction coefficient distribution for $\alpha = 0°$ to 3°. The critical pressure coefficient for $M = 0.75$ is $c_{p,\,crit} = -0.59$. The flow is transonic on the suction side. In the case of the transitional flow, the shock is stronger and further downstream for all angles of attack. The boundary layer is laminar up to the pressure minimum. Transition is caused by the adverse pressure gradient and not the shock on the upper surface. For high Reynolds number flows, the intermittency increase occurs over a rather short length in an adverse pressure gradient flow and a longer transition region might give a more realistic

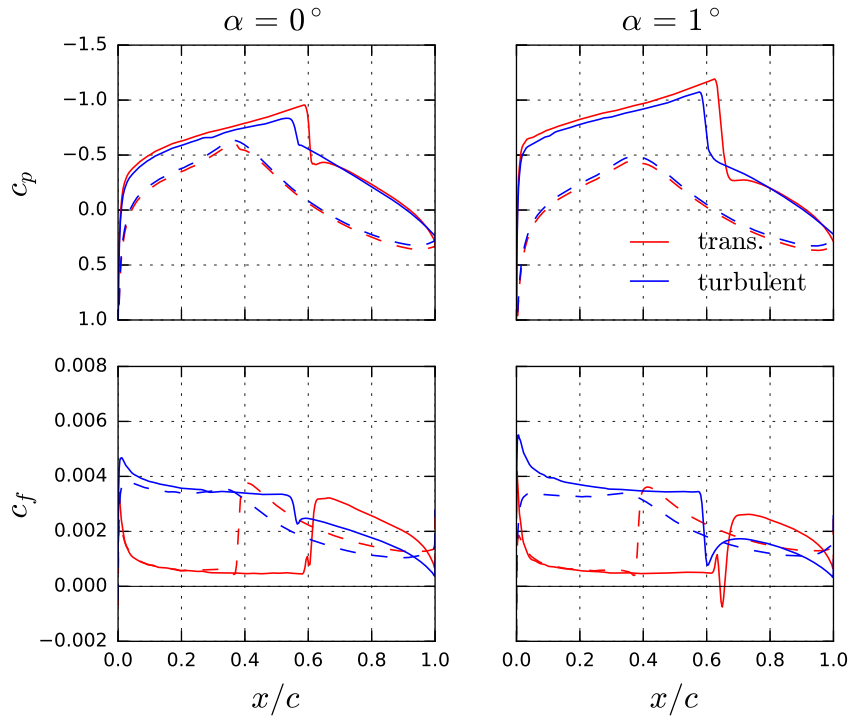

Figure 5.61: RAE 2822: Pressure and skin friction coefficient distribution for $\alpha = 0°$ and $1°$

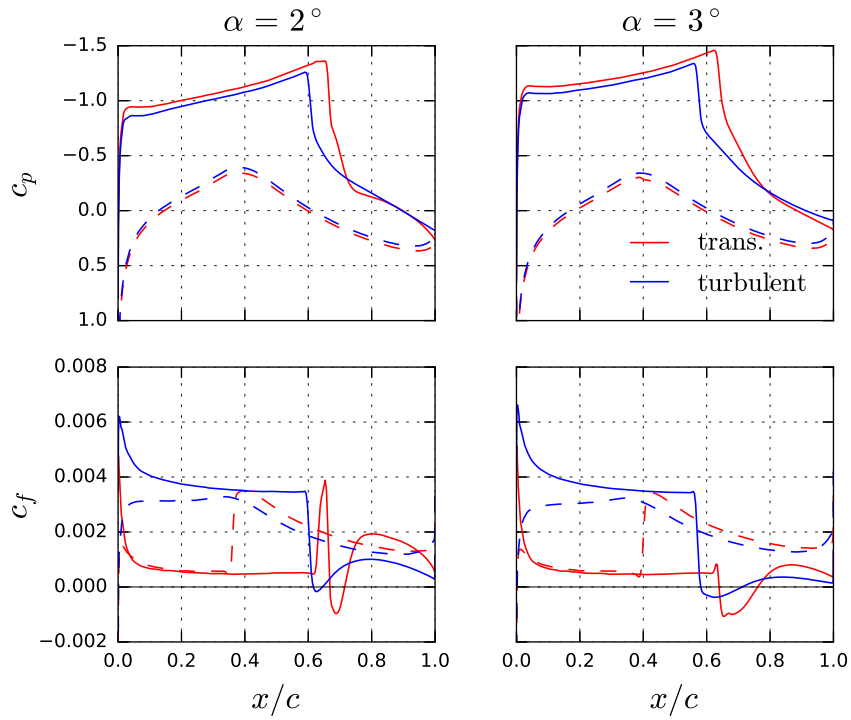

Figure 5.62: RAE 2822: Pressure and skin friction coefficient distribution for $\alpha = 2°$ and $3°$

shock-boundary layer interaction.

For $\alpha > 1°$, the transitional boundary layer shows a shock-induced separation. The fully turbulent flow requires a stronger shock for the boundary layer to separate, which is given for $\alpha > 2°$. On the lower surface, transition takes place once the adverse pressure gradient region is reached. For both flow conditions and all angles of attack, the lower surface is shock-free.

For the given angle of attack range, no laminar drag bucket is found. There is no sudden change in the transition position as it is found for the NLF(2)-0415M. No suction peak develops on the upper surface of the RAE 2822 for the given flow conditions, which would be required for an upstream transition position.

RAE 2822: Unsteady Results

Figure 5.63 to 5.66 depict the unsteady results for the mean angles of attack $\alpha_m = 0°$, $1°$, and $2°$ for a fully turbulent and a transitional flow. Figure 5.63 and 5.64 present the results for $\alpha_m = 0°$ for pitch and heave motion. The lift coefficient derivatives $c_{l\alpha}$ and c_{lh} show a similar behavior for both types of flow in magnitude and phase with a minor difference for the quasi-steady magnitude at $k = 0$ for $c_{l\alpha}$. Only at $\alpha_m = 2°$, there are some qualitative differences in the phase of the lift coefficient derivatives as $c_{l,\,max}$ is approached.

The moment coefficient variation is almost linear for the turbulent flow up to $\alpha = 2°$. The transitional moment coefficients run parallel to the fully turbulent values for low angles of attack. For angles of attack $\alpha > -1°$, the moment coefficients start to diverge from the turbulent values as can be seen in Fig. 5.60. This increasing difference is also found in the unsteady moment coefficient behavior (Fig. 5.63 to 5.66). There is a pronounced difference in magnitude and phase for the unsteady aerodynamic moment.

The transitional flow for $\alpha_m = 1°$ and $2°$ gives a phase lead of the aerodynamic moment with $\Phi_{m\alpha} < -180°$. A phase lead enables a 1-dof flutter of the pitch mode. A similar phase lead is shown for the supercritical CAST10-2 airfoil in a wind tunnel experiment with free transition by Hebler (2013) and numerically by Fehrs et al. (2015). The phase lead for the CAST10-2 and the RAE 2822 is found in an angle of attack range with a strong negative moment curve slope.

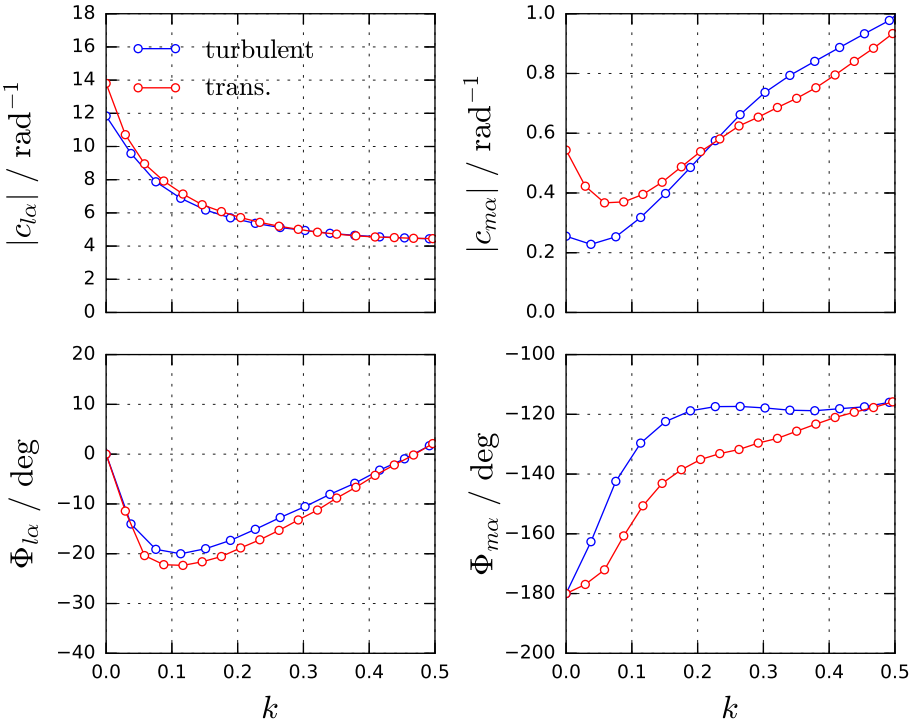

Figure 5.63: RAE 2822: Unsteady lift and moment for $\alpha_m = 0°$ due to pitch

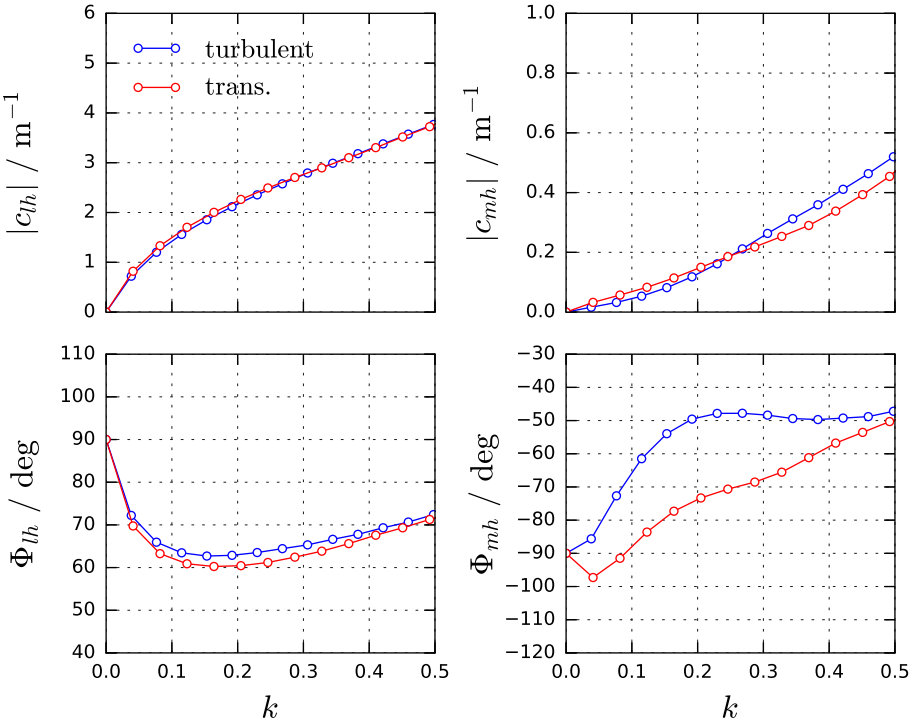

Figure 5.64: RAE 2822: Unsteady lift and moment for $\alpha_m = 0°$ due to heave

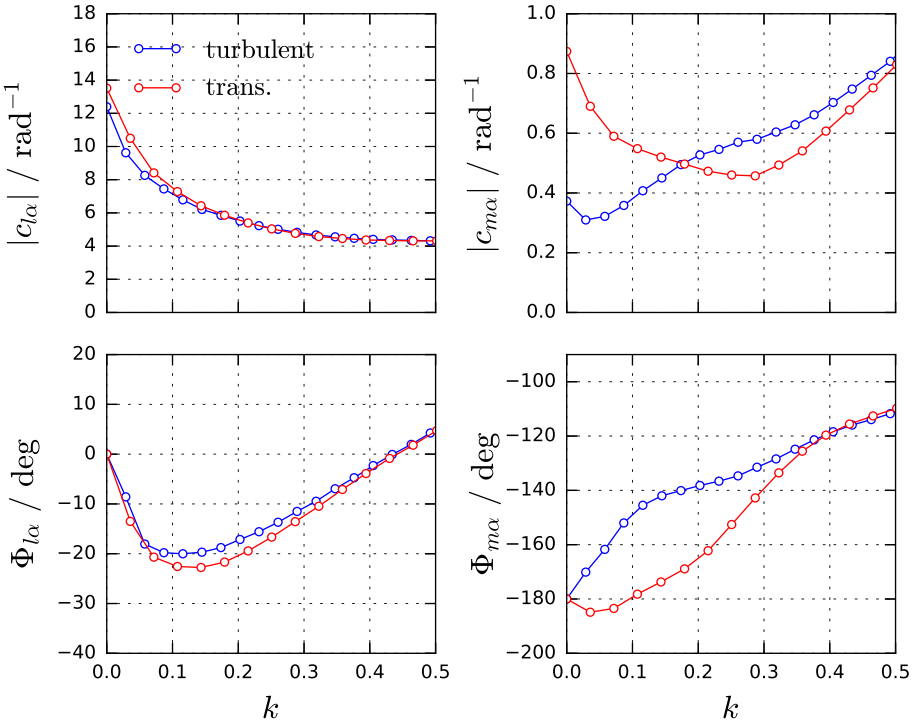

Figure 5.65: RAE 2822: Unsteady lift and moment for $\alpha_m = 1°$ due to pitch

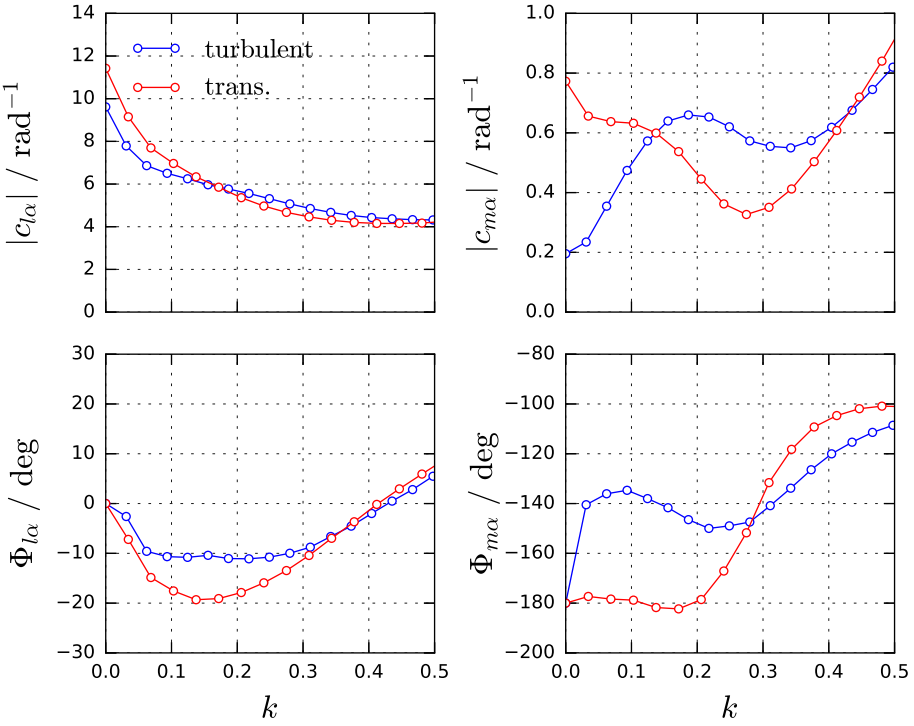

Figure 5.66: RAE 2822: Unsteady lift and moment for $\alpha_m = 2°$ due to pitch

RAE 2822: Grid Dependency

As pointed out above, the intermittency increase is confined to a few grid points along the surface and there might exist a stronger interaction of the shock with the transitional boundary layer on a finer grid. Figure 5.67 depicts the pressure and skin friction coefficient distribution on the baseline grid with $\Delta x/c = 0.004$ and on a refined grid with a cell length of $\Delta x/c = 0.002$.

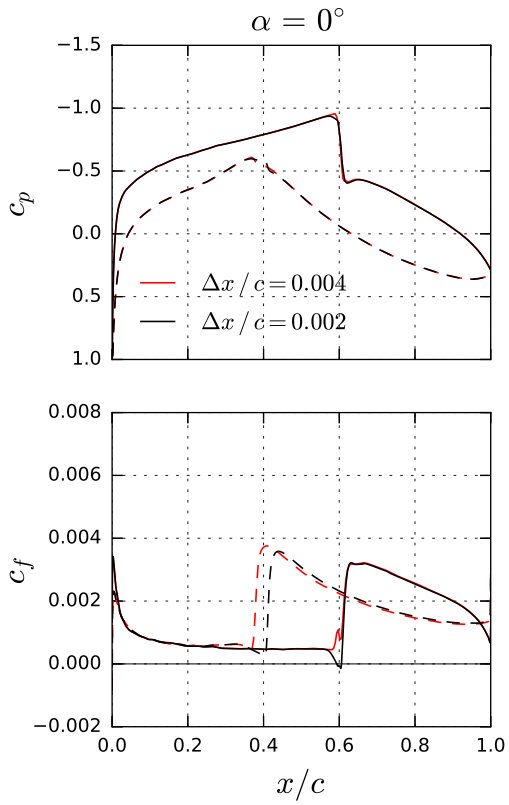

Figure 5.67: RAE 2822: Grid dependency of c_p and c_f at $\alpha = 0°$

The first intermittency increase (transition onset) on the upper surface is given at $x/c \approx 0.585$ on the coarse grid. On the finer grid, the transition onset moves slightly upstream to $x/c \approx 0.57$. At the same time, the intermittency growth expands over a larger distance along the airfoil. Once the laminar boundary layer encounters the adverse pressure gradient region, the laminar boundary layer separates. The turbulent flow reattaches downstream of the shock. Although the pressure distribution is hardly affected by the grid refinement, the boundary layer transition shows a very different characteristic as the flow detaches at the shock location.

Single frequency pitch computations are performed for both grids. The pitch motion has an amplitude of $\widehat{\alpha} = 1° \cdot 10^{-4}$. The results are compared to the pulse excitation (amplitude $\widehat{\alpha} = 1° \cdot 10^{-5}$) in Fig. 5.68. There is no pronounced effect of the finer grid on the unsteady

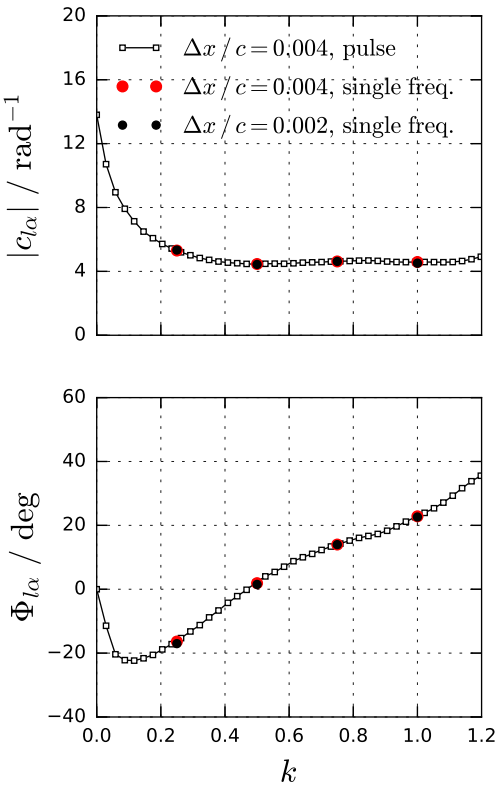

Figure 5.68: RAE 2822: Grid dependency of $c_{l\alpha}$ at $\alpha_m = 0°$

results for $c_{l\alpha}$. In addition, the single frequency computations match the pulse results. This indicates an amplitude independence of the results.

RAE 2822: Flutter Results

This section presents flutter results for the RAE 2822 based on the unsteady aerodynamic data. The same structural model as for the NLF(2)-0415M given in Section 5.4.3 is used. Table 5.16 presents the flutter speed U_{fl} and the reduced frequency at flutter k_{fl} for the RAE 2822. Figure 5.69 to 5.71 depict the frequency and reduced damping curves for the fully turbulent (blue) and transitional (red) flow.

Table 5.16: RAE 2822: Flutter results

	transitional			fully turbulent		
α_m / deg	mode	U_{fl} / (m/s)	k_{fl}	mode	U_{fl} / (m/s)	k_{fl}
0	1	211.4	0.313	1	207.0	0.319
1	1	226.6	0.297	1	219.0	0.305
2	1	236.3	0.288	1	242.6	0.282

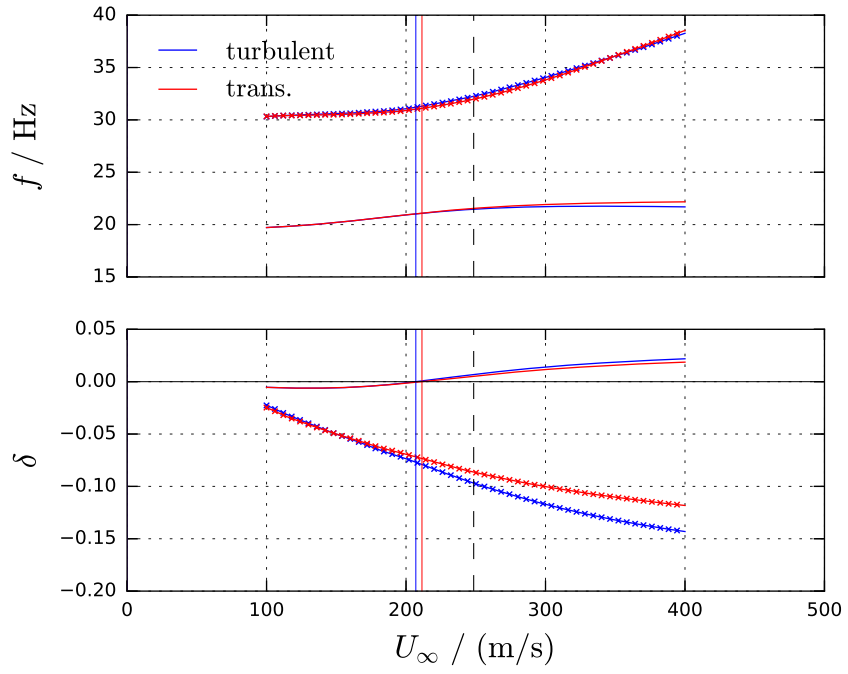

Figure 5.69: RAE 2822: Flutter results for $\alpha_m = 0°$

The first heave-dominated mode gets unstable for all mean angles of attack. The overall flutter speed increases with the mean angle of attack and the reduced frequency at flutter is

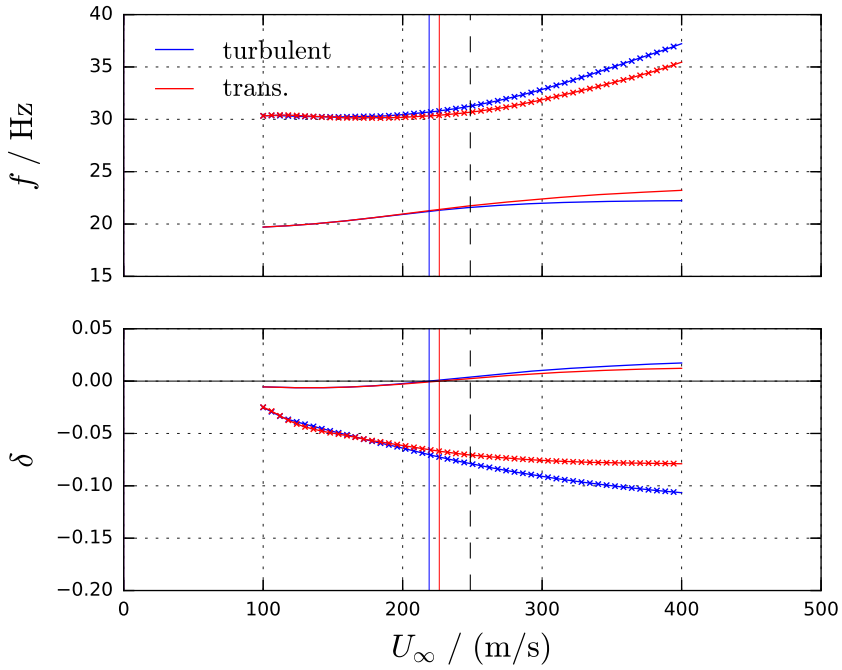

Figure 5.70: RAE 2822: Flutter results for $\alpha_m = 1°$

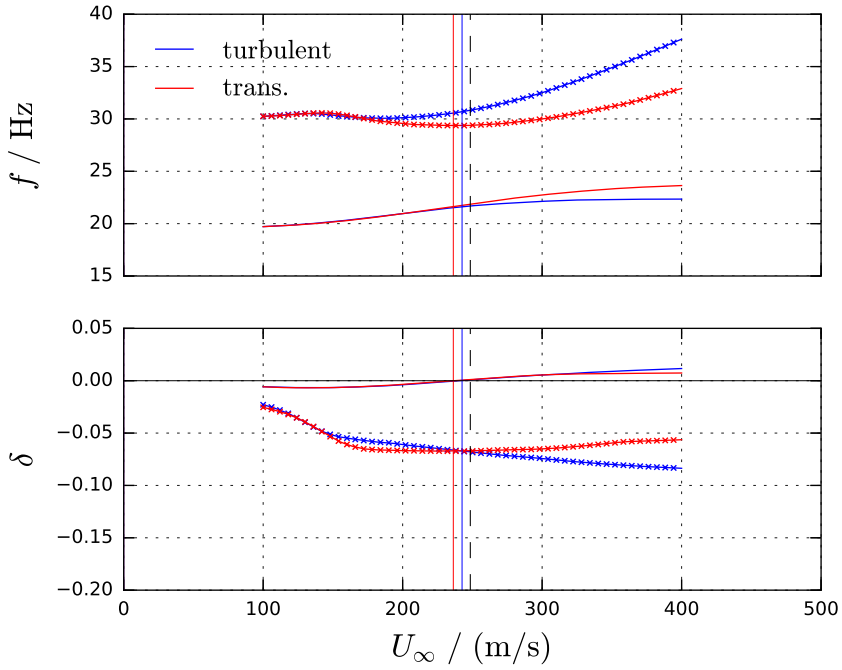

Figure 5.71: RAE 2822: Flutter results for $\alpha_m = 2°$

decreased. The second mode frequency of the transitional flow bends stronger towards the first mode as the mean angle of attack is increased, which supports the required mode interaction for the 2-dof flutter.

The main difference in the unsteady aerodynamics is found for reduced frequencies below $k = 0.3$. The structural model gives critical reduced frequencies at flutter of $k \approx 0.3$. Therefore, no pronounced difference between the fully turbulent and transitional flow is found. To demonstrate the effect of free boundary layer transition, a 1-dof system is considered. The chord length is changed to $c = 0.385$ m to obtain a critical reduced frequency at flutter below $k = 0.2$. For a constant mass and radius of gyration, a change of the chord length results in a variation of the mass moment of inertia I_α.

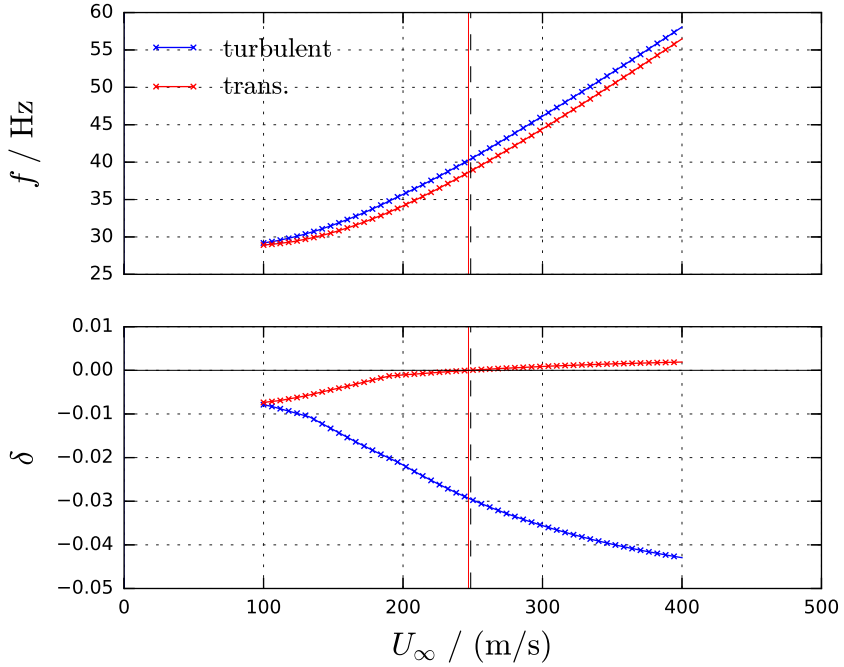

Figure 5.72: RAE 2822: 1-dof flutter results for $\alpha_m = 2°$

Fig. 5.72 depicts the flutter results for the 1-dof model. The transitional (red) results show a torsional flutter at $U_{fl} = 246.9$ m/s with $k_{fl} = 0.189$. In addition, this case represents a matched condition as $U_{CFD} = 248.5$ m/s. At the flutter speed, the indifference point for torsional flutter with Im $(c_{m\alpha}) = 0$ is given, which is only possible for the transitional flow as can be seen in Fig. 5.66.

For the 2-dof system with $c = 0.385$ m, the torsional flutter does not occur. The structural and aerodynamic coupling result in an instability of the first, heave-dominated mode with a severe reduction of the flutter speed compared to the baseline model with $c = 1$ m.

RAE 2822: Summary

The unsteady test case for the RAE 2822 covers a high Reynolds number flow at a transonic Mach number in a low disturbance environment. The steady computations give a linear lift increase for the fully turbulent and transitional flow. No laminar drag bucket is encountered as no sudden change in the transition position exists. Although qualitative similar, the transitional moment coefficient shows a stronger variation with angle of attack compared to the fully turbulent case.

This difference is also found in the unsteady results. The transitional moment coefficient derivatives show a deviation from the fully turbulent results. Most important, the pitch moment coefficient shows a phase lead in a certain reduced frequency range, which enables a torsional flutter. A similar torsional flutter is known for the CAST10-2 airfoil at $Re = 2 \cdot 10^6$.

The given structural model results in a similar flutter behavior for both flow conditions. As the reduced frequency at flutter decreases, the flutter behavior starts to deviate stronger. For a transonic flow, the effect of transition has to be considered as the separation behavior, shock strength, and shock position is changed. The different mean flow conditions give a modification of the unsteady aerodynamics at low reduced frequencies.

6 Conclusion

This thesis presents a transition model based on the γ-Re$_\theta$ transition model. The original model is reduced to a one-equation model for the intermittency variable γ. The transition onset is computed based on an algebraic equation that replaces the $\widetilde{Re}_{\theta t}$ transport equation. The correlation includes the effect of freestream turbulence level and pressure gradients on the onset of transition.

Boundary layer transition in external aerodynamics is usually governed by a low disturbance environment. Therefore, the dominant transition mechanism is Tollmien-Schlichting transition or, in the case of 3-dimensional flows, additional crossflow and attachment line transition. The proposed correlation is based on an extensive study of existing experimental data and correlations proposed in literature. In contrast to the original model, a strong stabilizing effect of favorable pressure gradients is identified and included in the model. The pressure gradient correlation is based on the acceleration parameter K, which can be computed directly inside the boundary layer.

The model is fine tuned using experimental data for 2-dimensional airfoil test cases at moderate Mach numbers and moderate to high Reynolds numbers. After calibration, a large number of validation test cases are computed. The model gives reasonable results up to Reynolds numbers found in free flight. In addition, the extent of the laminar drag bucket is well predicted for moderate Reynolds numbers and the model behavior is similar to the well established e^N method.

The γ transition model closes an existing gap for high Reynolds number, external aerodynamic applications in correlation-based transition modeling. Although the γ transition model gives reliable results for the considered flows, further work is needed to gather more data to validate and extend the given model. The transition model can be extended by existing correlations for crossflow transition. Crossflow transition is the main transition mechanism in flows around conventional aircraft configurations. In addition, a Galilean invariant formulation is desirable for the calculation of full rotor applications for wind turbines or helicopters. For airfoils and wings, Galilean invariance is a minor problem.

The unsteady validation test case and the unsteady high Reynolds number computations set forth the effect of flows with free boundary layer transition on the aerodynamics and the

aeroelastic behavior. Although boundary layer effects are more pronounced at low Reynolds numbers, a partly laminar flow still affects the drag and lift at free flight Reynolds numbers. More important for aeroelastic considerations, the occurrence of laminar separations, shock positions, and the shock strength are directly influenced by an upstream laminar boundary layer. These effects enable novel aeroelastic effects like a torsional, transition-induced 1-dof flutter.

The unsteady computations are based on the assumption that the transport equation approach gives a qualitative correct representation of the unsteady transition behavior. A further discussion of the aeroelastic behavior requires additional unsteady wind tunnel test data, which allow an evaluation of the unsteady transition behavior at high Reynolds numbers. This includes the influence of unsteady pressure distributions on the boundary layer receptivity process and the transition process itself to give a comprehensive unsteady transition model.

Boundary layer flows with free transition are more complicated to predict, to discuss, and the resulting aerodynamic and aeroelastic behavior is hard to predict without any specific and detailed investigation. Morkovin gives a farsighted advice right at the beginning of his report that should be followed:

> "*... don't get discouraged about transition problems too early - they have a way of being around for decades.*" (Morkovin 1969, p. 7)

Bibliography

Abbott, I. H., von Doenhoff, A. E., and Stivers, L. S., Jr. "Summary of Airfoil Data," NACA, TR-824, 1945.

Abu-Ghannam, B. J. and Shaw, R. "Natural Transition of Boundary Layers - The Effects of Turbulence, Pressure Gradient, and Flow History," *Journal of Mechanical Engineering Science*, Vol. 22, No. 5, pp. 213–228, 1980.

Anderson, J. D., Jr. *Fundamentals of Aerodynamics*. 4$^{\text{th}}$ ed., McGraw-Hill, New York, 2007.

Arnal, D. "Description and Prediction of Transition in Two-Dimensional, Incompressible Flow," *Special Course on Stability and Transition of Laminar Flow* edited by R. Michel, AGARD, AGARD-R-709, 1984.

Arnal, D. "Laminar-Turbulent Transition Problems in Supersonic and Hypersonic Flows," *Special Course on Aerothermodynamics of Hypersonic Vehicles* edited by J. F. Wendt, AGARD, AGARD-R-761, 1989.

Arnal, D. and Casalis, G. "Laminar-Turbulent Transition Prediction in Three-Dimensional Flows," *Progress in Aerospace Sciences*, Vol. 36, No. 2, pp. 173–191, 2000.

Bansmer, S., Radespiel, R., Unger, R., Haupt, M., and Horst, P. "Experimental and Numerical Fluid-Structure Analysis of Rigid and Flexible Flapping Airfoils," *AIAA Journal*, Vol. 48, No. 9, pp. 1959-1974, 2010.

Bennett, H. W. "An Experimental Study of Boundary Layer Transition," Kimberly-Clark Corporation, Report, 1953.

Betchov, R. and Criminale, W. O., Jr. "Stability of Parallel Flows," *Applied Mathematics and Mechanics* edited by F. N. Frenkiel, G. Temple, Vol. 10, Academic Press, New York, 1967.

Bippes, H. "Basic Experiments on Transition in Three-Dimensional Boundary Layers Dominated by Crossflow Instability,"*Progress in Aerospace Sciences*, Vol. 35, No. 4, pp. 363–412, 1999.

Bisplinghoff, R. L., Ashley, H., and Halfman, R. L. *Aeroelasticity*. 1st ed., Dover Publications, Mineola, 1996.

Boerstoel, J. W. and Huizing, G. H. "Transonic Shock-Free Aerofoil Design by an Analytic Hodograph Method," *Journal of Aircraft*, Vol. 12, No. 9, pp. 730–736, 1975.

Boiko, A. V., Grek, G. R., Dovgal, A. V., and Kozlov, V. V. *The Origin of Turbulence in Near-Wall Flows*, 1st ed., Springer, Berlin, 2002.

Braslow, A. L. and Visconti, F. "Investigation of Boundary-Layer Reynolds Number for Transition on an NACA $65_{(215)}$-114 Airfoil in the Langley Two-Dimensional Low-Turbulence Pressure Tunnel," NACA, TN-1704, Washington, D.C., 1948.

Brown, A. and Martin, B. W. "The Use of Velocity Gradient Factor as a Pressure Gradient Parameter," *Proceedings of the Intitution of Mechanical Engineers*, Vol. 190, No. 14/76, pp. 277–285, 1976.

Content, C. and Houdeville, R. "Application of the γ-R_θ Laminar-Turbulent Transition Model in Navier-Stokes Computations," *40th Fluid Dynamics Conference and Exhibit*, AIAA, Chicago, 2010.

Cook, P. H., McDonald, M. A., and Firmin, M. C. P. "Aerofoil RAE 2822 - Pressure Distributions, and Boundary Layer and Wake Measurements," *Experimental Data Base for Computer Program Assessment*, edited by J. Barche, AGARD, AGARD-AR-138, 1979.

Crabtree, L. F. "Prediction of Transition in the Boundary Layer on an Aerofoil," *Journal of the Royal Aeronautical Society*, Vol. 62, pp. 525–528, 1958.

Criminale, W. O., Jackson, T. L., and Joslin, R. D. *Theory and Computation in Hydrodynamic Stability*. 1st ed., Cambridge University Press, Cambridge, 2003.

Dagenhart, J. R. and Saric, W. S. "Crossflow Stability and Transition Experiments in Swept-Wing Flow," NASA, TP-1999-209344, Hampton, 1999.

Dhawan, S. and Narasimha, R. "Some Properties of Boundary Layer Flow During the Transition from Laminar to Turbulent Motion," *Journal of Fluid Mechanics*, Vol. 3, No. 4, pp. 418–436, 1958.

Dietz, G., Schewe, G., and Mai, H. "Experiments on Heave/Pitch Limit-Cycle Oscillations of a Supercritical Airfoil Close to the Transonic Dip," *Journal of Fluids and Structures*, Vol. 19, No. 1, pp. 1–16, 2004.

DLR AS. "Technical Documentation of the DLR TAU-Code Release 2015.1.0," DLR, Technical Report, Braunschweig, 2015.

Dress, D. A., Johnson, C. B., McGuire, P. D., Stanewsky, E., and Ray, E. J. "High Reynolds Number Tests of the CAST 10-2/DOA 2 Airfoil in the Langley 0.3-Meter Transonic Cryogenic Tunnel - Phase I," NASA, TM-84620, Hampton, 1983.

Dryden, H. L. "Air Flow in the Boundary Layer Near a Plate," NACA, TR-562, Washington, D.C., 1937.

Dunham, J. "Predictions of Boundary Layer Transition on Turbomachinery Blades," *Boundary Layer Effects in Turbomachines* edited by J. Surugue, AGARD, AGARD-AG-164, pp. 57–71, 1972.

Emmons, H. W. "The Laminar-Turbulent Transition in a Boundary Layer-Part I," *Journal of the Aeronautical Sciences*, Vol. 18, No. 7, pp. 490–498, 1951.

Erickson, L. L. "Transonic Single-Mode Flutter and Buffet of a Low Aspect Ratio Wing Having a Subsonic Airfoil Shape," NASA, TN-D-7346, Washington, D.C., 1974.

Fehrs, M. "Erweiterte Auswertung des Turbulenzgrads aus der TWG-Messkampagne 2011," DLR, Institute of Aeroelasticity, Internal Presentation, Göttingen, 2015.

Fehrs, M., van Rooij, A. C. L. M., and Nitzsche, J. "Influence of Boundary Layer Transition on the Flutter Behavior of a Supercritical Airfoil," *CEAS Aeronautical Journal*, Vol. 6, No. 2, pp. 291–303, 2015.

Fisher, D. F. and Dougherty, N. S., Jr. "Flight and Wind-Tunnel Correlation of Boundary-Layer Transition on the AEDC Transition Cone," NASA, TM-84902, Washington, D.C., 1982.

Freymann, R. *Strukturdynamik*, 1st ed., Springer, Heidelberg, 2011.

Fröhlich, J. *Large Eddy Simulation turbulenter Strömungen*, 1st ed., Teubner, Wiesbaden, 2006.

Fung, Y. C. *An Introduction to the Theory of Aeroelasticity*, 1st ed., Dover Publications, Mineola, 2002.

Försching, H. and Tichy, L. "Grundlagen der Aeroelastik," *Handbuch der Luftfahrzeugtechnik* edited by C.-C. Rossow, K. Wolf, P. Horst, Hanser Verlag, München, 2014.

Grabe, C., Nie, S., and Krumbein, A. "Transition Transport Modeling for the Prediction of Crossflow Transition," *34^{th} AIAA Applied Aerodynamics Conference*, AIAA, Washington, D.C., 2016.

Granville, P. S. "The Calculation of the Viscous Drag of Bodies of Revolution," NAVY Department - The David W. Taylor Model Basin, 849 NS715-102, Washington, D.C., 1953.

Gray, W. E. "The Effect of Wing Sweep on Laminar Flow," Royal Aircraft Establishment, TM-Aero-255, Fanborough, 1952.

Gregory, N. "Transition and the Spread of Turbulence on a 60° Swept-Back Wing," *Journal of the Royal Aeronautical Society*, Vol. 64, pp. 562–564, 1960.

Hall, D. J. and Gibbings, J. C. "Influence of Stream Turbulence and Pressure Gradient Upon Boundary Layer Transition," *Journal of Mechanical Engineering Science*, Vol. 14, No. 2, pp. 134–146, 1972.

Hassig, H. J. "An Approximate True Damping Solution of the Flutter Equation by Determinant Iteration," *Journal of Aircraft*, Vol. 8, No. 11, pp. 885–889, 1971.

Hebler, A., Schojda, L., and Mai, H. "Experimental Investigation of the Aeroelastic Behavior of a Laminar Airfoil in Transonic Flow," *Proc. IFASD 2013*, IFASD, Bristol, 2013.

Hebler, A. "Aeroelastik am Laminarflügel - Versuchsbericht ALF-3," DLR, IB 232-2013 J 12, Göttingen, 2013.

Herwig, H. *Strömungsmechanik*. 1st ed., Vieweg + Teubner Verlag, Wiesbaden, 2008.

Horton, H. P. "Laminar Separation Bubbles in Two and Three Dimensional Incompressible Flow," Ph. D. Dissertation, Queen Mary College, University of London, London, 1968.

Houwink, R., Kraan, A. N., and Zwaan, R. J. "Wind-Tunnel Study of the Flutter Characteristics of a Supercritical Wing," *Journal of Aircraft*, Vol. 19, No. 5, pp. 400–405, 1982.

Jones, W. P. and Launder, B. E. "The Prediction of Laminarization with a Two-Equation Model of Turbulence," *International Journal of Heat and Mass Transfer*, Vol. 15, No. 2, pp. 301–314, 1972.

Kaiser, C., Thormann, R., Dimitrov, D., and Nitzsche, J. "Time-Linearized Analysis of Motion-Induced and Gust-Induced Airloads with the DLR TAU Code," *Deutscher Luft- und Raumfahrtkongress 2015*, Rostock, 2015.

Klebanoff, P. S. and Tidstrom, K. D. "Evolution of Amplified Waves Leading to Transition in a Boundary Layer with Zero Pressure Gradient," NASA, D-195, Washington, D.C., 1959.

Klimmek, T. "ALLEGRA Meilensteinbericht M 3.3.1 – Definition von Simulationsszenarien für die Böenanalyse der ALLEGRA Konfiguration," DLR, IB 232-2014 J 08, Göttingen, 2014.

Kovasznay, L. S. G., Komoda, H., and Vasudeva, B. R. "Detailed Flow Field in Transition," *Proceedings of the 1962 Heat Transfer and Fluid Mechanics Institute* edited by F. E. Ehlers et al., Stanford University Press, Stanford, 1962.

Krause, M., Behr, M., and Ballmann, J. "Modeling of Transition Effects in Hypersonic Intake Flows Using a Correlation-Based Intermittency Model," *15th AIAA International Space Planes and Hypersonic Systems and Technologies Conferences*, AIAA, Dayton, 2008.

Krumbein, A., Krimmelbein, N., and Schrauf, G. "Automatic Transition Prediction in Hybrid Flow Solver, Part 1: Methodology and Sensitivities," *Journal of Aircraft*, Vol. 46, No. 4, pp. 1176-1190, 2009a.

Krumbein, A., Krimmelbein, N., and Schrauf, G. "Automatic Transition Prediction in Hybrid Flow Solver, Part 2: Practical Application," *Journal of Aircraft*, Vol. 46, No. 4, pp. 1191-1199, 2009b.

Krumbein, A., Krimmelbein, N., and Seyfert, C. "Automatic Transition Prediction in Unsteady Airfoil Flows Using an Unstructured CFD Code," *29th AIAA Applied Aerodynamics Conference*, AIAA, Honolulu, 2011.

Kundu, P. K., Cohen, I. M., and Dowling, D. R. *Fluid Mechanics*, 5th ed., Elsevier, Amsterdam, 2012.

Langel, C. M., Chow, R., and van Dam, C. P. "A Comparison of Transition Prediction Methodologies Applied to High Reynolds Number External Flows," *54th AIAA Aerospace Sciences Meeting*, AIAA, San Diego, 2016.

Langtry, R. B. and Menter, F. R. "Correlation-Based Transition Modeling for Unstructured Parallelized Computational Fluid Dynamics Codes," *AIAA Journal*, Vol. 47, No. 12, pp. 2894–2906, 2009.

Langtry, R. B., Menter, F. R., Likki, S. R., Suzen, Y. B., Huang, P. G., and Völker, S. "A Correlation-Based Transition Model Using Local Variables – Part II: Test Cases and Industrial Applications," *Journal of Turbomachinery*, Vol. 128, No. 3, pp. 423-434, 2006.

Langtry, R. B. "A Correlation-Based Transition Model Using Local Variables for Unstructured Parallelized CFD Codes," Ph. D. Dissertation, University Stuttgart, Stuttgart, 2006.

Launder, B. E. "Laminarization of the Turbulent Boundary Layer by Acceleration," Gas Turbine Laboratory, MIT, Report 77, Cambridge, 1964a.

Launder, B. E. "Laminarization of the Turbulent Boundary Layer in a Severe Acceleration," *Journal of Applied Mechanics*, Vol. 31, No. 4, pp. 707–708, 1964b.

Leishman, J. G. *Principles of Helicopter Aerodynamics*, 1st ed., Cambridge University Press, Cambridge, 2000.

Lian, Y. and Shyy, W. "Laminar-Turbulent Transition of a Low Reynolds Number Rigid or Flexible Airfoil," *AIAA Journal*, Vol. 45, No. 7, pp. 1501–1513, 2007.

Liepmann, H. W. "Investigation of Boundary Layer Transition on Concave Walls," NACA, NACA-WR-W-87, Washington, D.C., 1945.

Mabey, D. G., Ashill, P. R., and Welsh, B. L. "Aeroelastic Oscillations Caused by Transitional Boundary Layers and Their Attenuation," *Journal of Aircraft*, Vol. 24, No. 7, pp. 463–469 1987.

Mack, L. M. "Computation of the Stability of the Laminar Compressible Boundary Layer," *Methods in Computational Physics Vol. 4* edited by B. Alder, S. Fernbach, M. Rotenberg, Academic Press, pp. 247-299, 1965.

Mack, L. M. "Linear Stability Theory and the Problem of Supersonic Boundary-Layer Transition," *AIAA Journal*, Vol. 13, No.3, pp. 278–289, 1975.

Mai, H. and Hebler, A. "Aeroelasticity of a Laminar Wing," *Proc. IFASD 2011*, IFASD, Paris, 2011.

Malan, P., Suluksna, K., and Juntasaro, E. "Calibrating the γ-Re_θ Transition Model for Commercial CFD," *47th AIAA Aerospace Sciences Meetings*, AIAA, Orlando, 2009.

Mayle, R. E. "The Role of Laminar-Turbulent Transition in Gas Turbine Engines," *Journal of Turbomachinery*, Vol. 113, pp. 509-537, 1991.

McGhee, R. J., Beasley, W. D., and Foster, J. M. "Recent Modifications and Calibration of the Langley Low-Turbulence Pressure Tunnel," NASA, TP-2328, Hampton, 1984a.

McGhee, R. J., Viken, J. K., Pfenninger, W., Beasley, W. D., and Harvey, W. D. "Experimental Results for a Flapped Natural-Laminar-Flow Airfoil with High Lift/Drag Ratio," NASA, TM-85788, Hampton, 1984b.

Menter, F. R. "Two-Equation Eddy-Viscosity Turbulence Models for Engineering Applications," *AIAA Journal*, Vol. 32, No. 8, pp. 1598–1605, 1994.

Menter, F. R., Esch, T., and Kubacki, S. "Transition Modelling Based on Local Variables," *Engineering Turbulence Modelling and Experiments* edited by W. Rodi, N. Fueyo, Vol. 5, Elsevier Science Ltd., Philadelphia, pp. 555–564, 2002.

Menter, F. R., Langtry, R. B., Likki, S. R., Suzen, Y. B., Huang, P. G., and Völker, S. "A Correlation-Based Transition Model Using Local Variables – Part I: Model Formulation," *Journal of Turbomachinery*, Vol. 128, No. 3, pp. 413–422, 2006.

Menter, F. R., Smirnov, P. E., Liu, T., and Avancha, R. "A One-Equation Local Correlation-Based Transition Model," *Flow, Turbulence and Combustion*, Vol. 95, No. 4, pp. 583–619, 2015.

Meyer, R., Hakansson, S., and Liesner, K. "Turbulenzgradmessungen im DNW-TWG 2011," DLR, DLR-IB-92517-12 / B4, Berlin, 2012.

Michel, U. and Froebel, E. "Lower Limit for the Velocity Fluctuation Level in Wind Tunnels," *Experiments in Fluids*, Vol. 6, No. 1, pp. 49–54, 1988.

Mineck, R. E. "Comparison of NAE Porous Wall and NASA Adaptive Wall Test Results Using the NAE CAST-10 Airfoil Model," *CAST-10-2/DOA 2 Airfoil Studies Workshop Results* edited by E. J. Ray, A. S. Hill, CP-3052, pp 195–212, Hampton, 1989.

Misaka, T. and Obayashi, S. "Application of Local Correlation-Based Transition Model to Flows Around Wings," *44^{th} AIAA Aerospace Sciences Meeting and Exhibit*, AIAA, Reno, 2006.

Mislevy, S. P. and Wang, T. "The Effects of Adverse Pressure Gradients on Momentum and Thermal Structures in Transitional Boundary Layers: Part 1 - Mean Quantities," *ASME 1995 International Gas Turbine and Aeroengine Congress and Exposition*, ASME, Vol. 4, 95-GT-004, Houston, 1995.

Morkovin, M. V. "Critical Evaluation of Transition from Laminar to Turbulent Shear Layers with Emphasis on Hypersonically Travelling Bodies," Research Institute for Advanced Studies, AFFDL-TR-68-149, Maryland, 1969.

Narasimha, R. "The Laminar-Turbulent Transition Zone in the Boundary Layer," *Progress in Aerospace Science*, Vol. 22, pp. 29–80, 1985.

Narasimha, R. and Dey, J. "Transition-Zone Models for 2-Dimensional Boundary Layers: A Review," *Sadhana*, Vol. 14, No. 2, pp. 93–120, 1989.

Orr, W. M. "The Stability or Instability of the Steady Motions of a Perfect Liquid and of a Viscous Liquid. Part I: A Perfect Liquid, *Proceedings of the Royal Irish Academy. Section A: Mathematical and Physical Sciences*, Vol. 27, pp. 9–68, 1907a.

Orr, W. M. "The Stability or Instability of the Steady Motions of a Perfect Liquid and of a Viscous Liquid. Part II: A Viscous Liquid, *Proceedings of the Royal Irish Academy. Section A: Mathematical and Physical Sciences*, Vol. 27, pp. 69–138, 1907b.

Pettersson, K. and Crippa, S. "Implementation and Verification of a Correlation Based Transition Prediction Method," *38th Fluid Dynamics Conference and Exhibit*, AIAA, Seattle, 2008.

Pfenninger, W. "Flow Phenomena at the Leading Edge of Swept Wings," *Recent Developments in Boundary Layer Research IV*, AGARD, AGARDograph 97, Paris, 1965.

Poirel, D., Harris, Y., and Benaissa, A. "Self-Sustained Aeroelastic Oscillations of a NACA0012 Airfoil at Low-to-Moderate Reynolds Numbers," *Journal of Fluids and Structures*, Vol. 24, No. 5, pp. 700–719, 2008.

Radespiel, R., Windte, J., and Scholz, U. "Numerical and Experimental Flow Analysis of Moving Airfoils with laminar Separation Bubbles," *AIAA Journal*, Vol. 45, No. 6, pp. 1346–1356, 2007.

Rayleigh, J. S. "On the Stability, or Instability, of Certain Fluid Motions," *Proc. London Math. Soc.*, Vol. 11, pp. 57–72, 1879.

Rayleigh, J. S. "On the Stability or Instability of Certain Fluid Motions, II," *Proc. London Math. Soc.*, Vol. 19, pp. 67–75, 1887.

Redeker, G., Horstmann, K., Köster, H., Thiede, P., and Szodruch, J. "Design of a Natural Laminar Flow Glove for a Transport Aircraft," *Flight Simulation Technologies Conference and Exhibit*, AIAA, Dayton, 1990.

Reynolds, O. "An Experimental Investigation of the Circumstances which Determine Whether the Motion of Water Shall be Direct or Sinuous, and of the Law of Resistance in Parallel Channels," *Proc. R. Soc. Lond.*, Vol. 35, pp. 84–99, 1883.

Richter, K., Koch, S., Gardner, A. D., Mai, H., Klein, A., and Rohardt, C. H. "Experimental Investigation of Unsteady Transition on a Pitching Rotor Blade Airfoil," *Journal of the American Helicopter Society*, Vol. 59, No. 012001, pp. 1–12, 2014.

Roach, P. E. and Brierly, D. H. "The Influence of a Turbulent Free-Stream on Zero Pressure Gradient Transitional Boundary Layer Development Part I: Test Cases T3A and T3B," *Numerical Simulation of Unsteady Flows and Transition to Turbulence*, edited by O. Pironneau, W. Rodi, I. L. Ryhming, A. M. Savill, T. V. Truong, Cambridge University Press, pp. 319–347, Cambridge 1992.

Rouse, H. *Elementary Mechanics of Fluids*, 1st ed., J. Wiley & Sons, Washington, New York, 1946.

Saric, W. S., Reed, H. L., and Kerschen, E. J. "Boundary-Layer Receptivity to Freestream Disturbances," *Annual Review of Fluid Mechanics*, Vol. 34, pp. 291–319, 2002.

Saric, W. S., Reed, H. L., and White, E. B. "Stability and Transition of Three-Dimensional Boundary Layers," *Annual Review of Fluid Mechanics*, Vol. 35, No. 1, pp. 413–440, 2003.

Savill, A. M. "A Synthesis of T3 Test Case Predictions," *Numerical Simulation of Unsteady Flows and Transition to Turbulence*, edited by O. Pironneau, W. Rodi, I. L. Ryhming, A. M. Savill, T. V. Truong, Cambridge University Press, pp. 404–441, Cambridge 1992.

Schlichting, H. "Zur Entstehung der Turbulenz bei der Plattenströmung," *Nachr. Ges. Wiss. Göttingen, Math.-Phys. Klasse*, Fachgruppe II, No. 38, pp. 181–208, 1933.

Schlichting, H. and Gersten, K. *Grenzschicht-Theorie*. 10th ed., Springer, Berlin, 2006.

Schmid, P. J. and Henningson, D. S. "Stability and Transition in Shear Flows," *Applied Mathematical Sciences* edited by J. E. Marsden, L. Sirovich, Vol. 142, Springer, New York, 2001.

Schrauf, G., Perraud, J., Vitiello, D., and Lam, F. "Comparison of Boundary-Layer Transition Predictions Using Flight Test Data," *Journal of Aircraft*, Vol. 35, No. 6, pp. 891–897, 1998.

Schreiber, H.-A., Steinert, W., and Küsters, B. "Effects of Reynolds Number and Free-Stream Turbulence on Boundary Layer Transition in a Compressor Cascade," *Journal of Turbomachinery*, Vol. 124, No. 1, 2002.

Schubauer, G. B. and Klebanoff, P. S. "Contributions on the Mechanics of Boundary-Layer Transition," NACA, TN-3489, Washington, D.C., 1955.

Schubauer, G. B. and Skramstad, H. K. "Laminar-Boundary-Layer Oscillations and Transition on a Flat Plate," NACA, Report 909, Washington, D.C., 1948.

Schwamborn, D., Gerhold, T., and Heinrich, R. "The DLR TAU-Code: Recent Applications in Research and Industry," *Proc. European Conference on Computational Fluid Dynamics ECCOMAS* edited by P. Wesseling, E. Oñate, J. Périaux, TU Delft, 2006.

Seitz, A., Kruse, M., Wunderlich, T., Bold, J., and Heinrich, L. "The DLR Project LamAiR: Design of a NLF Forward Swept Wing for Short and Medium Range Transport Application," *29th AIAA Applied Aerodynamics Conference*, AIAA, Honolulu, 2011.

Seyb, N. J. "The Role of Boundary Layers in Axial Flow Turbomachines and the Prediction of their Effects," *Boundary Layer Effects in Turbomachines* edited by J. Surugue, AGARD, AGARD-AG-164, pp. 241–260, 1972.

Seyfert, C. and Krumbein, A. "Evaluation of a Correlation-Based Transition Model and Comparison with the e^N-method," *40th Fluid Dynamics Conference and Exhibit*, AIAA, Chicago, 2010.

Singh, U. K. "The Effect of Viscosity on the Flow past Aerofoils in Cascade," Ph. D. Dissertation, University of Liverpool, Liverpool, 1974.

Smith, A. M. O. and Gamberoni, N. "Transition, Pressure Gradient and Stability Theory," Douglas Aircraft Company, Report ES 26388, El Segundo, 1956.

Somers, D. M. and Horstmann, K.-H. "Design of a Medium-Speed, Natural-Laminar-Flow Airfoil for Comuter Aircraft Application," DFVLR, IB 129-85/26, Braunschweig, 1985.

Sommerfeld, A. "Ein Beitrag zur Hydodynamischen Erklaerung der turbulenten Fluessigkeitsbewegungen," *Atti del IV Congresso internazionale dei Matematici*, Vol. 3, pp. 116–124, 1908.

Spalart, P. R. and Rumsey, C. L. "Effective Inflow Conditions for Turbulence Models in Aerodynamic Calculations," *AIAA Journal*, Vol. 45, No. 10, pp. 2544–2553, 2007.

Stanewsky, E. and Zimmer, H. "Development and Wind Tunnel Investigation of Three Supercritical Airfoil Profiles for Transport Aircraft," NASA, TM-75840, Washington, D.C., 1980.

Stanewsky, E., Demurie, F., Ray, E. J., and Johnson, C. B. "High Reynolds Number Tests of the CAST-10-2/DOA 2 Transonic Airfoil at Ambient and Cryogenic Temperature Conditions," *AGARD Conference Proceedings*, No. 348, pp 47–60, 1984.

Suder, K. L., O'Brien, J. E., and Reshotko, E. "Experimental Study of Bypass Transition in a Boundary Layer," NASA, NASA-TM-100913, Cleveland, 1988.

Suluksna, K., Dechaumphai, P., and Juntasaro, E. "Correlations for Modeling Transitional Boundary Layers Under Influences of Freestream Turbulence and Pressure Gradient," *International Journal of Heat and Fluid Flow*, Vol. 30, No. 1, pp. 66–75, 2009.

Theodorsen, T. "General Theory of Aerodynamic Instability and the Mechanism of Flutter," NACA, Report 496, Washington, D.C., 1935.

Tollmien, W. "Über die Entstehung der Turbulenz," *Nachr. Ges. Wiss. Göttingen*, Math.-Phys. Klasse, 1. Mitteilung, pp. 21–44, 1929.

Tollmien, W. "Ein allgemeines Kriterium der Instabilität laminarer Geschwindigkeitsverteilungen," *Nachr. Ges. Wiss. Göttingen*, Math.-Phys. Klasse, Fachgruppe 1, Mathematik, Vol. 1, pp. 79–114, 1935. Translated as "General Instability Criterion of Laminar Velocity Distributions," NACA, TM-792, 1936. Washington, D.C.,.

van de Vooren, A. I. and Bergh, H. "Spontaneous Oscillations of an Aerofoil due to Instability of the Laminar Boundary Layer," National Aeronautical Research Institute, Report F.96, Amsterdam, 1951.

van Driest, E. R. and Blumer, C. B. "Boundary Layer Transition: Freestream Turbulence and Pressure Gradient Effects," *AIAA Journal*, Vol. 1, No. 6, pp. 1303–1306, 1963.

van Ingen, J. L. "A Suggested Semi-Empirical Method for the Calculation of the Boundary Layer Transition Region," *Technische Hogeschool Vliegtuigbouwkunde*, Report V.T.H.-74, Delft, 1956.

von Doenhoff, A. E. and Abott, F. T., Jr. "The Langley Two-Dimensional Low-Turbulence Pressure Tunnel," NACA, TN-1283, Washington, D.C., 1947.

Wazzan, A. R., Okamura, T. T., and Smith, A. M. O. "Spatial and Temporal Stability Charts for the Falkner-Skan Boundary-Layer Profiles," McDonnell Douglas Astronautics Co., DAC-67086, Huntington Beach, 1968.

White, F. M. *Viscous Fluid Flow*. 2nd ed., McGraw-Hill, New York, 1991.

Windte, J. and Radespiel, R. "Propulsive Efficiency of a Moving Airfoil at Transitional Low Reynolds Numbers," *AIAA Journal*, Vol. 46, No. 9, pp. 2165–2177, 2008.

Wright, J. R. and Cooper, J. E. *Introduction to Aircraft Aeroelasticity and Loads*. 1st ed., John Wiley & Sons, West Sussex, 2007.

Yuan, W., Poirel, D., Wang, B., and Benaissa, A. "Effect of Freestream Turbulence on Airfoil Limit-Cycle Oscillations at Transitional Reynolds Numbers," *Journal of Aircraft*, Vol. 52, No. 4, pp. 1214–1225, 2015.

Zwaaneveld, J. "Aerodynamic Characteristics of the Supercritical Shock-Free Airfoil Section NLR 7301," NLR, TR 76052 C, 1976.

Zwaaneveld, J. "NLR 7301 Airfoil," *Experimental Data Base for Computer Program Assessment*, edited by J. Barche, AGARD, AGARD-AR-138, 1979.

Acknowledgement

First, I would like to express my gratitude to my advisors Prof. Lorenz Tichy and Prof. Rolf Radespiel for the support of my Ph.D. thesis and research at the DLR Institute of Aeroelasticity in Göttingen. Their encouragement and suggestions helped to develop the subject and to push further into the domain of transitional flows.

My thanks goes to my supervisors Dr.-Ing. Holger Hennings and Jens Nitzsche, who enabled me to pursue my research and encouraged me to develop new ideas. Their support in difficult periods of my dissertation helped to focus on the matter.

In addition, I want to thank my colleagues Anna Petersen, Wolfgang Wegner, Andreas Krumbein, Cornelia Grabe, Stefan Surrey, Benjamin Lütke, Felix Wienke, Diliana Friedewald, Anne Hebler, Sebastian Helm, and Christoph Kaiser for all the discussions during the last years.